



FCTUC DEPARTAMENTO DE ENGENHARIA CIVIL
FACULDADE DE CIÊNCIAS E TECNOLOGIA
UNIVERSIDADE DE COIMBRA



Numerical Simulation of Connections Designed For Seismic Actions

**In Partial Fulfilment of the requirements for the degree of Master in Civil
Engineering**

Author

Ângela Sofia Sequeira Lemos

Supervisors:

Prof. Dr. Luís Alberto P. Simões da Silva (FCTUC)

Prof. Dr. Jean-Pierre Jaspart (ULG)

Esta dissertação é da exclusiva responsabilidade da sua autora, não tendo sofrido correções após a defesa em provas públicas. O Departamento de Engenharia Civil da FCTUC declina qualquer responsabilidade pelo uso da informação apresentada.

Financial support from Fundação para a Ciência e a Tecnologia (FCT) under contract grant PTDC/ECM-EST/3711/2014 and also from the European Community's Research Fund for Coal and Steel (RFCS) under grant agreement n° RFSR-CT-2015-00022, is gratefully acknowledged.

Coimbra, December 2015

AGRADECIMENTOS

A presente dissertação foi desenvolvida com a contribuição dos Departamentos de Engenharia Civil da Universidade de Coimbra e da Universidade de Liège.

Expresso aqui uma enorme gratidão por todos aqueles que contribuíram com o seu apoio para este trabalho. Aos alunos do programa doutoral da Universidade de Coimbra, nomeadamente ao João Nuno, às alunas de doutoramento da Universidade de Salerno, Antonella Francavilla e Marina D’antimo e aos meus orientadores, Professor Doutor Luís Simões da Silva e Professor Doutor Jean-Pierre Jaspard. Obrigada pelo apoio!

O meu muito obrigado aos investigadores da Universidade Salerno que pacientemente responderam a todas as minhas questões e disponibilizaram todo o material necessário ao desenvolvimento da tese, Doutor Massimo Latour e Professor Doutor Gianvittorio Rizzano. Uma especial referência ao Professor Doutor Jean François Demonceau da Universidade de Liège e ao aluno de doutoramento da Universidade de Coimbra Hugo Augusto, pela ajuda imprescindível durante todo o processo e pela sua incansável paciência para comigo.

À Joana Castanheira e ao João Costa pela sua amizade incondicional, força e apoio que sempre me deram. E claro, à minha grande amiga e colega, Ana Francisca Santos.

Ao apoio imensurável que os meus pais sempre me deram ao longo da minha vida. Esta fase não foi diferente e, como sempre, a presença deles foi sentida. Ao meu querido irmão. O melhor amigo que alguém pode ter. É uma sorte ter-te comigo. Amo-vos aos três.

Há ainda aquelas pessoas a quem não agradei em particular mas que estão neste momento com um sorriso, porque sabem que é delas que estou a falar.

“A gem cannot be polished without friction, nor a man perfected without trials.”

Lucius Annaeus Seneca

RESUMO

Estruturas em aço têm sido cada vez mais utilizadas em diversos tipos de aplicações. No entanto, estas demonstraram problemas quando submetidas a alguns eventos sísmicos passados, os quais provocaram elevados danos estruturais e, conseqüentemente, elevados custos de reparação. De forma a garantir a operacionalidade dos edificios e, mais importante, a ausência de colapso na sucessão de um evento sísmico forte, uma profunda investigação está a ser feita. As mais recentes descobertas ao nível do comportamento sísmico destas estruturas estão a ser introduzidas nas regras de dimensionamento de edificios em aço situados em regiões sísmicas.

Este documento tem como objectivo o estudo de um novo tipo de ligação proposta por um grupo de investigadores envolvidos num projeto europeu designado por “FREEDAM”. O principal intuito do programa é a inserção de uma nova componente dissipativa por atrito numa ligação semi-rígida viga-coluna, a qual irá permitir a dissipação da energia transferida por um evento sísmico destrutivo através do escorregamento de um adesivo, sem criar qualquer dano estrutural aos restantes componentes da ligação. O conceito de sustentabilidade está intrinsecamente associado a esta nova solução devido ao facto de nenhum elemento estrutural sofrer danos na sucessão de eventos sísmicos excepcionais. Tal é apenas possível porque o novo sistema permite o fácil acesso, reparação ou substituição do material de fricção. Adicionalmente, o grau de confiança e robustez de estruturas com este tipo de ligação poderá aumentar em zonas de elevada sismicidade.

A eficiência da nova componente será avaliada com base na área e estabilidade das curvas representativas do seu comportamento histerético e com base na sua capacidade de dissipação de energia analisada isoladamente e quando implementada na ligação.

ABSTRACT

Steel structures have been widely used in different types of applications in the past years. However, some steel constructions did not have a good performance when subjected to seismic events in the past, leading to considerable damage to the buildings and the consequent significant cost of repairs. In order to guarantee that buildings remain operational or, more importantly, do not collapse after strong seismic events, extensive investigation is being carried out. The findings of recent studies are being implemented in the design regulations for steel buildings in seismic zones.

The aim of this dissertation is to study a new type of connection proposed by a group of researchers involved in the European Research program named “FREEDAM”. The main goal of this program is to develop an innovative friction component within beam-to-column connections in Moment Resisting Frames (MRF), which will be able to dissipate the input energy of a destructive seismic event by means of the slippage of a damper material, without any damage to the other structural components.

Additionally, the concept of sustainability is directly allied to this new solution due to the fact that no structural parts will suffer any damage during the aftermath of an earthquake. This is achievable because it is possible to easily repair or replace the friction material in the new system. Moreover, this solution also results in an increased reliability and robustness in the case of exceptional events.

The efficiency of the damper material will be evaluated through the width and stability of the hysteresis loops and the energy dissipation capacity of the component alone, as well as its influence on the overall connection.

Table of Contents

1. INTRODUCTION	1
1.1. GENERAL CONSIDERATIONS	1
1.2. OBJECTIVES	1
1.3. STRUCTURE OF THE DISSERTATION	2
2. STATE OF THE ART	3
2.1. BEAM-TO-COLUMN CONNECTIONS IN MOMENT RESISTING FRAMES SUBJECTED TO SEISMIC LOADING	3
2.2. DISSIPATIVE DOUBLE SPLIT TEE JOINTS EQUIPPED WITH FRICTION DAMPERS	5
2.2.1. INTRODUCTION	5
2.2.2. FRICTION	6
2.2.2.1. Friction interactions	6
2.2.2.2. Experimental characterization of friction pads	7
2.2.3. EXPERIMENTAL BEHAVIOUR OF FULL-SCALE DST JOINTS	9
3. NUMERICAL ANALYSIS OF THE FRICTION COMPONENT	11
3.1. INTRODUCTION	11
3.2. EXPERIMENTAL PROCEDURE AND RESULTS – SALERNO UNIVERSITY	11
3.3. MODELLING FRICTION PROBLEMS IN ABAQUS SOFTWARE	16
3.3.1. INTRODUCTION	16
3.3.2. SCRIPTING IN ABAQUS	18
3.4. MODELLING PRELOADING FORCES IN ABAQUS	21
3.5. FEM MODEL	24
3.5.1. MECHANICAL PROPERTIES OF THE MATERIALS	24
3.5.1.1. Steel plates and bolts	24
3.5.1.2. Friction material	24
3.5.2. GEOMETRY OF THE MODEL	25
3.5.3. ADJUSTMENTS OF THE BOLTS	25
3.5.4. MESH ADOPTED	26
3.5.5. STEPS	28
3.5.6. DISPLACEMENTS AND BOUNDARY CONDITIONS	29
3.5.7. FRICTIONAL BEHAVIOUR – TANGENTIAL CONTACT PROPERTIES	29
3.5.7.1. Energy considerations for friction variations	29
3.5.8. RESULTS	32
3.5.8.1. Force-displacement curve	32
3.5.8.2. Energy dissipation capacity	33
3.5.8.3. Wearing of the material	34
3.6. DISCUSSION OF THE NUMERICAL MODELLING	35
4. COMPONENT APPROACH	36
4.1. INTRODUCTION	36
4.2. DETAILED DESCRIPTION OF THE SPECIMENS	36
4.3. VERIFICATION OF THE DESIGN RULES APPLIED BY SALERNO	39
4.3.1. INTRODUCTION	39

4.3.2.	DETERMINATION OF THE DESIGN STRESSES	39
4.3.3.	DEFINITION OF THE LENGTH OF THE SLOTTED HOLES	41
4.3.4.	DESIGN OF THE T-STUB FLANGE – HOGGING MOMENT	41
4.3.4.1.	Definition of the thickness of the T-stub flange	42
4.3.4.2.	Definition of the bolts	43
4.3.4.3.	Geometric compatibilities	44
4.3.5.	CHECK THE L-STUB BENDING RESISTANCE – SAGGING MOMENT	45
4.3.5.1.	Initial considerations	45
4.3.5.2.	Calculation of the resistance of the L-stub	45
4.3.6.	CHECK THE COLUMN WEB IN COMPRESSION	49
4.3.6.1.	Design of the continuity plates	49
4.3.6.2.	Design of the continuity plates welds	50
4.3.7.	CHECK OF THE SHEAR PANEL RESISTANCE	51
4.3.8.	CHECK OF THE COLUMN FLANGE RESISTANCE	52
4.4.	DEVELOPMENT OF MOMENT-ROTATION CURVES FOR THE CONNECTIONS	52
4.4.1.	IDENTIFICATION OF THE RELEVANT COMPONENTS	53
4.4.2.	INITIAL STIFFNESS, $K_{i,HOGG}$ - HOGGING MOMENT	55
4.4.3.	MODIFIED STIFFNESS, $K_{MOD,HOGG}$ - HOGGING MOMENT	56
4.4.4.	DESIGN MOMENT RESISTANCE, $M_{V,HOGG}$ - HOGGING MOMENT	57
4.4.5.	ULTIMATE MOMENT RESISTANCE, $M_{U,HOGG}$ – HOGGING MOMENT	58
4.4.6.	INITIAL STIFFNESS, $K_{i,SAGG}$ - SAGGING MOMENT	59
4.4.7.	MODIFIED STIFFNESS, $K_{MOD,SAGG}$ - SAGGING MOMENT	60
4.4.8.	DESIGN MOMENT RESISTANCE, $M_{V,SAGG}$ - SAGGING MOMENT	61
4.4.9.	ULTIMATE MOMENT RESISTANCE, $M_{U,SAGG}$ – SAGGING MOMENT	61
4.4.10.	FINAL M - ϕ MONOTONIC CURVE	61
4.4.11.	FINAL STATEMENT	63
5.	NUMERICAL SIMULATION OF THE INNOVATIVE JOINT	64
5.1.	INTRODUCTION	64
5.2.	FINITE ELEMENT MODEL DEVELOPMENT	64
5.2.1.	DESCRIPTION OF THE NUMERICAL MODEL	64
5.2.1.1.	Material properties	65
5.2.1.2.	Steps used in the numerical model	66
5.2.1.3.	Type of finite elements	69
5.2.1.4.	Interaction properties	69
5.2.1.5.	Boundary conditions	70
5.2.1.6.	Scripting interface	70
5.3.	RESULTS	70
5.3.1.	MONOTONIC BEHAVIOUR	71
5.3.2.	CYCLIC BEHAVIOUR	74
5.3.2.1.	Moment-rotation curve	74
5.3.2.2.	Energy dissipation capacity	74
5.3.2.3.	Variation of the preloading force	75
5.3.3.	DISCUSSION OF THE RESULTS	76
6.	CONCLUSIONS AND FURTHER STUDIES	77
6.1.	CONCLUSIONS	77
6.2.	FURTHER STUDY	78

NOTATIONS

a_{cp} – Thickness of the continuity plate's welds

b_c – Column width of an H section

b_p – Width of a plate

d – Nominal diameter of the bolt

d_0 – Hole diameter for a bolt

h – High of an I or H section

k – Torque coefficient

l – Length of a fillet weld

r – Root radius of an I or H section

s – Force per unit of area needed to shear cold weld junctions

s_0 – Critical shear stress of the weaken material

t_f – Flange thickness of an I or H section

t_w – Web thickness of an I or H section

w – Distance between two bolts of the same row

z – Lever arm

z_{eq} – Equivalent lever arm

A – Contact area on the friction interface

A_s – Tensile stress area of the bolt

C_u – Compressive force applied to the connection

E – Young Modulus

E_{diss} – Dissipated Energy

$E_{diss,cum}$ – Cumulated Energy dissipated

F – Total Sliding Force

\bar{F} – Non-dimensional Sliding Force

F_A – Total friction force due to adhesion phenomena

I_i – Inertia Moment of element i

$M_{diss, jc, Rd}$ – Moment design value of the dissipative joint component

$M_{j, Rd}$ – Design moment resistance of a joint

$M_{no-diss, jc, Rd}$ – Moment design value of the non-dissipative joint component

$M_{pl,i,Rd}$ – Moment resistance of the T-stub flange for mechanism type- i ($i=1,2$ or 3)

N – Normal Force

N_b – Bolt pre-loading Force

P – Contact pressure

T_b – Value of the tightening torque

T – Temperature

T_u – Tensile force applied to the connection

V_{cf} – Shear force applied to the connection

γ_{Mi} – partial safety coefficients for connections

γ_{ov} – Overstrength factor referred in EC8-1

$\gamma_{ov,rm,diss,jc}$ – Random material variability factor regarding the dissipative joint component

$\gamma_{ov,sh,diss,jc}$ – Material strain hardening factor regarding the dissipative joint component

$\delta_{u, comp.}$ – Ultimate stroke of the component

ΔL_{bolt} – Adjustment of the bolt length

ΔL^* – Elastic deformation of all intermediate plates

ΔL_{total} – Total adjustment of the bolt length

ε_{bolt} – Bolt extension

μ – Friction coefficient

σ_0 – Material penetration hardness

σ_{\perp} – Normal tension perpendicular to the thickness

$\sigma_{//}$ – Normal tension parallel to the weld axis

τ_{\perp} – Tangential tension perpendicular to the weld axis

$\tau_{//}$ – Tangential tension parallel to the weld axis

u – Sliding speed.

φ_u – Ultimate rotation of the connection

ϕ – Rotation of the connection

ABBREVIATIONS

FFD – Free From Damage

GUI – Graphical User Interface

MRF – Moment Resisting Frame

DST – Double-Split Tee

FREEDAM- Free From Damage Connections

FEM- Finite Elements Method

BWWF – Bolted Web-Welded Flange

EC - Eurocode

LVDT - Linear Variable Differential Transformer

RBS- Reduced Beam Section

ULS – Ultimate Limit State

SLS – Serviceability Limit State

DLS – Damage Limit State

EN – Euronorm

1. INTRODUCTION

1.1. General considerations

Although steel Moment Resisting Frames (MRFs) have been known for their good performance in past seismic events, with little loss of life and few recorded collapses, the same has not been observed for some rare earthquakes such as the 1994 Northridge and 1995 Kobe earthquakes. Therefore, research into new techniques to prevent structural damage to buildings has gained relevance. Additionally, the territory of Portugal is characterized by medium to high levels of seismicity. For these reasons Portugal, and some other countries with identical motivations, have united their skills and competences in order to discover innovative solutions aimed at preventing or reducing the impacts of an earthquake.

Dissipative zones in steel MRFs are usually located at the beam ends where energy can be dissipated and structural elements may suffer significant strength degradation. However, even if the damage to the structural components is responsible for the dissipation of certain amounts of energy, it should also be avoided. The global tendency has been a shift towards the development and implementation of low damage seismic resisting systems in order to reduce the economic effects of earthquakes. In addition, any probable minor damage may be fixed easily and cheaply thus preventing the collapse of the building and guaranteeing that it rapidly becomes operational.

1.2. Objectives

The main goal of this work is to study a new type of connection that prevents damage to all other structural components with the exception of the one component of the connection that is specially designed to dissipate the input energy of a seismic hazard by means of the slippage of a friction material. In addition, the friction component of the connection must satisfy certain requirements, such as: possess a stable hysteretic behaviour as well as a great energy dissipation capacity and ductility supply. In order to do that, the friction material must have a good tribological behaviour.

The abovementioned study of the connection was proposed as a part of the European project named “FREEDAM”, which includes the participation of several international organisations: the University of Salerno (UNISA), the University of Naples (UNINA), the University of Coimbra (UC), the University of Liege (ULG), the

companies “FIP INDUSTRIALE” and “O FELIZ”. The name adopted for the project is related to the fact that a Free From Damage Connection is being developed.

This dissertation discusses two different programmes intending, on one hand, to fully explore the behaviour of the friction interfaces and, on the other hand, analyse the results when applied to joints that are specially designed to dissipate the input energy of seismic events. More specifically, the present dissertation focuses on the following objectives:

- The development of a strategy for the numerical modelling of complex friction problems. The proposed approach should be able to describe the friction behaviour of the damper installed in the bolted connection.
- The design of an innovative connection and the obtainment of the moment-rotation curves that characterize the monotonic behaviour of the joint. For this purpose, the component approach is applied.
- The numerical modelling of the overall beam-to-column connection equipped with the friction device, when subjected to monotonic and cyclic loading conditions.

The numerical modelling was developed using the Finite Elements Method (FEM) with *Abaqus* Software.

1.3. Structure of the dissertation

Six main chapters constitute the present thesis. In **Chapter 1**, the relevance of the studies herein presented is justified, the objectives are discussed, the methodology adopted is described and the global organization of this dissertation is explained.

The subsequent chapter, **Chapter 2**, evaluates current knowledge in the field of MRF frames designed to have connections with a stable hysteretic behaviour and a wide range of energy dissipation capacity. To this end, some of the principal studies already performed are discussed.

In **Chapter 3**, numerical work for the friction device is presented as well as the results and conclusions derived.

In **Chapter 4**, the component approach is used for the design of the connection and also to develop moment-rotation curves ($M-\phi$ curves), making it possible to understand the behaviour of the full-scale beam-to-column connections better. The results obtained are compared with experiments already performed for those connections. A more profound analysis of the hysteretic behaviour obtained for the innovative connection is attained by developing a numerical model for the overall joint, using *Abaqus* Software and is discussed in **Chapter 5**.

Finally, conclusions and future work to be done are explored in **Chapter 6**.

2. STATE OF THE ART

2.1. Beam-to-column connections in moment resisting frames subjected to seismic loading

The use of full strength joints in steel Moment Resisting Frames (MRFs) provides a good dissipative capacity and avoids the plastic engagement of the elements constituting the beam-to-column connections, as the dissipative zones are located at the beam ends. Among various other connection typologies, the bolted web-welded flange joint (BWFF) was considered to have a good seismic response. However, during the Kobe and Northridge earthquakes already mentioned in **Chapter 1**, a relatively poor performance of BWFF connections was observed due to the cracking of the welds (**Iannone et al., 2011, Grecea et al., 2004**). Thus, research into innovative connections has been conducted mainly to come up with a new solution that provides the required combination of strength, stiffness and ductility but avoids the previously observed cracking. Moreover, due to uncertainties of the quality of the weld, the idea of mainly using bolts was investigated and later came to be known as “weld free” systems (**Koetaka et al., 2005; Inoue et al., 2006**).

For this reason, several types of connections have been proposed, such as the end-plate and T-stub bolted connections, properly designed for seismic regions. Naturally, because of the inelastic behaviour of such connections due to the plates, bolts and T-stubs contribution, the analysis of such solutions has become more complex. Nevertheless, numerical work performed proved that a great deal of ductility could be achieved and the Finite Elements Method (FEM) could be used to predict the behaviour of such connections.

Finally, semi-rigid partial-strength connections started to generate interest among investigators and Eurocode 8 (**CEN, 2004**) introduced the idea of dissipating the input energy of an earthquake in the elements of the connection. Furthermore, double split tee (DST) connections have proved to be a promising solution that could be applied in dissipative semi-rigid MRFs because they are easily replaced, leading to the concept of sustainability, an essential requirement nowadays (**Iannone et al., 2011**). However, the results related to the dissipation supply in traditional DST connections were profoundly influenced by pinching and strength degradation.

Therefore, other researchers, such as **Inoue et al. (2006)**, **Kishiki et al. (2006)**, **Oh et al. (2009)**, and **Ramhormoziu and Clifton (2014)** have been studying solutions

involving beam-to-column connections equipped with passive energy dissipation devices.

Finally, **Latour et al. (2015)** investigated a new typology for beam-to-column joints by introducing two dampers at both beam flange levels.

However, after the initial tests, it was observed that, despite the geometrical symmetry of the joint, its behaviour was asymmetric and the displacements obtained on both upper and lower flange levels were not the same. Therefore, a modification of the configuration of the joint was suggested by inserting only one damper at the lower beam flange level. That research has, so far, only been published in Eurosteel proceedings, 2004 (Latour et al.,2014.a). With the second proposed layout, under bending actions, the joint is forced to rotate around the upper T-stub and the energy dissipation supply is provided by the slippage of the lower beam flange on the layers of friction materials. Moreover, with a classical fixed T-stub placed at the upper beam flange, concrete slab damage can also be easily prevented.

Further studies on the latter connection were proposed in the European project “FREEDAM”. The connection typologies discussed are depicted in Figure 2.1.

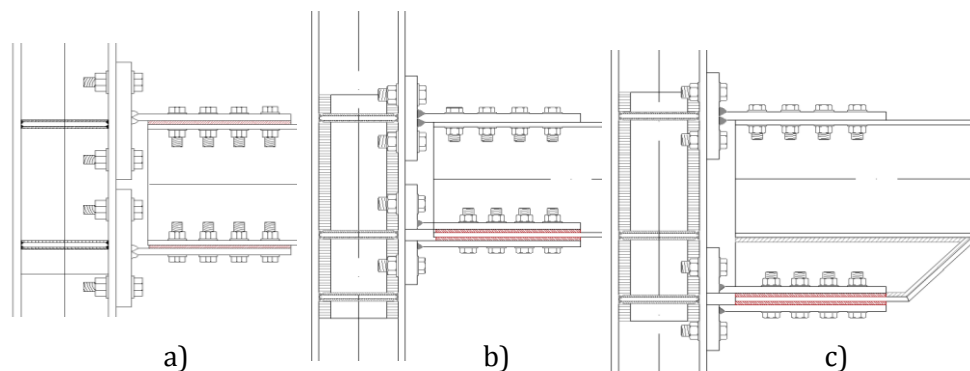


Figure 2.1: Geometry of the connections of main interest to this work: a) Connection with two friction dampers; b) Connection with only one friction damper; c) Connection with one friction damper and with an additional haunch.

Regarding semi-rigid partial strength connections, dynamic analyses have been performed in order to evaluate the stability of the cycles. However, it must be said that Eurocode 3 – Part 1-8 (**CEN, 2005**) only provides information for evaluating the monotonic response of beam-to-column connections. Therefore, the use of the component approach to predict the cyclic moment-rotation response should be studied carefully. Generally, the cyclic response of connections may be either stable or unstable, depending on the joint components involved in the plastic range, which can be defined based on design rules.

Therefore it is very important to define the cyclic behaviour of the individual components of the connections properly and also to identify which of them are responsible for the dissipation of the input seismic energy, i.e., it is of paramount importance to distinguish the dissipative from non-dissipative components. The main studies on this subject have pointed out that components subjected to compressive forces cannot behave as dissipative components because buckling mechanisms can be very unstable. Moreover, brittle mechanisms, such as the bolt or weld failure, should be avoided absolutely. Furthermore, excessive panel deformation could lead to the premature failure of the welds. Therefore, EC 8 recommends that the deformation of the column web panel in shear does not exceed 30% of the plastic rotation of the joint.

At Salerno University, experimental work was developed regarding both traditional and innovative double split tee connections. For the traditional DST connections, the components mainly responsible for the energy dissipation and the stability of the cyclic response are the two bolted T-Stubs, defined as the weakest components, while for the innovative DST connections those components are the friction dampers.

Both experiments followed similar procedures and used equivalent test set-ups. Therefore, it is easier to compare some of the results obtained for the two joints and point out some of the main drawbacks of traditional double split-tee connections when compared with the innovative connection equipped with friction dampers.

2.2. Dissipative double split tee joints equipped with friction dampers

2.2.1. Introduction

Structures designed to withstand earthquakes have to fulfil specific requirements such as stiffness, strength and ductility (**Grecea et al., 2004**). Therefore, three limit states should be considered: Serviceability limit state (SLS) related to stiffness criterion; Damageability limit state (DLS) related to strength criterion; and Ultimate limit state- (ULS) imposing ductility criterion.

The innovative connection must be designed in order to prevent the slippage of the friction pad under serviceability limit states and to be only activated under severe loading conditions. In other words, friction dampers can be used as displacement reducers at serviceability limit states (SLS) and as dissipative elements under ultimate limit states (ULS). Additionally, it is required that the components of the connection and structural elements do not achieve a plastic engagement and do not suffer any damage.

The energy dissipation capacity is provided by the movement of the T-stub webs on the friction pads, which are preloaded by means of high strength bolts.

Therefore, the slip force depends on the value of the normal force and on the friction coefficient.

2.2.2. Friction

All surfaces are rough. It is well known that even the most polished materials are not flat and that, when magnified sufficiently, surface undulations, characterized by valleys and hills large enough in comparison with molecular dimensions, may be observed. Those deviations from the plane are called asperities.

In order to completely understand the behaviour of friction interactions, two main definitions will be presented: adhesion and ploughing. These two phenomena are the main sources of friction between two sliding metal interfaces.

2.2.2.1. Friction interactions

When two surfaces are placed against each other, the contact is made at the tips of their asperities, where pressure can assume extremely high values. Strong adhesion may develop in these regions, causing the specimens to become a continuous solid. When this process occurs in metals it may be referred to as “cold welding”. Additionally, when one surface slides over one other, the previously formed junctions have to be sheared and the corresponding force to do it is equal to the frictional resistance.

However, if one surface is much harder than the other, the asperities on the harder surface will cut grooves in the softer one. This is called ploughing and the forces involved need to be accounted for in order to estimate the total friction force.

Mathematically, the total friction force results from the sum of both, the friction force due to adhesion and the friction force due to ploughing. However, it has been proved that the effects of the ploughing component in abrasion may be negligible when compared to the adhesion component, in the case of metals.

Therefore, the final sliding force (F) can be given by the total friction force due to adhesion (F_A), which can be simply proportional to the real contact area $A=N/\sigma_0$:

$$F = F_A = A \cdot s = \frac{N}{\sigma_0} \cdot s \quad (2.1)$$

where N is the normal load, σ_0 is the penetration hardness of the material and s is the force per unit of area needed to shear cold-weld junctions. By observing equation (2.1), it may be concluded that the ratio between the frictional force and the normal

applied load is a constant value (considering that the asperities are in the plastic range).

The classical theory of dry friction is based on the following three postulates:

1. The force of friction is directly proportional to the applied load. (Amontons' 1st Law)
2. The force of friction is independent of the apparent area of contact (Amontons' 2nd law);
3. Kinetic friction is independent of the sliding velocity (Coulomb's Law).

The first two, known as Amontons' laws, can be explained by Bowden and Tabor's theory (**Bowden and Tabor, 1967**). Under these considerations, the tangential force acting during slippage in the opposite direction of motion may be calculated by Coulomb's friction equation:

$$F = \mu \cdot N \quad (2.2)$$

where F is the sliding force, μ is the friction coefficient and N the normal action. According to equations (2.1) and (2.2), the friction coefficient may be determined as follows:

$$F = F_A = \frac{N}{\sigma_0} \cdot s_0 = \mu \cdot N \leftrightarrow \mu = \frac{s_0}{\sigma_0} \quad (2.3)$$

where s_0 represents the critical shear stress of the weakest material and σ_0 is the hardness of the softest material. For metals, the above relationship, derived from the classical Bowden and Tabor theory, provides reasonable results. However, when using rubber elements in the friction pads, characterized by big elastic ranges, the friction coefficient is influenced by the contact pressure (P) but also by the temperature (T) and sliding speed (v).

$$\mu = \mu(P, v, T) \quad (2.4)$$

For these materials, Amontons' laws cannot be applied and their tribologic relations depend on the adhesive junctions, the shear resistance of the rubbing materials and the real contact area.

2.2.2.2. Experimental characterization of friction pads

During research performed at Salerno University, two programmes were analysed. The first, was intended to characterize various frictional interfaces, the second, to apply the same materials to DST joints with the main goal of dissipating energy by using stable and wide loops. The second test programme is described later.

In order to provide a tribological characterization of the friction elements, several specimens were subjected to uniaxial loading conditions (**Latour et al.,2014.a;b and Latour et al., 2015**). The specimens were constituted by a layer of a friction material interposed between two plates made of S275 JR structural steel. In order to allow the relative movement of the outer steel plates on the friction material, one of the inner plates was made with slotted holes. The geometry of the specimens used may be visualized in Figure 2.2.

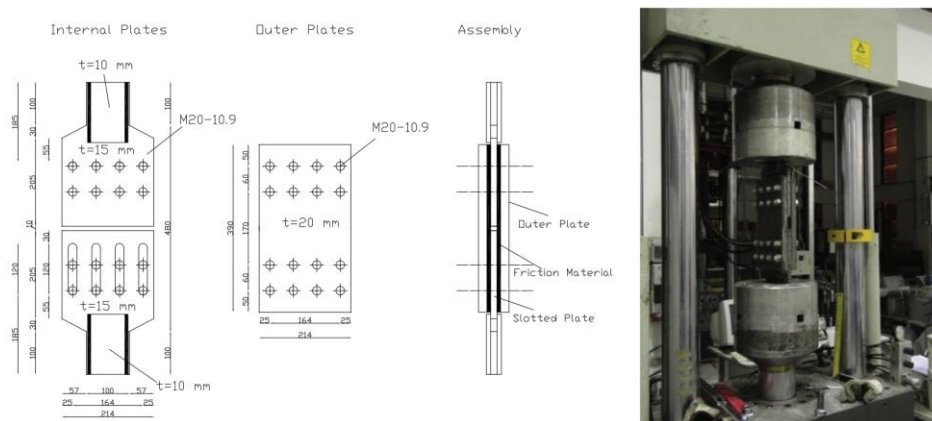


Figure 2.2: Scheme of the specimen's geometry (Latour et al., 2015).

Some parameters were changed during the experimental procedure in order to account for their influence on the friction coefficient and on the cyclic response of the specimen. These parameters were: the number of tightened bolts, the friction interface, the thickness of the friction interface, the tightening torque and the type of washer. Regarding the last variable, circular flat steel washers and cone shaped annular steel disc spring washers were analysed.

In order to evaluate the influence of the friction material, the following interfaces were subjected to analysis: steel on steel; brass alloy on steel; sprayed aluminium on steel; rubber material M0 on steel; rubber material M1 on steel; and rubber material M2 on steel. The rubber materials are detailed in Latour et al. (2014.b).

Tests were performed in order to obtain both static and kinetic friction coefficients, by varying the clamping force in a range suitable for structural applications. To do so, the experiments were executed in the Universal Testing Machine: Schenck Hydropuls S56. This machine is constituted by a hydraulic system with a load capacity of up to ± 630 kN, maximum stroke equal to ± 125 mm and a self-balanced steel frame used to counteract the axial loadings.

2.2.3. Experimental behaviour of full-scale DST joints

Full-scale tests on the dissipative joints were also performed at the University of Salerno, using the abovementioned friction materials. The main information about the experimental layout is summarized and shown in Figure 2.3:

- the column is horizontally connected to two steel hinges, while the beam is in a vertical position connected to the column;
- two different hydraulic actuators have been used: MTS 243.60 used to apply under force control, the axial load in the column, equal to 30 % of the squash load; and MTS 243.35 which was used to apply the desired displacement history at the beam end under displacement control;
- a horizontal frame was used in order to prevent lateral buckling (depicted in Figure 2.3). The frame restrains only the lateral displacements;
- four DST connections were tested with friction dampers located at both beam flange levels: TSJ-M1-CYC08, TSJ- M2-CYC09, TSJ-M2-DS-CYC10 and TSJ-B-CYC11. Later, two different connections were analyzed with only one damper positioned at the lower beam flange level: TSJ-SA-CYC12 and TSJ-H-SA-CYC13. Regarding the meaning of these labels, TSJ represents the joint typology: Tee Stub joint; M1, M2, B or SA symbolizes the different types of friction materials used; DS is an abbreviation for Disc Springs; H is an abbreviation for Hammer Head; and finally, CYXX corresponds to the progressive number of the cyclic tests.

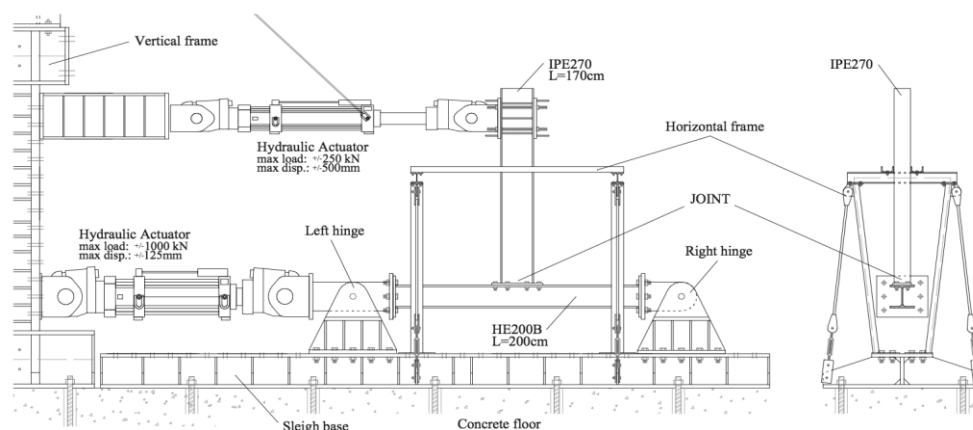


Figure 2.3: Test set-up used (M. Latour et al., 2015)

The experimental tests confirmed that the cyclic behaviour of the joint is mainly governed by the cyclic response of the friction pads. A comparison between the cyclic behaviour of four specimens (CYC09-CYC11) and of specimen TS-CYC04 made by means of their envelope curves is presented in Figure 2.4. In fact, all the specimens

The experimental program adopted for the two relevant friction interfaces is presented in Figure 3.2. Experiments performed for each specimen were divided in several tests, each using a different torque. For both metallic interfaces studied, three tests were made, which means that three levels of normal forces were applied. Each test was performed for a specific torque applied to the 4 bolts belonging to the second row (Figure 3.1). The tightening torques have been applied at the end of each loading sequence using a calibrated torque wrench. For each test or sequence, the displacement history was applied through 10 cycles, using different displacement amplitudes.

Additionally, in all loading sequences, a constant frequency of 0.25 Hz was adopted and, therefore, a variation of the displacement amplitude leads to an adjustment of the sliding velocity.

Interface	Torque	Number of bolts of friction pad	Number of cycles of the sequence	Amplitude
Steel-steel	200 N m	4	10	±30 mm
	300 N m		10	
	500 N m		10	
Sprayed aluminum-steel	200 N m	4	10	± 15 mm
	300 N m		10	
	400 N m		10	

Figure 3.2: Summary of the tests of the experimental program carried by Salerno University – Metallic interfaces (adapted from Latour et al., 2014.b)

Results obtained for both interfaces are depicted in Figure 3.3 and Figure 3.4. They report the hysteretic behaviour of the specimens, represented in terms of friction coefficient versus displacement. The friction coefficient was determined according to:

$$\mu = \frac{F}{mnN_b} \quad (3.1)$$

in which m is the number of surfaces in contact, n is the number of bolts, N_b corresponds to the bolt preloading force and, F is the sliding force. Italian standard CNR- UNI 10011(1997) recommends **equation (3.2)** for the calculation of the preloading force.

$$N_b = \frac{T_b}{k.d} \quad (3.2)$$

where T_b is the value of the tightening torque, d represents the nominal diameter of the bolt and k is the torque coefficient defined as the term which depends on friction coefficients, lead and thread angles, and on the diameter of the bolt. This coefficient assumes frequently the value of 0.2.

3. NUMERICAL ANALYSIS OF THE FRICTION COMPONENT

3.1. Introduction

The software used for the numerical analysis herein presented is Abaqus (version 6.13). Abaqus is a powerful finite element tool used for an extensive range of problems.

The numerical model developed in this dissertation involves the cyclic analysis of 2 possible types of friction dampers tested at the University of Salerno: steel on steel and sprayed aluminium on steel interfaces, both metallic interfaces. Although many more surfaces were analysed, the numerical procedure used in this chapter is time consuming and repetitive, meaning no further knowledge would be obtained if other interfaces were subjected to numerical analysis. Besides that, the elastic behaviour of the rubber materials was not provided by the Italian company that produced them.

In this chapter, the experimental results obtained for the two referred metallic interfaces are firstly analysed, then an introduction to modelling friction problems in Abaqus is presented and the application of preloading forces is studied. Furthermore, the numerical model used for the prediction of the friction behaviour is described in detail, numerical results are provided and final remarks are given at the end of the chapter.

3.2. Experimental procedure and results – Salerno University

Figure 3.1 depicts the geometry of the tested specimens.

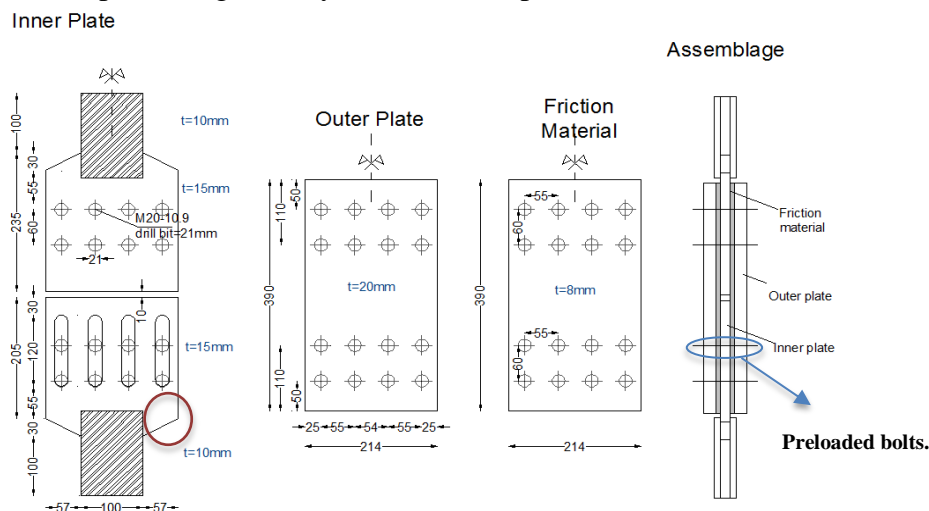


Figure 3.1: Dimensions of the experimental specimen.

The experimental program adopted for the two relevant friction interfaces is presented in Figure 3.2. Experiments performed for each specimen were divided in several tests, each using a different torque. For both metallic interfaces studied, three tests were made, which means that three levels of normal forces were applied. Each test was performed for a specific torque applied to the 4 bolts belonging to the second row (Figure 3.1). The tightening torques have been applied at the end of each loading sequence using a calibrated torque wrench. For each test or sequence, the displacement history was applied through 10 cycles, using different displacement amplitudes.

Additionally, in all loading sequences, a constant frequency of 0.25 Hz was adopted and, therefore, a variation of the displacement amplitude leads to an adjustment of the sliding velocity.

Interface	Torque	Number of bolts of friction pad	Number of cycles of the sequence	Amplitude
Steel-steel	200 N m	4	10	±30 mm
	300 N m		10	
	500 N m		10	
Sprayed aluminum-steel	200 N m	4	10	± 15 mm
	300 N m		10	
	400 N m		10	

Figure 3.2: Summary of the tests of the experimental program carried by Salerno University – Metallic interfaces (adapted from Latour et al., 2014.b)

Results obtained for both interfaces are depicted in Figure 3.3 and Figure 3.4. They report the hysteretic behaviour of the specimens, represented in terms of friction coefficient versus displacement. The friction coefficient was determined according to:

$$\mu = \frac{F}{mnN_b} \quad (3.1)$$

in which m is the number of surfaces in contact, n is the number of bolts, N_b corresponds to the bolt preloading force and, F is the sliding force. Italian standard CNR- UNI 10011(1997) recommends **equation (3.2)** for the calculation of the preloading force.

$$N_b = \frac{T_b}{k.d} \quad (3.2)$$

where T_b is the value of the tightening torque, d represents the nominal diameter of the bolt and k is the torque coefficient defined as the term which depends on friction coefficients, lead and thread angles, and on the diameter of the bolt. This coefficient assumes frequently the value of 0.2.

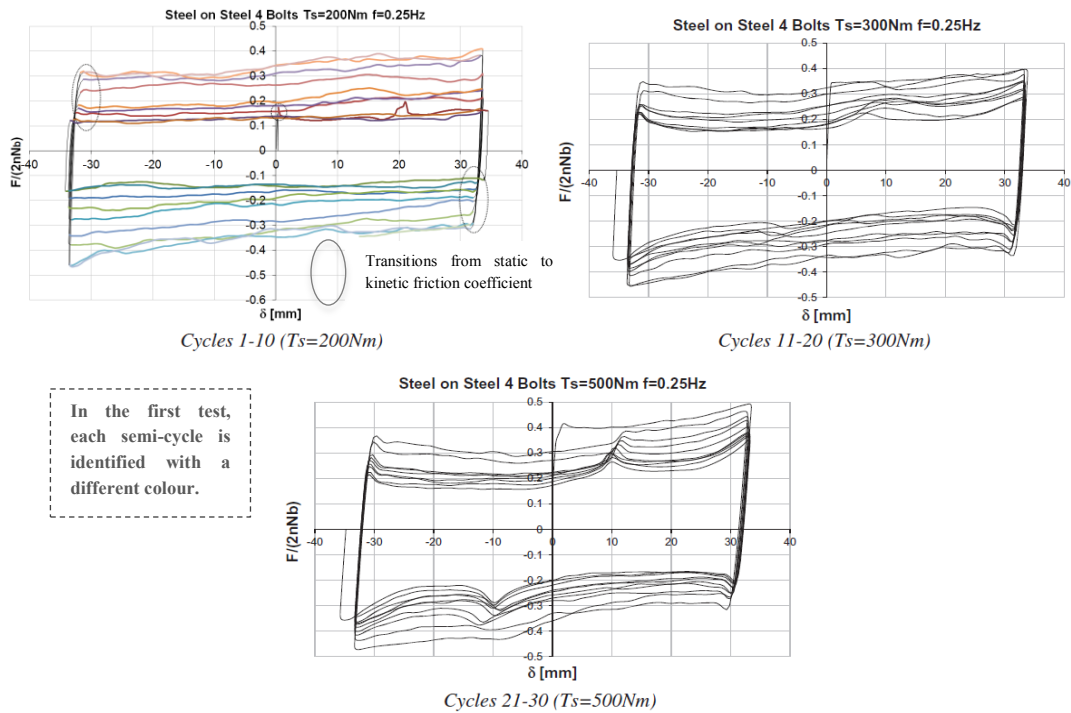


Figure 3.3: Friction coefficient versus displacement curves for steel on steel interface. (Latour et al., 2014.b).

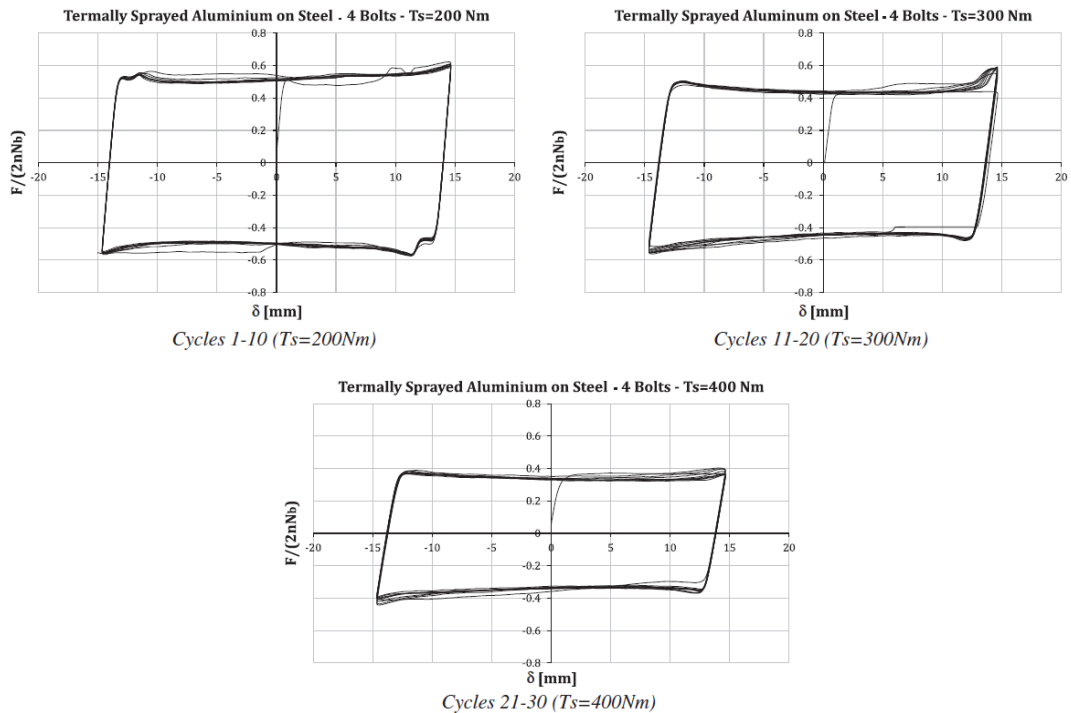


Figure 3.4: Friction coefficient versus displacement curves for sprayed aluminium on steel interface. (Latour et al., 2014.b).

After sliding, some complex phenomena resulting from the variation of asperity interlocking, ploughing conditions and variation of the bolt preload have significant

influence on the friction coefficient. Its modulus allows better the evaluation of the friction amplitude and to better understand the softening and hardening behaviours occurring during the tests. Thus, in terms of the friction coefficient variability, one can analyse the non-dimensional friction coefficient, which is given by:

$$\bar{F} = \frac{|F|}{mnN_b} \quad (3.3)$$

In Figure 3.5, the non-dimensional friction coefficient is a function of the semi-cycle number.

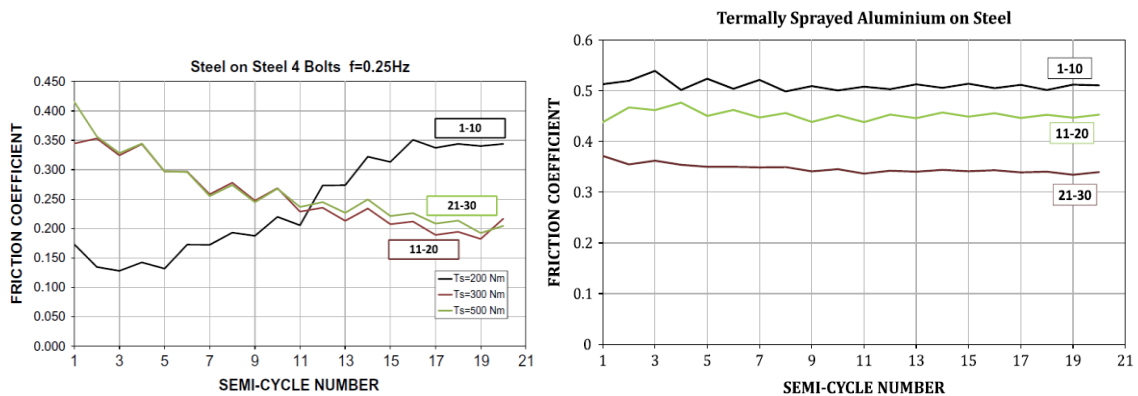


Figure 3.5: Non-dimensional force as a function of the semi-cycle number- Metallic interfaces (Latour et al., 2014.b).

Further conclusions and observations can be reported by analyzing these experimental results.

For steel on steel interface, it is possible to observe that the friction coefficient varies significantly in each sequence, as the number of cycles increase. In the first sequence, the kinetic friction coefficient is increasing due to three possible phenomena. The first one is related to the strain-hardening of the asperities in contact because those zones are subjected to plastic deformation which will work harden them, increasing their shear strength. The second one is associated with the fact that the ploughing component of friction has a significant contribution when two identical metals are sliding against each other. The hardened junctions will difficultly be sheared and the surface damage will be severe. Finally, the particles entrapped between asperities due to damage of the metal surface can also increase the sliding resistance.

In the following sequences, this tendency reverses as an increase of the semi-cycle number provokes a decrease of the friction coefficient. That variation of the friction coefficient may be related with the loss of the preloading force due to wearing of the material. In fact, the friction coefficient may even have a constant value. However as

the normal load was not controlled and measured, its variation is indirectly reported on the friction coefficient values.

These two tendencies can be explained by the laws of friction, although one cannot be certain of all phenomena developed at the interface. On the other hand, a much more difficult understanding is inherent to the variations of the static friction coefficient. In fact, the static friction coefficient is given by $\mu = s_0/\sigma_0$, where s_0 represents the critical shear stress of the material and σ_0 is the respective hardness. As a plastic deformation of the asperities is expected for metallic interfaces, the static coefficient of friction should remain constant. The fact that this value is also increasing at the beginning of each sequence can be related with the strain hardening suffered by steel asperities and with severe damage on the interface, in such a manner that the number of particles entrapped between the two surfaces is significant, affecting the overall behaviour of steel. However the results should be confirmed with further experimental tests.

In the case of sprayed aluminium on steel, that friction coefficient remains approximately constant for each sequence, meaning the variation of the normal load is not significant as the number of cycles increase. Nevertheless, the difference of the friction coefficient is well marked as the preloading force increases.

One can notice the dependence of the friction coefficient when varying the pressure applied to the surfaces.

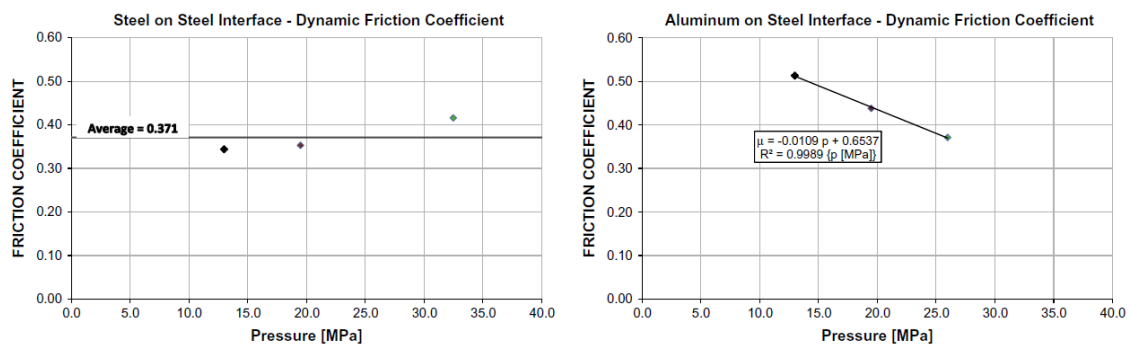


Figure 3.6: Friction coefficient versus pressure applied to the metallic surfaces (Latour et al., 2014.b).

It is possible to observe that the dynamic coefficient regarding steel on steel interfaces is not significantly affected by the normal pressure applied to the surfaces whereas aluminum on steel interface is strongly affected by the contact pressure. That proves that Amontons' law ceases to apply to surfaces covered with thin metallic films as the friction coefficient decreases with the applied normal force. In fact, by covering a

hard material with a softer one, a small area of contact is achieved because the load is borne by the hard metal. However, shearing occurs in the softer material, which leads to a lower value of the shear strength. For these reasons, both A and s are small, given origin to a small friction. As a result, an increase of load may origin only a small increase of the shear contact area and consequently a small rise in the frictional force. Therefore, the friction coefficient will diminish as the normal load increases. An excessive loading will ultimately lead to the breakdown of the aluminum film and increase the steel-steel interaction.

3.3. Modelling friction problems in Abaqus software

3.3.1. Introduction

Before starting the finite element analysis of the innovative friction device, further understanding of the methods used by Abaqus software in simple problems of friction is necessary. To achieve them, a simplified model, given by an assemblage of three plates was analysed. The geometry of the simplified numerical model is depicted in Figure 3.7.

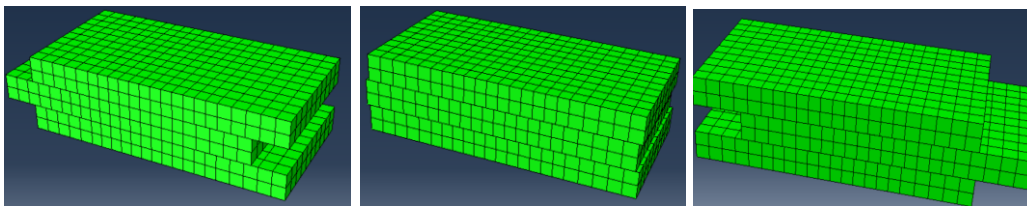


Figure 3.7: Geometry of the simplified model of friction.

A normal pressure was introduced on the outer plates and the inner plate was subjected to imposed displacements. After the first step, where the normal pressure is activated, an imposed displacement of 30/-30 mm is applied. The objective was to measure the sliding force required for initializing the movement.

Both surfaces were considered to be made of steel S275 and a friction coefficient equal to 0.170 was introduced for the contact properties. The pressure and apparent area of contact were modified and Amontons' and Coulomb's laws of friction for the generic cases of two metallic surfaces subjected to quasi-static tests were validated.

However, these “laws of friction” cease to apply for numerous cases. Therefore, to precise and validate the output values obtained with FE methods in complex friction problems, adequate models as well as experimentally determined coefficients of friction are required (Kloecke et al., 2015). With reference to the simplified model

used, one noticed that the material behaviour introduced in Abaqus has no direct influence on the tangential behaviour. The tangential behaviour introduced does not consider directly the plastic flow of the asperities, their strain hardening, the adhesion and ploughing phenomena, the surface finish, and so on. For these reasons, the material behaviour introduced in Abaqus is not of main interest for this work as the relevant results will be mainly influenced by the contact properties defined in the interaction section.

Most of the tribological interactions physically occurring are far from being understood and not sufficiently covered by FE models. However, some approaches can indirectly introduce the friction coefficient variations. If the Coulomb approach is adopted as for this simplified model, the input friction coefficient will remain constant as the load history proceeds.

Nevertheless, in the Abaqus software, there are some available methods one can adopt in order to model friction coefficient variations, necessary for the reproduction of more complex phenomenon:

- Consider the implementation of contact pressure, slip rate or temperature dependent data for Coulomb's friction model by introducing tabular data;
- When stick-slips transitions are relevant for the analysis, Abaqus provides a formulation that involves static-to-kinetic exponential decay;
- A user defined formulation using subroutines FRIC, VFRIC and FRIC_COEF can provide more accurate relations for the friction coefficient with reference to the contact pressure, slip rate and temperature variations. Besides that, those subroutines can vary friction with reference to other variables defined by the user;
- Modifying the Coulomb friction model by introducing additional information into the script file when the subroutines referred above are too complex.

In this case, slip-rate or temperature were not considered as variables in the tests made in Salerno and the normal pressure was not measured during each test. Therefore, using tabular data by varying these three variables or using Abaqus subroutines was not of great interest in this work.

Additionally, as the experiments were performed for large displacements, stick-slip transitions were not relevant because they would not introduce significant changes on the total energy dissipated (see Figure 3.3). Therefore, those transitions were neglected, and only the kinetic friction coefficient was introduced, which is considered constant for each semi-cycle.

The adopted procedure to model friction consists in the development of a Script file in which the friction properties are modified during the analysis and where transitions from stick to slip phases are neglected.

For each sequence, a new model was created, giving origin to six numerical models, three for each interface tested.

3.3.2. Scripting in Abaqus

The Abaqus Scripting Interface is an application programming interface (API) to the models and data used by Abaqus. It will be used to:

- Modify the friction coefficient during each test sequence;
- Automate repetitive tasks;
- Perform parametric studies;
- Create, modify and submit analysis jobs;

Abaqus scripting interface is an extension of the popular object-oriented language called python. Therefore, understanding the python language was a necessary tool for this numerical work.

Two scripting possibilities were considered for modelling each loading sequence. The first script hypothesis allows friction variation by using the RESTART function in Abaqus. The restart information will start the analysis using data from the previous analysis. By using energy correlations, the friction coefficient modifications are obtained and used in the following semi-cycles.

The energy dissipated at each semi-cycle can be simply calculated considering the friction coefficient value, μ , the displacement introduced, δ , and the normal load applied, N :

$$E_{diss} = \mu \cdot N \times \delta \quad (3.4)$$

The relation between the cumulated energy dissipated and the friction coefficient can be obtained from the experimental results.

$$\mu_{i+1} = f(\mu_{ini}; E_{diss,cum}) \quad (3.5)$$

A scheme of this first numerical procedure is presented in Figure 3.8.

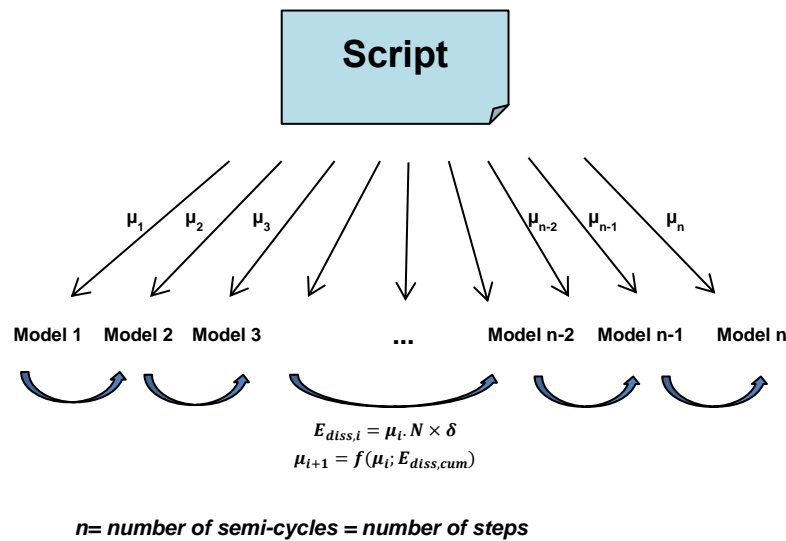


Figure 3.8: Scheme for the first Scripting Hypothesis.

The second Script hypothesis consists in creating a unique model, that accounts for the friction variation through modifications in the input file. In Abaqus GUI (“Graphical User Interface”) there are no available options for considering friction variations besides introducing tabular data with reference to normal pressure, slip rate or temperature data. However, Abaqus allows the user to introduce an amplitude function to model friction coefficient variations by changing the input file as follows:

```
*CHANGE FRICTION, INTERACTION = name, AMPLITUDE = amp_name
*FRICTION
, μini
```

The scripting interface would be used for creating the input file and for its modification using “write” commands. The amplitude function would be created considering the same energetic relations reported above for the first scripting hypothesis.

The second solution would be easily applied for more complex displacement history as all friction changes are reported in an amplitude function. Therefore, experimental results should be carefully studied in order to develop accurate relations between the total energy dissipated at the friction damper and the friction coefficient.

On the contrary, using the RESTART function becomes more difficult when the loading history increases its complexity. As a matter of fact, the loading history applied to the friction component herein analysed is very simple, whereas the loading history applied to the connection equipped with the friction damper is far more

complex. Besides this, the number of created models is equal to the number of semi-cycles. Having a significant number of cycles will generate a big number of models.

However, after trying the second approach, controlling friction variations proved to be impossible. The following problems were identified:

- Only amplitudes with monotonically increasing values between 0.0 and 1.0 were allowed. However, positive values would only lead to decreasing values of the friction coefficient. Therefore, it would never be possible to represent hardening behaviours;
- The referred amplitude function reports friction changes evolution and not the friction evolution. Therefore, a value of 1.0 in the amplitude function would bring the friction coefficient down to zero, while a value close to zero should have no influence in the friction coefficient. However, when using a value close to zero, unstable results were obtained.

Therefore, the first scripting approach was adopted. In order to introduce the RESTART function, the following code was written in a script.

```
#Define function responsible for RESTARTING the new model from the previous one
def copyModel(oldModel,friction, boundaryDisp):

    #Rename the model. For example, creating Model-2 from Model-1: newModel = Model-2; oldModel = Model-1
    newModel = oldModel.split("-")[0] + "-" + str(int(oldModel.split("-")[1])+1)
    print("Creating model %s, from model %s, with a friction coefficient of %s, and displacement of %s mm")
    %(newModel, oldModel, friction, boundaryDisp)

    #Rename the Job. For example, creating Job-2 from Job-1: newJob = Job-2; oldJob = Job-1
    newJob = "Job-" + str(newModel.split("-")[1])
    oldJob = "Job-" + str(oldModel.split("-")[1])

    #Rename the Step. For example, creating Step-3 from Step-2: newStep = Step-3; previousStep = Step-2
    newStep = "Step-" + str(int(newModel.split("-")[1])+1)
    previousStep = "Step-" + str(int(oldModel.split("-")[1])+1)

    boundaryDisp = float(boundaryDisp)
    friction = float(friction)

    #Copy the Previous Model
    #mdb.Model(name='Model-2', objectToCopy=mdb.models['Model-1'])
    mdb.Model(name=newModel, objectToCopy=mdb.models[oldModel])

    #Change model attributes, using the RESTART function.
    #mdb.models['Model-2'].setValues(restartJob='Job-1')
    mdb.models[newModel].setValues(restartJob=oldJob, restartStep=previousStep)

    #create step
    #mdb.models['Model-3'].StaticStep(name='Step-3', previous='Step-2', initialInc=0.001)
    mdb.models[newModel].StaticStep(name=newStep, previous=previousStep, initialInc=0.001)

    #create restart info
    mdb.models[newModel].steps[newStep].Restart(frequency=0, numberIntervals=1, overlay=ON, timeMarks=OFF)

    #new boundary condition. Changing the displacement amplitude for the cyclic analysis.
    #mdb.models['Model-3'].boundaryConditions['BC-2'].setValuesInStep(stepName='Step-3', u2=30.0)
    mdb.models[newModel].boundaryConditions['BC-2'].setValuesInStep(stepName=newStep, u2=boundaryDisp)
```

```

#Changing friction properties in the tangential behaviour of the relevant interaction.
mdb.models[newModel].interactionProperties['Int-1'].tangentialBehavior.setValues(table=((friction, ), ))

#create job & write input

#RESTART = RESTART
#PERCENTAGE = PERCENTAGE
#ODB = ODB

dropJob = mdb.Job(name=newJob, model=newModel, description='', type=RESTART,
    atTime=None, waitMinutes=0, waitHours=0, queue=None, memory=90,
    memoryUnits=PERCENTAGE, getMemoryFromAnalysis=True,
    explicitPrecision=SINGLE, nodalOutputPrecision=SINGLE, echoPrint=OFF,
    modelPrint=OFF, contactPrint=OFF, historyPrint=OFF, userSubroutine='',
    scratch='', multiprocessingMode=DEFAULT, numCpus=1, numGPUs=0)

dropJob.writeInput(consistencyChecking=OFF) #Create INPUT File
mdb.jobs[newJob].submit(consistencyChecking=OFF) #Run JOB
mdb.jobs[newJob].waitForCompletion() # Do not allow modifications while running the model
print ("New job: %s input file was created"% (newJob))

```

Figure 3.9: Introduction of the RESTART function in the Script.

3.4. Modelling preloading forces in Abaqus

The main parameters that define the sliding resistance of the friction device are the friction behaviour of the materials used and the normal load transmitted to the friction interfaces. Friction interactions in Abaqus were already analysed in the first simplified model. Therefore, another simplified model was created in order to study the application of preloading forces in Abaqus.

This simplified model is presented in Figure 3.10. It is possible to observe that two types of holes geometries were analysed, one with slotted holes and another with normal sized holes. Three plates with the same thickness were pressed against each other considering one prestressed bolt.

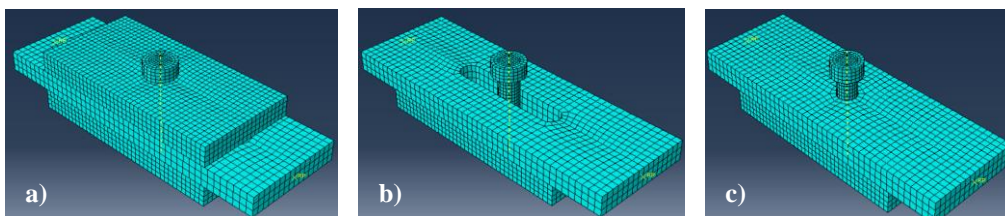


Figure 3.10: Simplified model used for the evaluation of the application of preloading forces in Abaqus: a) Global geometry of the model; b) Model with slotted holes; c) Model with normal sized holes.

Abaqus allows the application of preloading forces in bolts by using the “bolt load” option presented in the load module. Two methods are available for its application.

The first one considers the application of a concentrated load while the second one allows a prescribed change in the bolt length. Due to convergence problems related with the first option, a change of the bolt length was applied. Figure 3.11, shows an example of the application of this load.

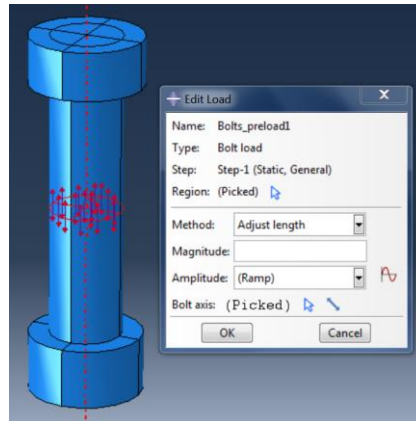


Figure 3.11 Modelling a pre-tensioned bolt in Abaqus.

When tightening bolts in experimental test set-ups by using calibrated torque wrenches, the load is directly transmitted to the bolt. However, in this case, as a deformation is introduced instead of a force, not all the imposed deformation is transmitted to forces due to further deformation of the plates. Therefore, it is not enough to calculate the extension of the bolt that provokes a certain bolt pressure, considering the bolt in the elastic range:

$$\varepsilon_{bolt} = \frac{\Delta L_{bolt}}{L_{bolt}} \quad (3.6)$$

$$\varepsilon_{bolt} = \frac{\sigma_{bolt}}{E} \leftrightarrow \Delta L_{bolt} = L_{bolt} \cdot \frac{\sigma_{bolt}}{E} \quad (3.7)$$

Results must be calibrated with the numerical results obtained. For this, besides the influence of the bolt geometry, also the effect of changing the thickness of the plates was analysed and different meshes were evaluated. Eleven geometries were analysed through varying the plate's thickness and, consequently, the bolt length, varying the bolt geometry and varying the mesh adopted, resulting in a total of 44 models. A more refined mesh was adopted for **Mesh 1** and a less refined mesh was associated to **Mesh 2**. The same adjusted length of 0.088 mm was applied for all models, and the expected pressure was calculated considering the theory of elasticity and a Young's modulus of 210 GPa for steel, while the obtained pressure was taken from numerical results. In Figure 3.12 is possible to observe the obtained results.

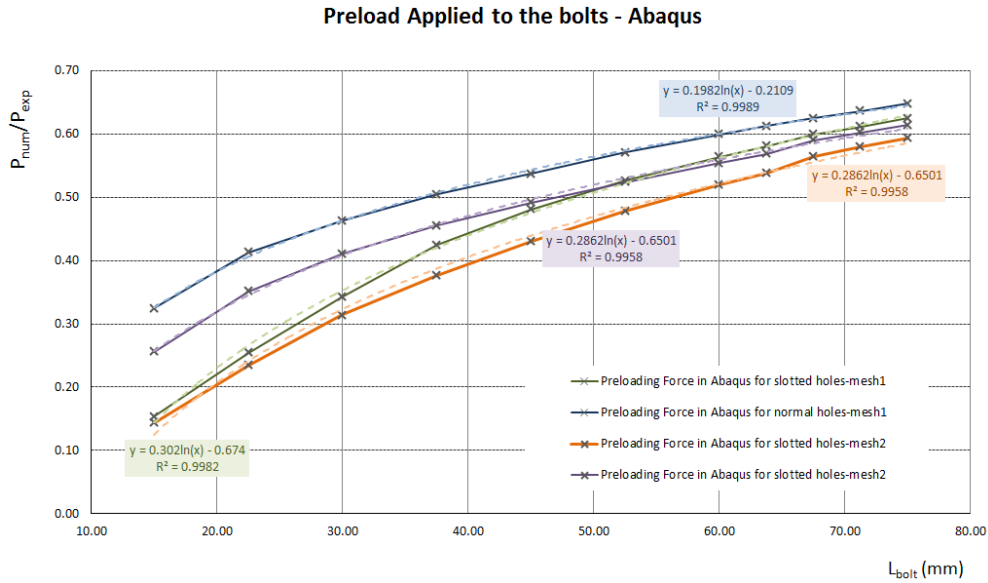


Figure 3.12: Ratio between the pressure obtained numerically and the expected pressure with reference to the length of the bolt.

Some considerations were taken from this analysis, which are important for the final friction device model:

- For a certain mesh and a certain bolt length, the enhanced adjusted length can be calculated based on the required pressure, by using a logarithmic approximation curve:

$$P_{num} = P_{required} \rightarrow P_{exp} \rightarrow \Delta L_{bolt}$$

- It is possible to conclude that a more refined mesh leads to more rigid elements and, consequently, the same adjusted length produces higher stresses in the bolt, or, using different words, greater preloading forces. Therefore, for each mesh, different calibrations should be considered.
- The geometry of the hole has also a big influence on the results as the contact area is smaller in the case of slotted holes (see Figure 3.13), meaning the same extension of the bolt produces bigger solicitations in the surrounding of elongated holes, and, therefore bigger deformations. Furthermore, as the thickness of the plates decreases, this influence is better marked because the deformation in the thickness direction gains more influence. On the contrary, for both hole geometries, as the thickness of the plates increases, the tendency towards a strain plane problem occurs, and the deformation happening in the thickness direction of the plates is no longer significant.

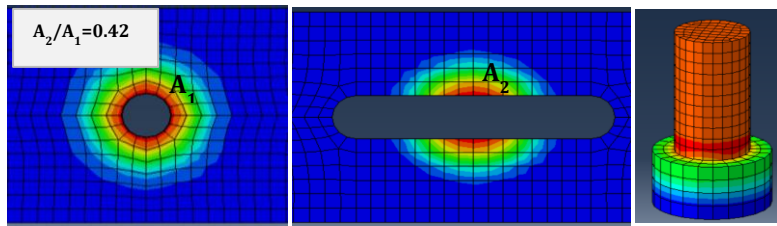


Figure 3.13: Distribution of the normal stresses in the bolts surroundings.

3.5. FEM model

This section presents the adopted friction model in detail. Firstly, the material's behaviour law is introduced, then the geometry of the model is presented, the adopted mesh is justified and steps, loads and boundary conditions defined.

More attention will be paid to the definition of the contact properties. For this, μ - $E_{\text{diss,cum}}$ relations will be derived from the experimental tests and introduced in the numerical model. At the end, results are presented and discussed.

3.5.1. Mechanical properties of the materials

3.5.1.1. Steel plates and bolts

Due to the fact all materials behave elastically, there is no need to fully describe the mechanical behaviour of the materials by means of coupon tests. However, further studies will evaluate the robustness of the suggested connection, proving the necessity to realize coupon tests for all materials.

In the numerical model, only the elastic behaviour was considered for the steel elements.

3.5.1.2. Friction material

Due to the fact that the abrasion of the friction interfaces has a significant influence on the results, damage evolution of these materials needs to be correctly modelled. That will be introduced by varying the friction coefficient during the analysis in accordance with the experimental results obtained. Although the most fitted approach would be modelling the wearing evolution of the materials by considering the microscopic phenomena developed when two surfaces slide against each other, that is extremely complex and not in the scope of this dissertation.

Therefore, in this numerical analysis, the behaviour of the friction materials is not of great importance as the relevant information is introduced in the tangential contact properties. Again, only the elastic properties will be introduced.

For both specimens, with and without sprayed aluminium, a steel plate with 8 mm thickness was used. As already referred, in the case of the sprayed aluminium-on-steel interface, although the shearing resistance is given by the sprayed aluminium asperities, the normal pressure is directly transmitted to the steel plate. Therefore, the behaviour of the sprayed aluminium material was only considered indirectly in tangential contact properties.

3.5.2. Geometry of the model

The geometry of the friction pad is approximately the same as the one used in the experiments. However, to reduce computer processing time, one symmetry boundary condition was adopted, reducing the size of the model to a half. The symmetry condition used is depicted in Figure 3.14.

Additionally, the angular edges identified in a red colour in Figure 3.1 were avoided due to the fact they can give origin to irregular finite elements. At the same time, the shape of the inner plate was defined in order to have approximately the same tension degradation as the original specimen.

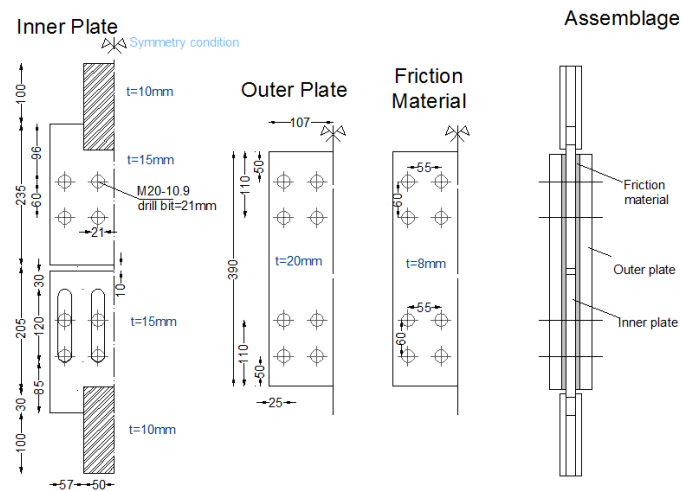


Figure 3.14: Scheme of the adopted geometry for the numerical model and definition of the symmetry used.

3.5.3. Adjustments of the bolts

Initially, only the monotonic behaviour was analysed in order to guarantee the static friction coefficient obtained in the experiments. The obtained results for the monotonic behaviour of steel-on-steel interface are depicted in Figure 3.15. One can observe that, before sliding occurs, small displacements were registered. Those small adjustments are related with small gaps between the bolt shanks and the edge of the bolt holes. At first, before overcoming the friction resistance between the two

surfaces, the outer plates and friction plates move together with the pulled inner plate. That gives origin to contact between the outer plates and the bolts fastening the outer plates to the fixed inner plate. After contact begins, the bolts start moving with the outer plates. Finally, the bolt shanks begin contact with the fixed inner plate. Therefore, the expected displacement before sliding occurs is twice the referred gap:

$$\delta_0 = 2 \times \frac{21-20}{2} = 1 \text{ mm} \quad (3.8)$$

Due to the fact that these displacements are irrelevant for the analysis, those 4 bolt holes were replaced by 20 mm holes. In Salerno experiments this problem was solved by increasing the torque applied to the bolts connecting the friction material and the outer plates to the fixed inner plate, until no initial displacements were reported.

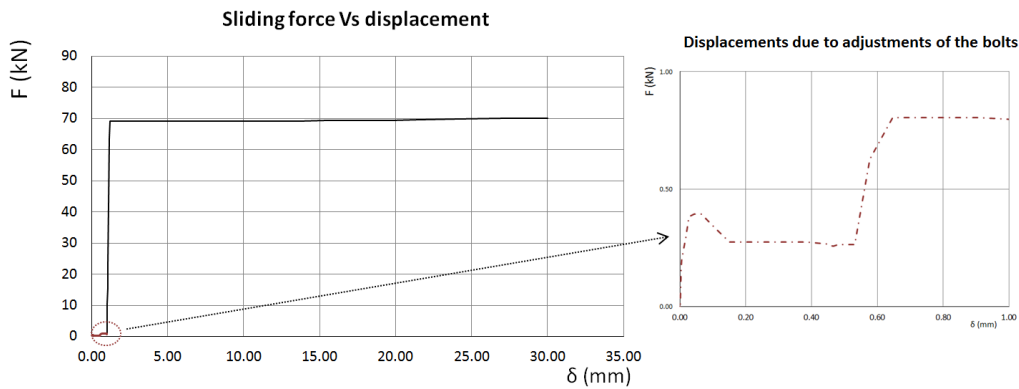


Figure 3.15: Sliding force times displacement – Steel on steel (Abaqus).

3.5.4. Mesh adopted

The finite element theory states that the numerical model will converge to the true solution if the number of elements in that region gets finer. For contact problems, this also holds true. However the cost of computation is always of concern and intelligent meshing decisions must be made. Thus, one must choose the adequate number of finite elements that allows the correct level of accuracy and reasonable results.

Furthermore, depending on the type of problem analysed, the type of finite elements to be used is of main importance. The finite element used is C3D8R (8 node, linear brick with reduced integration and hourglass control).

Additionally, no plane should only be defined with one element. Therefore, all plate's thickness should have more than one element.

As already analysed, the mesh size influences significantly the amplitude of the normal forces introduced into the friction interface. Calibration was performed for the preloading force applied in the case of the first sequence of steel-on-steel interface tests. As the pressure applied to the bolt varies linearly with the adjusted length introduced, no more calibration would be necessary for the geometry considered. The applied torque in the experimental procedure was equal to 200 N.m, leading to a normal force of:

$$N_b = \frac{200}{0.2 * 20} = 50 \text{ KN}$$

, which leads to a pressure of 159.15 MPa (considering the bolt shank with 20 mm of diameter). This was the target pressure. Six different models were analysed by considering six different meshes. In mesh 1, 2 and 3, only the bolt's mesh was changed whereas in case of mesh 4 and 5, only the plate's mesh was changed. This way, the influence of the bolt's mesh and plate's mesh was analysed separately. Finally, Mesh 6 was obtained by considering the influence of refining the outer plate's mesh in the contact between the bolts head and nut. In Figure 3.16, it is possible to analyse the variation of the bolt pressure obtained numerically with the introduced adjusted length, for the different meshes used.

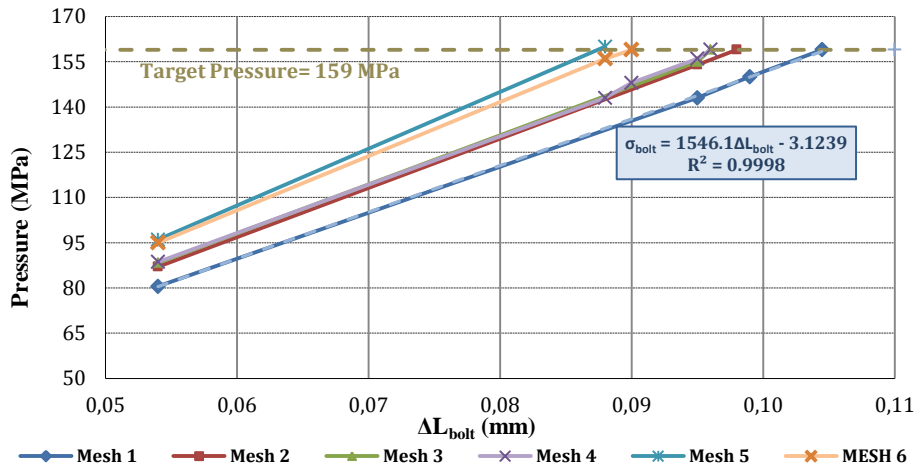


Figure 3.16: Pressure applied to the bolt with reference to the adjusted length introduced.

In fact, due to the additional elastic strain suffered by the plates, an increased variation of the length of the preloaded bolts needs to be considered in order to apply the same preloading force introduced in the experimental proceeding.

$$\Delta L_{total} = \Delta L_{bolt} + \Delta L^* \quad (3.9)$$

, in which ΔL^* represents the elastic deformation of all intermediate plates.

In Figure 3.17 is possible to analyse the influence of the element's number on the results and on the time consumption of the model.

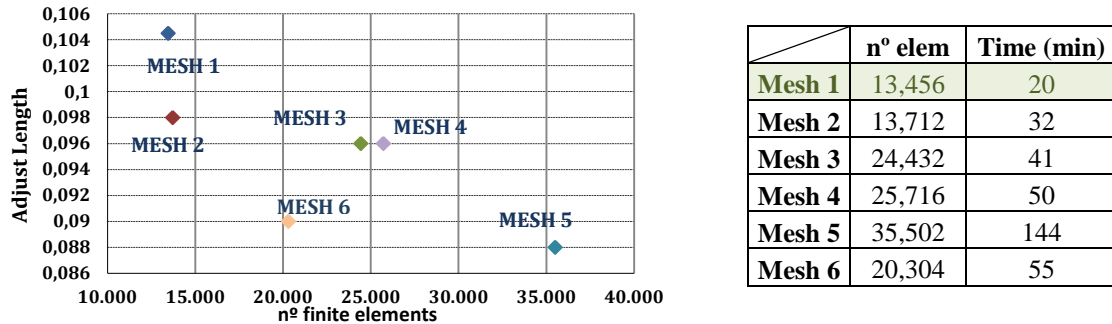


Figure 3.17: Sensitivity study.

By analysing the results, one can conclude that both, the bolt's mesh and the plate's mesh influence significantly the results. Mesh 6 was the one providing more accurate results with less finite elements. Mesh 5 is associated with less deformation of the steel plates. However, time endurance of the model exceeds two hours. Additionally, mesh 1 is the less refined mesh, leading to a more flexible behaviour of the plates. Therefore, for that mesh the necessary adjusted length is bigger than for the other models.

However, as results were calibrated for each mesh, the influence of the flexibility of the elements was already being taken into account. Therefore, calibration of the adjusted length would lead to similar results for all six models because the sliding resistance obtained for the friction device is given by coulomb's law, i.e., considering the same normal forces on the friction interface leads to the same results. For these reasons, Mesh 1 was considered. For the other sequences, the correct value of the adjusted length was obtained by equation (3.10), obtained by correlation.

$$\Delta L_{bolt} = \frac{\sigma_{bolt} + 3,1239}{1546,1} \quad (3.10)$$

The adopted mesh has 13,456 finite elements and takes approximately 20 min to initialize contact.

3.5.5. Steps

The initial step in contact analysis is usually the hardest step to establish convergence because the parts are not fully in contact. For the analysis to complete the first step, rigid body motions due to the lack of boundary conditions should be avoided.

Thus, due to the fact the analysed model involves preloaded bolts, its application should be defined as the first step, in order to initialize contact. In Table 3.1 and Table 3.2, the necessary adjust length to apply to the bolts is presented.

Table 3.1: Adjusted lengths of the preloaded bolts- steel on steel interface.

	Preloaded bolts: 4 - Mesh 1				
	T _b (N.m)	N _b (KN)	σ (MPa)	ΔL _{elastic} (mm)	ΔL _{numerical} (mm)
1 st seq.	200	50	159.15	0.054	0.105
2 nd seq.	300	75	238.73	0.081	0.156
3 rd seq.	500	125	397.89	0.135	0.259

Table 3.2: Adjusted lengths of the preloaded bolts- sprayed aluminium-on-steel.

	Preloaded bolts: 4 - Mesh 1				
	T _b (N.m)	N _b (KN)	σ (MPa)	ΔL _{elastic} (mm)	ΔL _{numerical} (mm)
1 st seq.	200	50	159.15	0.054	0.105
2 nd seq.	300	75	238.73	0.081	0.156
3 rd seq.	400	100	318.31	0.108	0.208

Other steps will be used for the application of the displacement history that describes the cyclic solicitation of the friction interfaces.

3.5.6. Displacements and boundary conditions

The displacement history was introduced with an imposed translation applied to a reference point constrained to the inner plate section through the usage of a rigid link constraint. However, at the first step that point is fixed and no displacements are allowed until the normal contact is achieved between surfaces. In further steps this boundary condition is modified. The opposite section of the inner plate is fixed in all three directions during all analysis.

3.5.7. Frictional behaviour – tangential contact properties

3.5.7.1. Energy considerations for friction variations

Energy is the main parameter that can evaluate friction variations because it is directly related to the relative displacements occurring between two sliding interfaces and takes into account the damage of the surfaces. Therefore, relations were derived based on the experimental results obtained, for steel-on-steel interface and for sprayed aluminium-on-steel interface, for each sequence.

Furthermore, as the results obtained experimentally sometimes exceeded the displacement amplitude imposed and considering the impossibility of introducing those variations on the numerical model due to the dimensions of the slotted holes, the energy approach allows to calibrate the friction variations with the correct displacement amplitude (30 mm in the case of steel-on-steel interface and 15 mm in the case of sprayed aluminium-on-steel interface).

Steel-on-steel interface

In Table 3.3 is possible to observe the friction variations by measuring the sliding forces for each semi-cycle and dividing them by the initial pressure applied to the bolts. The total energy dissipated is calculated considering the sliding force times the displacement achieved in the experimental procedure. Based on experimental results, correlations were developed and are presented in Figure 3.18

Table 3.3: Variation of the friction coefficient with the semi-cycle number – Steel-on-Steel.

Semi-cycle no.	1 st Sequence- N=200 Nm			2 nd Sequence- N=300 Nm			3 rd Sequence- N=500 Nm		
	$F_{(\delta=0)}$ [kN]	μ	$E_{diss,cum}$ [kNm]	$F_{(\delta=0)}$ [kN]	μ	$E_{diss,cum}$ [kNm]	$F_{(\delta=0)}$ [kN]	μ	$E_{diss,cum}$ [kNm]
0	0.00	0.000	0.000	0.00	0.000	0.000	0	0	0
1	48.49	0.121	1.625	206.19	0.344	6.80	415.56	0.416	13.5
2	-56.95	0.142	5.441	-199.92	0.333	20.00	-360.32	0.360	36.9
3	55.15	0.138	9.135	194.25	0.324	32.82	305.75	0.306	56.8
4	-53.86	0.135	12.744	-205.51	0.343	46.38	-330.92	0.331	78.3
5	52.44	0.131	16.257	179.61	0.299	58.24	271.60	0.272	96.0
6	-64.80	0.162	20.599	-174.15	0.290	69.73	-280.54	0.281	114.2
7	62.63	0.157	24.795	151.79	0.253	79.75	223.43	0.223	128.7
8	-76.39	0.191	29.913	-166.04	0.277	90.71	-257.01	0.257	145.4
9	71.82	0.180	34.725	151.23	0.252	100.69	221.78	0.222	159.8
10	-85.91	0.215	40.481	-165.31	0.276	111.60	-269.79	0.270	177.4
11	77.30	0.193	45.660	132.21	0.220	120.33	214.70	0.215	191.3
12	-113.43	0.284	53.260	-147.83	0.246	130.08	-246.07	0.246	207.3
13	105.29	0.263	60.315	114.81	0.191	137.66	211.15	0.211	221.1
14	-128.31	0.321	68.911	-132.08	0.220	146.38	-238.57	0.239	236.6
15	124.25	0.311	77.236	109.78	0.183	153.62	201.59	0.202	249.7
16	-138.43	0.346	86.511	-129.08	0.215	162.14	-219.92	0.220	264.0
17	137.31	0.343	95.711	98.87	0.165	168.67	186.48	0.186	276.1
18	-125.70	0.314	104.132	-119.72	0.200	176.57	-202.28	0.202	289.2
19	136.25	0.341	113.261	106.87	0.178	183.62	173.27	0.173	300.5
20	-137.35	0.343	116.008	-120.04	0.200	191.54	-200.71	0.201	314.0

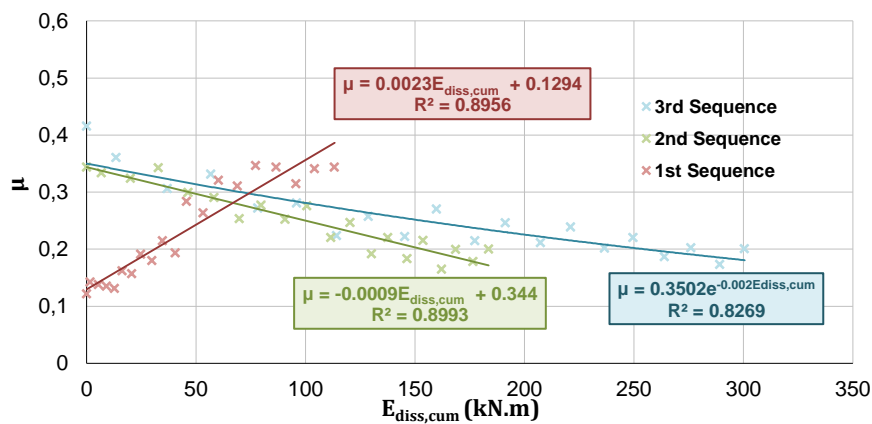


Figure 3.18: Friction coefficient times the cumulated energy dissipated - Steel on Steel interface.

By calling the RESTART function already created, the values determined with the later regression lines were introduced in the numerical models.

Sprayed aluminium-on-steel interface

The same procedure was adopted for the friction device using sprayed aluminium on the steel plates. As it was already explained, the geometry of the numerical model does not suffer any change. However, the frictional behaviour introduced in the tangential contact properties is modified according to the experimental results obtained for this specimen.

Table 3.4: Variation of the friction coefficient with the semi-cycle number – Sprayed aluminium-on-steel.

Semi-cycle no.	1 st Sequence- N=200 Nm			2 nd Sequence- N=300 Nm			3 rd Sequence- N=400 Nm		
	$F_{(\delta=0)}$ [kN]	μ	$E_{diss,cum}$ [kNm]	$F_{(\delta=0)}$ [kN]	μ	$E_{diss,cum}$ [kNm]	$F_{(\delta=0)}$ [kN]	μ	$E_{diss,cum}$ [kNm]
0	0.00	0.000	0.0	0.00	0.000	0.0	0.00	0.000	0.0
1	205.14	0.513	3.1	262.75	0.438	3.9	297.17	0.371	4.5
2	-207.89	0.520	9.3	-280.23	0.467	12.3	-283.87	0.355	13.0
3	215.67	0.539	15.8	277.03	0.462	20.7	289.73	0.362	21.7
4	-200.69	0.502	21.8	-285.93	0.477	29.2	-283.20	0.354	30.2
5	209.51	0.524	28.1	270.22	0.450	37.3	280.09	0.350	38.6
6	-201.57	0.504	34.1	-277.35	0.462	45.7	-280.06	0.350	47.0
7	208.56	0.521	40.4	268.36	0.447	53.7	279.14	0.349	55.3
8	-199.47	0.499	46.4	-273.71	0.456	61.9	-279.57	0.349	63.7
9	203.72	0.509	52.5	263.17	0.439	69.8	272.83	0.341	71.9
10	-200.23	0.501	58.5	-271.10	0.452	78.0	-276.39	0.345	80.2
11	203.23	0.508	64.6	262.93	0.438	85.8	269.29	0.337	88.3
12	-201.25	0.503	70.6	-271.79	0.453	94.0	-273.78	0.342	96.5
13	205.08	0.513	76.8	267.59	0.446	102.0	272.36	0.340	104.7
14	-202.27	0.506	82.9	-274.27	0.457	110.3	-275.16	0.344	112.9
15	205.59	0.514	89.0	269.42	0.449	118.3	273.07	0.341	121.1
16	-202.06	0.505	95.1	-273.41	0.456	126.5	-274.67	0.343	129.4
17	204.67	0.512	101.2	267.76	0.446	134.6	271.31	0.339	137.5
18	-200.60	0.501	107.2	-271.60	0.453	142.7	-272.43	0.341	145.7
19	204.81	0.512	113.4	268.09	0.447	150.8	267.54	0.334	153.7
20	-204.24	0.511	119.5	-271.67	0.453	158.9	-271.67	0.340	161.8

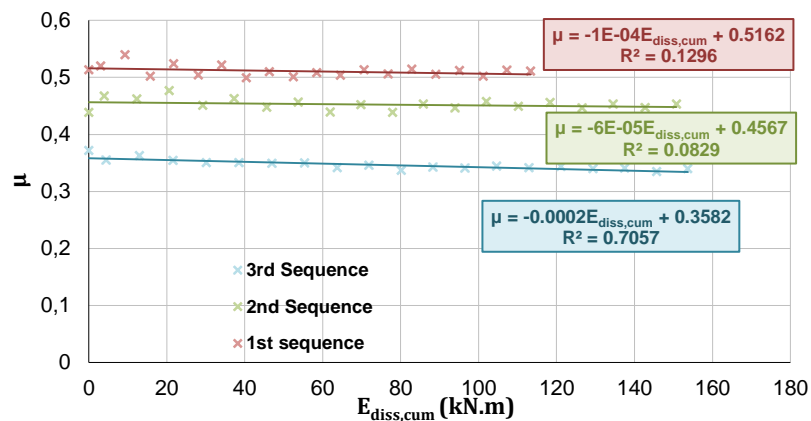


Figure 3.19: Friction coefficient times the cumulated energy dissipated – Sprayed Aluminium on Steel interface.

By observing Figure 3.19, one can conclude friction variations are very small for this interface, especially for the two first sequences in which the normal load is small. Therefore, for the two first sequences, a constant value for the friction coefficient was adopted, and there was no necessity of using the RESTART function. For the third sequence, the RESTART function was called 19 times.

3.5.8. Results

Displacement and reaction forces will be evaluated for the reference point attached to the movable face of the inner plate. Thus, the measured force corresponds to the friction force, which is the only one that opposes the applied displacement.

3.5.8.1. Force-displacement curve

For each loading sequence, the resulting force-displacement curve is obtained as presented in Figure 3.20 and Figure 3.21, for steel on steel interaction and sprayed aluminium on steel interaction, respectively.

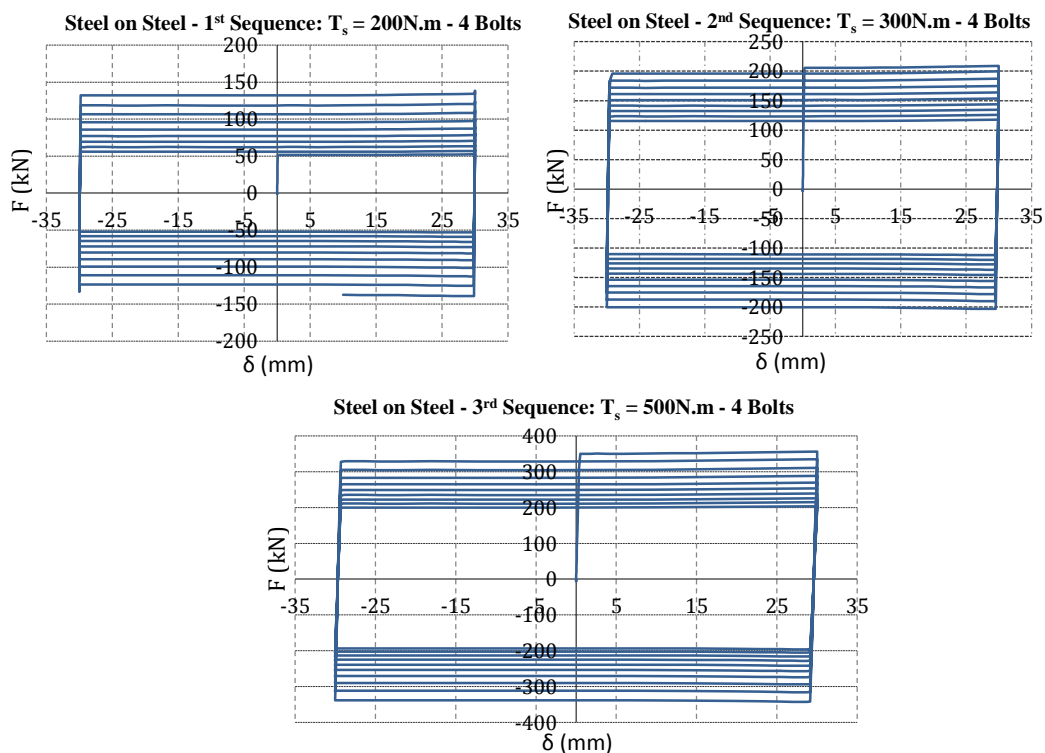


Figure 3.20: Cyclic behaviour obtained for steel-on-steel interface, for each sequence.

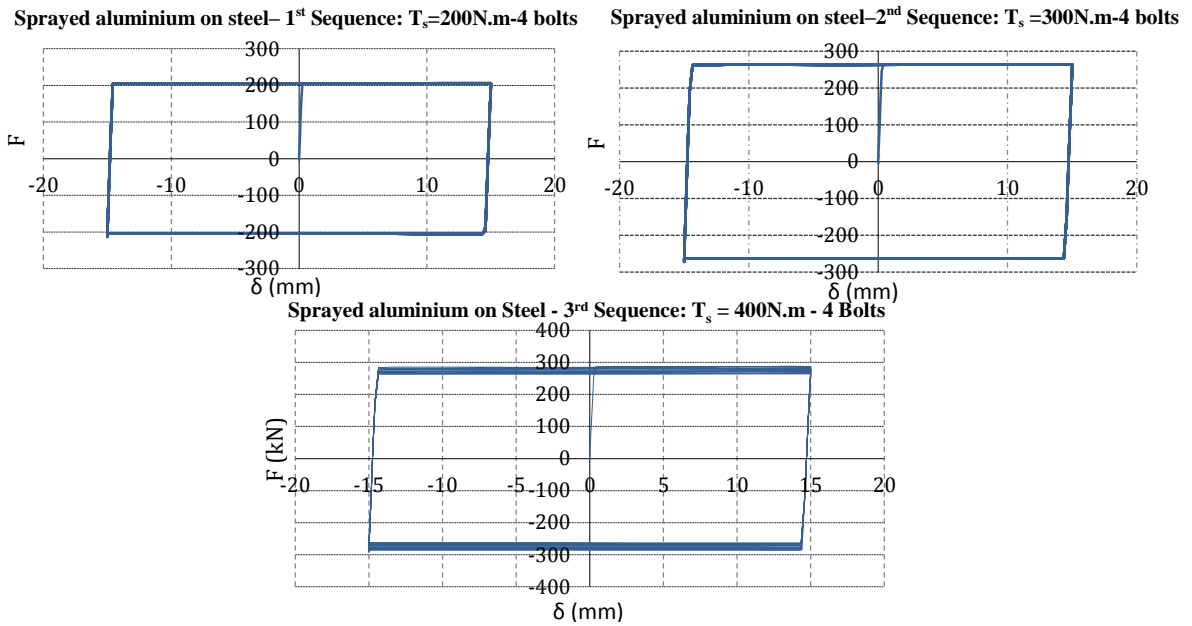


Figure 3.21: Cyclic behaviour obtained for sprayed aluminium-on-steel interface, for each sequence.

3.5.8.2. Energy dissipation capacity

The total energy dissipated through each loading cycle is summed up and presented in Figure 3.22 and Figure 3.23.

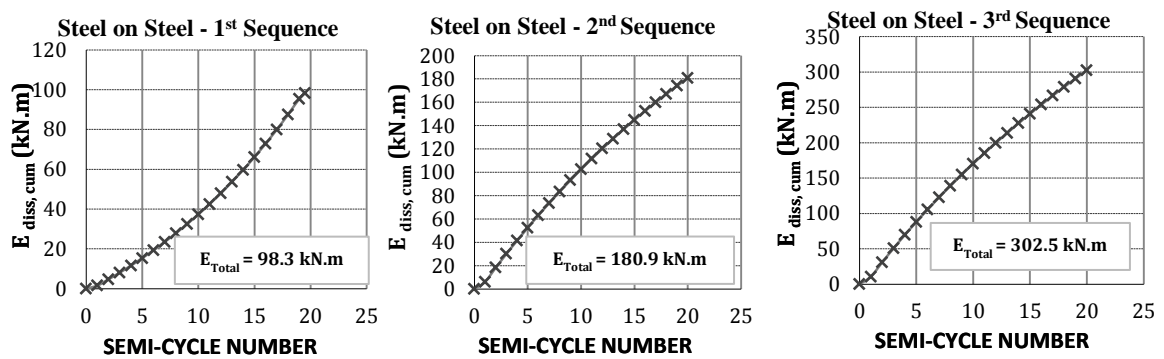


Figure 3.22: Cumulated energy dissipated times the semi-cycle number- Steel on steel.

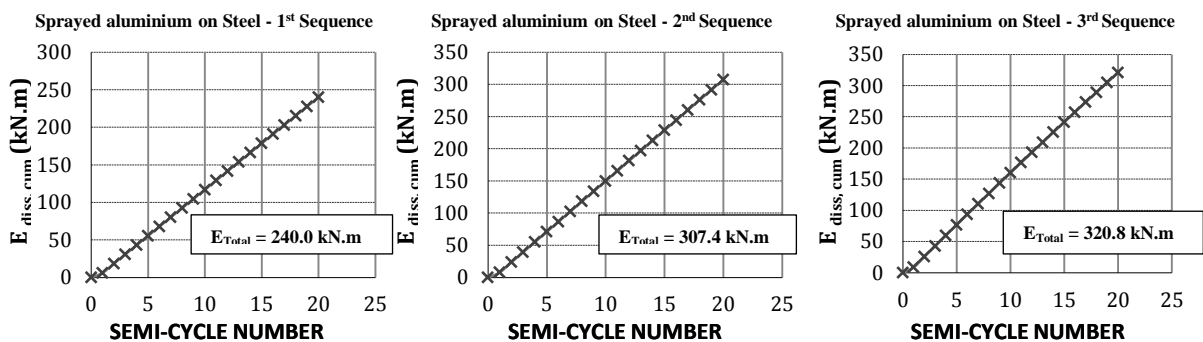


Figure 3.23: Cumulated energy dissipated times the semi-cycle number- Sprayed aluminium on Steel.

Finally, results are validated with the experimental ones by comparing the trend lines obtained on both when considering the friction variation with reference to the cumulated energy dissipated.

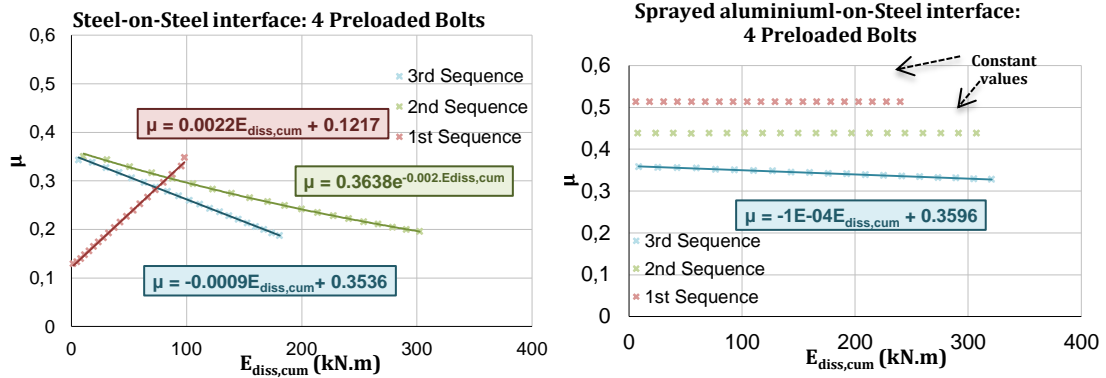


Figure 3.24: Friction coefficient times the cumulated energy dissipated – metallic interfaces.

Comparing the numerical obtained trend lines with the experimental correlations presented before, it is possible to conclude that a good agreement between both is obtained.

3.5.8.3. Wearing of the material

An estimation of the wearing of the materials can be done if the degrading behaviour is due to material loss. The loss of the friction coefficient is therefore reported as a loss of normal load due to wear of the metal surfaces. Thus, the loss of material is equal to the necessary variation of the length of the bolts. Following this assumption, the expected material wearing is reported in Table 3.5.

Table 3.5: Wearing of the friction materials.

Wearing-Steel-on-steel			Wearing-Sprayed aluminium-on-steel				
	1 st Seq.	2 nd Seq.	3 rd Seq.		1 st Seq.	2 nd Seq.	3 rd Seq.
μ_{FINAL}		0.187	0.196	μ_{FINAL}	0.513	0.438	0.328
$\mu_{INITIAL}$		0.343	0.350	$\mu_{INITIAL}$	0.513	0.438	0.358
$\mu_{INITIAL} / \mu_{FINAL}$		1.83	1.79	$\mu_{INITIAL} / \mu_{FINAL}$	1.0	1.0	1.1
$F_{N, ini}$ [kN]		75.00	125.00	$F_{N, ini}$	50.0	75.00	100.00
$F_{N, Fin}$ [kN]		40.92	69.86	$F_{N, Fin}$	50.0	74.93	91.65
ΔL_{bolt} [mm]		0.04	0.06	ΔL_{bolt}	0.00	0.00	0.01
ΔL_{plate} [mm]		0.04	0.06	ΔL_{plate}	0.0	0.00	0.01
% _{loss Material}		0.23%	0.37%	% _{loss Material}	No wearing	No wearing	0.06%

As expected, a heavy wearing can be expected for steel on steel interface, as the same metal is used for both surfaces in contact. However, further measurements should be made during the experiments due to the fact lots of variables can be influencing the degrading behaviour occurring.

3.6. Discussion of the numerical modelling

In order to simulate complex phenomenological problems, a full characterization of the tangential behaviour of the surfaces has to be performed and friction coefficients determined from experiments. These friction variations can then be introduced in more complex geometries, in which the same friction behaviour is expected, by using a RESTART function and by modifying the friction coefficient in accordance with considerations related to energy.

The friction simulation completed in the present work resulted in the expected outcomes, making it possible therefore to introduce the same approach to the overall connections, using these friction devices. However, the time required to run such analysis is not compatible with this work. Therefore, this approach will not be used in the subsequent numerical analysis of the connection.

4. COMPONENT APPROACH

4.1. Introduction

The aim of this chapter is to verify the design rules applied by the Salerno team to the innovative connection and to obtain the expected moment-rotation ($M-\phi$) curve that characterizes such connection.

The design rules for the dissipative joints are directly related to the capacity design concept, the principle of the component approach and the application of the two following principles:

- Resistant mechanisms must be designed according to the characteristics of the internal stress derived from structural analysis;
- Non-dissipative zones must be designed in order to remain in the elastic range and, consequently, must be sized up according to the envelope of the internal stresses that the dissipative zones, plasticized and hardened up to the limit of their ultimate strength, are able to transmit.

These two principles will govern the first part of this chapter. The geometry of the innovative connections designed by Salerno is defined based on the weakest component, which is the friction damper. This means the energy dissipation capacity and the shape of the $M-\phi$ curve should be mainly influenced by the friction properties of the sliding interface.

In the second part of the chapter, the suitability of the $M-\phi$ curves obtained is analysed by comparing them with the experimental ones.

4.2. Detailed description of the specimens

Specimen TSJ-SA300-320-CYC12 is a joint where the upper beam flange is connected to the column by using a normal T-stub whereas the lower beam flange is fastened to the column by means of a system of three L-stubs. In between the beam flange and the L-stubs, in order to realize the friction damper, a steel plate with a coating of 300 μm of sprayed aluminium is interposed.

The geometry of specimen TSJ-SA300-320-CYC 12 is illustrated in Figure 4.1.

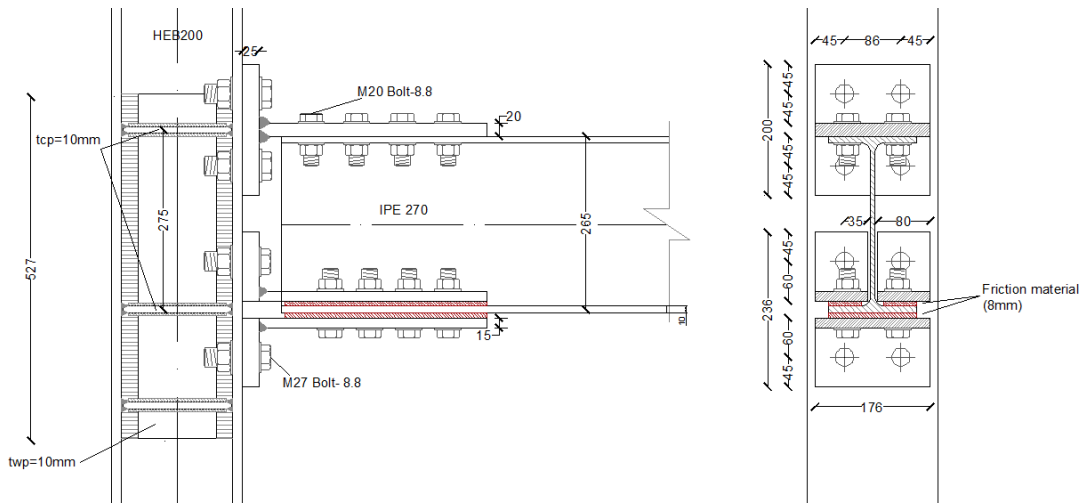


Figure 4.1: Geometry of specimen TSJ-SA300-320-CYC 12.

Specimen TSJ-H-SA300-260-CYC 13 is characterized by a detail very similar to the TSJ-SA300-320-CYC 12 specimen but, in this case, the friction damper is positioned in a beam haunch which is welded to the beam in order to increase the lever arm.

For the first connection, the lever arm was considered equal to 265 mm, while for the second connection that lever arm is equal to 411 mm. This last solution allows a reduction of the tightening torque. In a simplified way, a lower friction force can be provided by the friction dampers in order to obtain the same bending moment for the joint. The geometry of the second specimen is depicted in Figure 4.2.

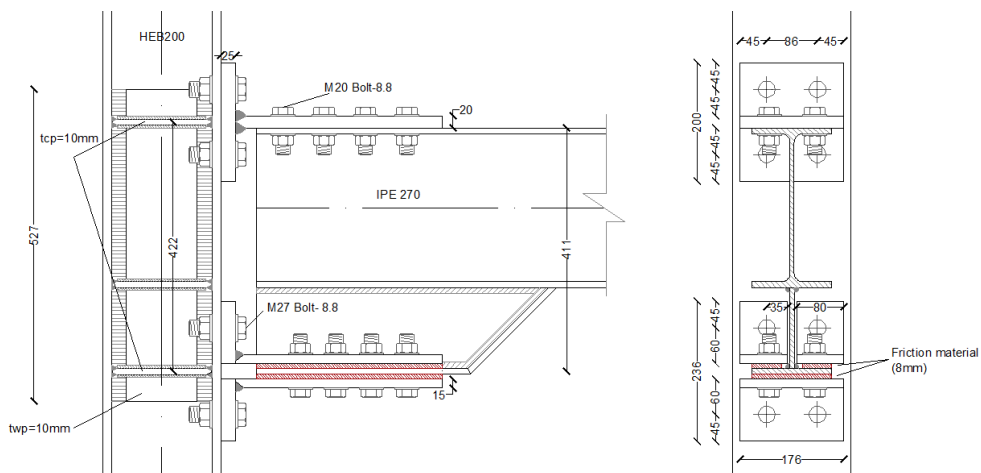


Figure 4.2: Geometry of specimen TSJ-H-SA300-260-CYC 13.

The geometry of the T-stubs and L-stubs, identical for both connections, is reported in Figure 4.3 and Figure 4.4, respectively.

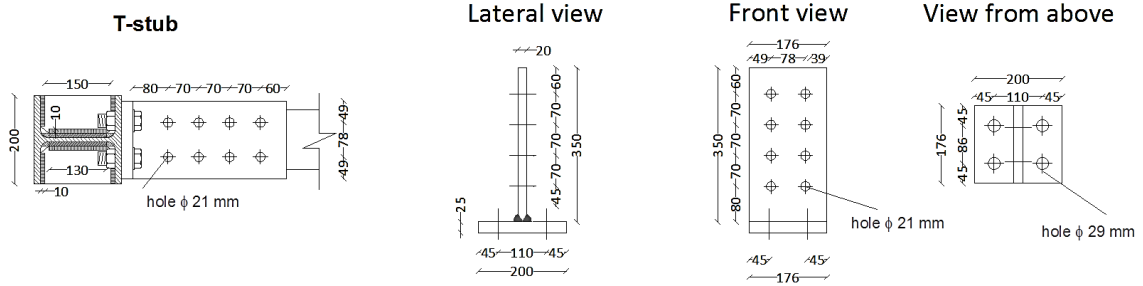


Figure 4.3: Geometry of the T-stub positioned on the upper flange of the beam.

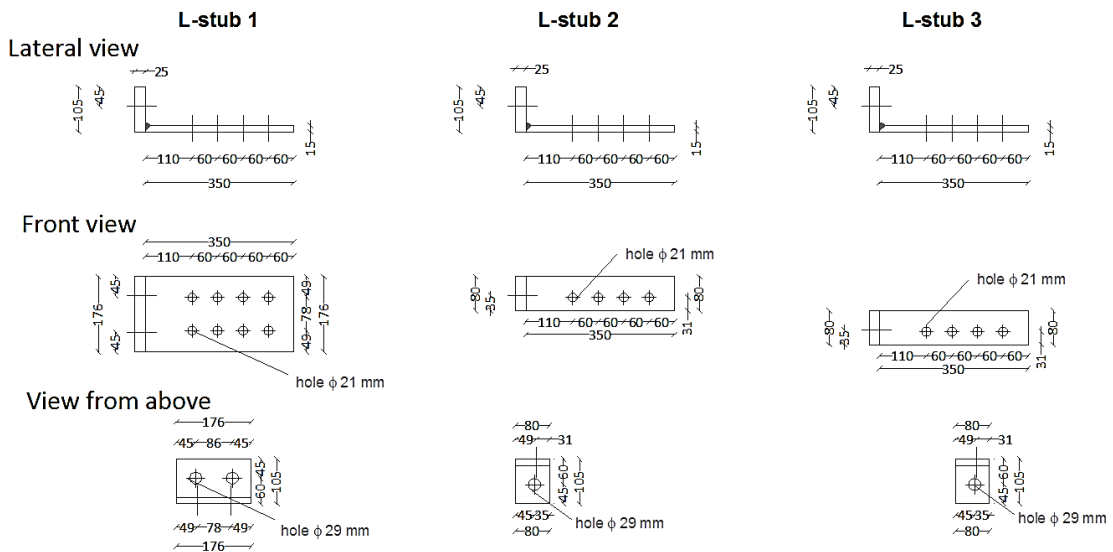


Figure 4.4: Geometry of the group of L-stubs positioned at the lower flange of the beam or haunch.

The beam and column are a IPE 270 and a HEA 200, respectively, both made of S275 steel. Additionally, all steel plates introduced in this joint are made with S275 steel. Figure 4.5 presents a scheme of the friction damper used in both specimens.

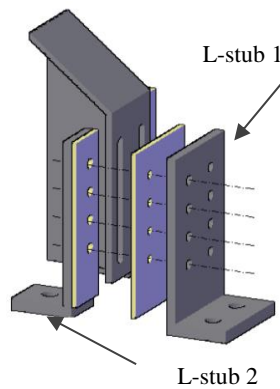


Figure 4.5: Scheme of the friction damper.

4.3. Verification of the design rules applied by Salerno

4.3.1. Introduction

All the adopted steps follow the guidelines referred in Eurocode 3: Design of Steel Structures - Part 1-8: Design of joints (CEN, 2005).

The design of the innovative double split connection respects the following steps:

1. Determination of the design stress;
2. Definition of the length of the slotted holes;
3. Design of the T-stub;
4. Check the L-stubs resistance;
5. Check the column web in compression;
6. Check the shear panel resistance;
7. Check the column flange resistance.

In order to define the design stresses it is further necessary to take into account the design rules applicable for connections located in seismic regions. According to EC8-1, a sufficient overstrength should be guaranteed for the non-dissipative components if:

$$M_{no-diss,jc,Rd} \geq 1.1\gamma_{ov}M_{diss,jc,Rd} \quad (4.1)$$

The factor 1.1 accounts for the effects of material strain hardening and the overstrength factor, γ_{ov} , accounts for random material variability. Eurocode 8 recommends a constant value of 1.25 for this factor.

In the case of the innovative joint, the friction device is the weakest component, for which no rules currently exist. However, the variability of the resistance of this component is mainly influenced by friction and normal pressure oscillations, which vary in a more restricted range than the material variability. For this reason, an overstrength factor equal to 1.25 was adopted for the non-dissipative components.

4.3.2. Determination of the design stresses

In order to control the slip resistance at the interface, the friction dampers are preloaded by means of eight high strength bolts properly tightened in order to achieve the required bending resistance.

The analysed joints were designed for a bending moment resistance equal to the beam plastic resistance. In case of the joint without any haunch, the plastic resistance is equal to $M_d=133$ kN.m whereas in case of the joint with the additional haunch, the

plastic resistance was increased by 25%, which results in $M_d = 166$ kN.m (Latour et al., 2014). Therefore, those were the resistance values adopted for the design of the friction dampers in each connection. The applied prestress was defined for each connection and a static friction coefficient between aluminium and steel interfaces equal to 0.4 was assumed, in accordance with the experimental measurements.

TSJ-SA300-320-CYC 12

$$T_{b,min} = \frac{0.2d \times F}{mn\mu \times k_s} = \frac{0.2 \times 20 \times \frac{133}{265 \times 10^{-3}}}{2 \times 8 \times 0.4} = 313.9 \text{ N.m}$$

$$T_{b,adopted-Salerno} = 320 \text{ N.m} \quad (4.2)$$

TSJ-H-SA300-260-CYC 13

$$T_{b,min} = \frac{0.2d \times F}{mn\mu \times k_s} = \frac{0.2 \times 20 \times \frac{166}{411 \times 10^{-3}}}{2 \times 8 \times 0.4} = 253.0 \text{ N.m}$$

$$T_{b,adopted-Salerno} = 260 \text{ N.m} \quad (4.3)$$

where k_s is a correction factor that takes the bolt geometry in consideration. The value advised by EC3-1-8 for the coefficient, in the case of normal clearance holes, is equal to one while for long open slotted holes this value should be reduced.

However, the coefficient k_s for slotted holes presented by EC3 was not used because it was also not considered in the experimental determination of the friction coefficient. This way, consistency was guaranteed with the experimental activity carried out on the joint friction component at Salerno University.

After defining the prestress applied to the bolts, the resistance of the friction pad, for each joint, is given by:

TSJ-SA300-320-CYC 12

$$F = T_u = C_u = \frac{T_b \times m \times n \times \mu}{0.2 \times d} = \frac{320 \times 2 \times 8 \times 0.4}{0.2 \times 20} = 512.0 \text{ kN} \quad (4.4)$$

$$M_{diss,jc,Rd} = F \cdot z = 512.0 \times 265 \times 10^{-3} = 135.7 \text{ kN.m} \quad (4.5)$$

TSJ-H-SA300-260-CYC 13

$$F = T_u = C_u = \frac{T_b \times m \times n \times \mu}{0.2 \times d} = \frac{260 \times 2 \times 8 \times 0.4}{0.2 \times 20} = 416.0 \text{ kN} \quad (4.6)$$

$$M_{diss,jc,Rd} = F \cdot z = 416.0 \times 411 \times 10^{-3} = 171.0 \text{ kN.m} \quad (4.7)$$

It is now possible to calculate the design forces for the non-dissipative components of both joints.

TSJ-SA300-320-CYC 12

$$M_{no-diss,jc,Rd} = 135.7 \times 1.25 = 169.6 \text{ kN.m} \quad (4.8)$$

$$F_{no-diss,jc,Rd} = \frac{135.7 \times 1.25}{265 \times 10^{-3}} = 640.0 \text{ kN} \quad (4.9)$$

TSJ-H-SA300-260-CYC 13

$$M_{no-diss,jc,Rd} = 171.0 \times 1.25 = 213.7 \text{ kN.m} \quad (4.10)$$

$$F_{no-diss,jc,Rd} = \frac{171.0 \times 1.25}{411 \times 10^{-3}} = 650.0 \text{ kN} \quad (4.11)$$

4.3.3. Definition of the length of the slotted holes

The friction damper has to be designed in such way that slippage between the friction interface and the beam flange is allowed. In order to accomplish that, the length of the slotted holes, made on the beam flange or on the haunch, has to be properly designed in accordance with the desired value of the joint rotation capacity.

$$L_{slot} = (n_{br} - 1)p + d_b + 2\phi z \quad (4.12)$$

where n_{br} corresponds to the number of bolt rows used to fasten the L-stub web to the beam flange or haunch, d_b is the bolt diameter, p is the bolt pitch, ϕ is the design value of the joint rotation capacity and z is the lever arm. By adopting four bolt rows totalling eight M20 bolts, with a pitch of 60 mm and by assuming a design joint rotation equal to $\pm 80 \text{ mrad}$, comes:

TSJ-SA300-320-CYC 12

$$L_{slot,min} = (4 - 1)60 + 20 + 2 \times 80 \times 10^{-3} \times 265.0 = 242.4 \text{ mm}$$

$$L_{slotted,adopt_Salerno} = 270 \text{ mm} \quad (4.13)$$

TSJ-H-SA300-260-CYC 13

$$L_{slot,min} = (4 - 1)60 + 20 + 2 \times 80 \times 10^{-3} \times 411.0 = 265.8 \text{ mm}$$

$$L_{slotted,adopt_Salerno} = 270 \text{ mm} \quad (4.14)$$

The same length of the slotted holes was used for both connections in order to simplify the manufacturing of the specimens. However, such a big length was not needed for the connection without the haunch.

4.3.4. Design of the T-stub flange – hogging moment

In order to control both the joint flexural strength and the plastic rotation supply, the plate's thickness and bolts strength and location must be conveniently detailed.

It is well know that the design resistance of a T-Stub is obtained as the minimum value between three failure modes:

- Flange yielding or Type-1 mechanism: Characterized by the formation of four plastic hinges, two of them located at the bolts axis due to bending moments caused by prying forces and the remaining two located at the flange-to-web connection;
- Flange yielding with bolts fracture or Type-2 mechanism: Characterized by the formation of two plastic hinges located at the same flange-to-web fillet. The other two hinges cannot be achieved because the bolt failure happens first;
- Bolts fracture or Type-3 mechanism: Characterized by bolts rupture only, without the development of any hinge because of the earlier detachment of the plates, which leads to decreased ductility.

In Figure 4.6, the three failure modes are depicted.

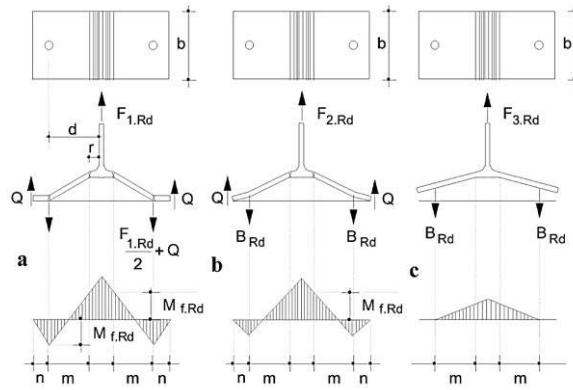


Figure 4.6: Failure modes of bolted T-stubs (Piluso et al., 2008).

4.3.4.1. Definition of the thickness of the T-stub flange

In order to prevent yielding of the T-stub, this element is designed to withstand a tensile force 1.25 greater than the one resisted by the friction damper. Additionally, ductility requirements are assured for failure mode type-1.

In order to obtain the total force of the T-stub, the contributions of the two bolt rows are summed up according to a plastic distribution of stresses (see Figure 4.7):

$$F_{T-stub}^{Type-1} = F1 + F2 = \frac{b_{eff}t_{ep}^2}{m_1} f_y + \frac{b_{eff}t_{ep}^2}{m_2} f_y \quad (4.15)$$

$$m_{eq} = \frac{m_1 m_2}{m_1 + m_2} \quad (4.16)$$

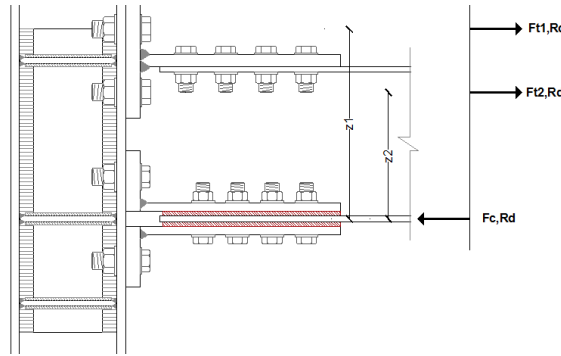


Figure 4.7: Plastic distribution of stresses.

To ensure this type of failure mode controls the behaviour of the T-stub, the thickness of the T-stub flange plate is restricted to a minimum value:

$$t_{ep,min} = \sqrt{\frac{F_{T-stub} m_{eq}}{b_{eff} f_y}} \quad (4.17)$$

The tensile force applied to the T-stub, F_{T-stub} , is equal to the design bending moment for non-dissipative components, divided by the lever arm. Therefore, for the connection without any haunch, a value of 640.0 kN was considered and, for the joint with a haunch, a value of 650.0 kN was obtained. The parameter m_i is the distance between the bolts axis of bolts line i and the plastic hinge located at the flange-to-web fillet (referred in Figure 4.6). For both bolt rows, m_i was considered equal to 45 mm, meaning $m_{eq} = \frac{m_1 \times m_2}{m_1 + m_2} = 22.50$ mm. The welds do not influence the value of m_i as they are full penetration welds. Furthermore, b_{eff} is equal to half of the plate's width, $b_{eff} = \frac{b}{2} = \frac{176}{2} = 88$ mm.

The minimum thickness required for the plates in the case of CYC 12 connection is 24.4 mm and in the case of connection CYC 13 is 24.6 mm. Therefore, a plate thickness equal to 25 mm was adopted for both joints.

For the selected geometry, the total resistance of the T-stub is equal to 672.2 kN, which corresponds to an overstrength factor of approximately 1.3, for both joints.

4.3.4.2. Definition of the bolts

In order to avoid the brittle failure of the bolts tightening the plates to the column flange, Type 3 mechanism cannot occur. On the other hand, in order to maximize the energy dissipation capacity, a Type-1 mechanism should be assured. Therefore, the parameter β_{Rd} governing the collapse mechanism typology given by the ratio between flexural strength of the flanges and axial strength of the bolts should verify the

following condition (4.18). In Figure 4.8 is possible to evaluate the relation between the parameter β_{Rd} and the type of failure mode.

$$\beta_{Rd} = \frac{4M_{pl,1,Rd}}{2B_{Rd}m_i} \leq \frac{2\lambda}{1+2\lambda} \quad (4.18)$$

where B_{Rd} is the bolt design resistance, $\lambda=n/m_i$ and n corresponds to the distance between the prying force and the bolt's axis, $n = e_{min} \leq 1.25m$ (referred in Figure 4.6). $M_{pl,1,Rd}$ is the plastic moment of the T-stub flange, which, in this case, depends on the effective width of a single bolt row, b_{eff} , on the thickness adopted for the plate and on its yield strength, f_y .

$$M_{pl,1,Rd} = 0.25b_{eff}t_p^2f_y \quad (4.19)$$

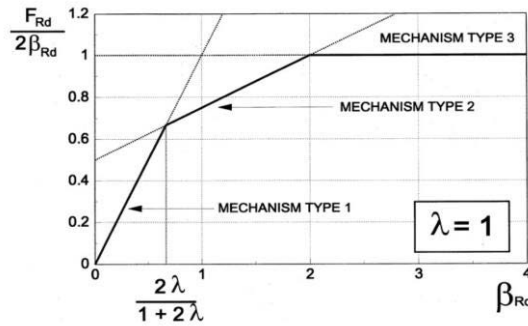


Figure 4.8: Types of failure mechanisms (Piluso et al., 2008).

By substituting the plastic moment of mechanism type-1 in this last condition, results:

$$B_{Rd} \geq \frac{\left(1 + \frac{n}{m_1}\right)b_{eff}t_p^2f_y}{4n} \quad (4.20)$$

$$B_{Rd} = \frac{K_2 \times f_{ub} \times A_s}{\gamma_{M2}} \quad (4.21)$$

where f_{ub} is the ultimate strength of the bolts, A_s is the tensile stress area of the bolt, k_2 was considered equal to 0.9 according to table 3.4 of EC3-1-8 and γ_{M2} is a safety coefficient used for bolted connections equal to 1.25.

A required tensile resistance of $B_{Rd} = 168.06 \text{ kN}$ was obtained. Therefore, M27 bolts of class 8.8 were adopted.

4.3.4.3. Geometric compatibilities

Due to geometrical conditions, two limit values should be considered for the distance between the two bolts in the same row, w_{min} and w_{max} , defined in equations (4.23) and (4.24) (Figure 4.9). Adopting the value of the edge distance, e , it is possible to define those limit values and the end-plate width.

$$e \geq 1.2 \times d_0 = 34.8 \text{ mm} \rightarrow e_{adopt} = 45 \text{ mm} \quad (4.22)$$

$$w_{min} = t_{cw} + 2r_c + 1.8d_0 = 9mm + 2 \times 18mm + 1.8 \times 29mm = 97.2mm \quad (4.23)$$

$$w_{max} = b_c - 2e = 110 mm \quad (4.24)$$

According to the above equations, the value for the distance w should remain between 97 mm and 110 mm. However, specimens tested in Salerno were produced with the following distance between the bolts:

$$w_{Salerno} = 86 mm \quad (4.25)$$

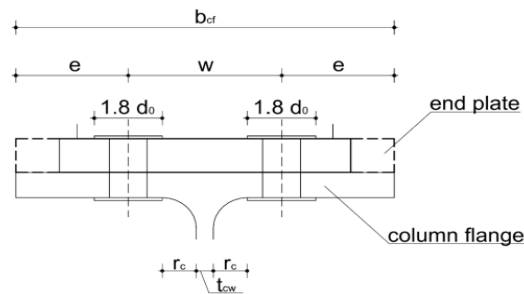


Figure 4.9: Geometrical conditions adopted for the bolts.

A contradiction between the limit values for w and the real value adopted is observed. That incongruence was identified as a producer's mistake. In further investigations those limit values have to be verified in order to provide space for the implementation of the bolt's nut. Finally, the end plate width is given by:

$$b_{ep} = 86 + 2 \times 45 mm = 176 mm \quad (4.26)$$

4.3.5. Check the L-stub bending resistance – sagging moment

4.3.5.1. Initial considerations

A system of three L-stubs was used to attach the lower beam flange to the column flange due to the presence of the beam web or haunch web (Figure 4.5).

The thickness of the L-stub flanges as well as their width, m distances and edge distances, e , were considered equal to the ones adopted for the T-stub flange. Moreover, also the same bolts dimensions and strength were adopted. Regarding the sagging moment, the resistance of the L-stub system should be greater than the one obtained for the friction dampers. Subsequent calculations will prove that this element was not correctly designed and that some yielding should be expected during the experimental tests.

4.3.5.2. Calculation of the resistance of the L-stub

Equations for the calculation of the L-stubs in bending were derived as they are not available in the Eurocode. For this matter, the energy conservation principle is used. A simplified example is presented. For mechanism type-1, it is expected that one hinge is formed at the bolts location in the flange of the L-stub. However, due to the

fact the thickness of the web is 10 mm lower than the thickness of the L-stub flange, for the same force, the second hinge is formed at the web plate. With respect to Figure 4.10, one can derive the resistance for mechanism type-1 through energy considerations.

The internal energy of the system must be equal to the work produced by all forces:

$$\underbrace{M_{pl,w,Rd} \times \theta + M_{pl,f,Rd} \times \theta}_{\text{Internal energy}} = \underbrace{F_{T,1,Rd} \times \delta}_{\text{External work}} \quad (4.27)$$

$$\text{And } \delta = \theta \times m \quad (4.28)$$

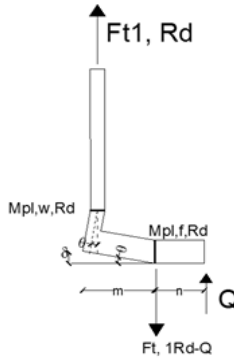
$$\Leftrightarrow F_{T,1,Rd(0)} = \frac{M_{pl,w,Rd} + M_{pl,f,Rd}}{m} \quad (4.29)$$


Figure 4.10: Mechanism Type-1.

in which $M_{pl,w,Rd}$ is the bending resistance of the L-stub web and $M_{pl,f,Rd}$ is the bending resistance of L-stub flange.

It is noted that the EC3 relations are presented for two bolts fastening the plate to the column flange. Therefore, equation (4.29) should have been multiplied by two. However, a more accurate relation provided by EC 3 was adopted:

$$F_{T,1,Rd(0)} = \frac{(4n - e_w) \times M_{pl,w,Rd} + (4n - e_w) \times M_{pl,f,Rd}}{2mn - e_w(m+n)} \quad (4.30)$$

In the above relation, e_w corresponds to a quarter of the diameter of the washer. Additionally, in accordance with the work developed by **Couchaux et al. (2010)**, the interaction between tensile force and bending moment in the tube wall should be considered. Therefore, a reduction factor $g(f_1)$ must be added to the earlier reported equation:

$$F_{T,1,Rd} = F_{T,1,Rd(0)} \times g(f_1) \quad (4.31)$$

in which $g(f_1)$ is given by:

$$g(f_1) = \left[\frac{\sqrt{1-4f_1}-1}{2f_1} \right]; f_1 = \left(\frac{F_{T,1,Rd(0)}}{F_{T,pl,w}} \right)^2 \times \frac{1}{1 + \left(\frac{t_f}{t_w} \right)^2 \cdot \frac{2n_1}{2n_1 - e_w}} \quad (4.32)$$

$F_{T,pl,w}$ is the axial tensile force of the L-stub web:

$$F_{T,pl,w} = l_{eff} \times t_{w,L-stub} \times f_{y,w,L-stub} \quad (4.33)$$

For mechanism type-2, the failure of the bolt with prying force is obtained. The same procedure was adopted.

$$\underbrace{M_{pl,w,Rd} \times \theta + M_{pl,Rd} \times \theta}_{\text{Internal energy}} = \underbrace{F_{T,2,Rd} \times \delta}_{\text{External work}} \quad (4.34)$$

$$M_{pl,Rd} = Q \times n \quad (4.35)$$

$$Q = \sum B_{t,Rd} - F_{T,2,Rd} \quad (4.36)$$

$$\text{And } \delta = \theta \times m \quad (4.37)$$

$$\leftrightarrow F_{T,2,Rd(0)} = \frac{M_{pl,w,Rd} + n \sum B_{t,Rd}}{m+n} \quad (4.38)$$

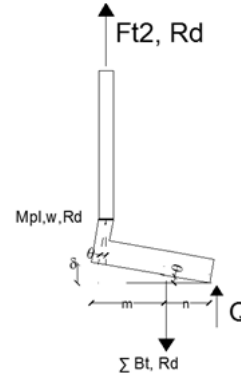


Figure 4.11: Mechanism Type-2.

Again considering the interaction between the tensile force and the bending moment, $F_{T, 2, Rd(0)}$ was reduced by a factor of $g(f_2)$ (Couchaux et al., 2010).

$$F_{T,2,Rd} = F_{T,2,Rd(0)} \times g(f_2) \quad (4.39)$$

in which $g(f_2)$ is given by:

$$g(f_2) = \left[\frac{\sqrt{1-4f_2}-1}{2f_2} \right]; f_2 = \left(\frac{F_{T,2,Rd(0)}}{F_{T,pl,w}} \right)^2 \times \frac{1}{1 + \frac{n_1 B_{t,Rd}}{M_{pl,w,Rd}}} \quad (4.40)$$

Mechanism Type-3 corresponds to the failure of the bolt without any prying action. On the safe side, its resistance can be given as two times the tensile resistance of the bolt, according to EC3. One must say that the referred value already takes in consideration the effect of the bolt bending on the tensile resistance of the bolt.

Besides the earlier mentioned failure mode, in case of L-stubs there is a fourth possible mechanism of rupture: the rupture of the L-stub web. This resistance is given by the tensile resistance of the L-stub web already presented in equation (4.33).

The results obtained for the resistance of each L-stub are presented in Table 4.1. The L-stub located below the beam or haunch flange has eight bolts whereas each L-stub located above the beam or haunch flange has only four bolts. The resistance is given per L-stub. Thus, the total resistance is given by the resistance of the lower L-stub (L-stub 1) plus two times the resistance of the upper L-stubs (L-stub 2).

Table 4.1: Resistance of each L-stub.

L-stub 1		L-stub 2	
m_x (mm)	52.50	m_x (mm)	52.50
$n_{L-stub 1}$ (mm)	45	$n_{L-stub 2}$ (mm)	45
$e_{w, L-stub 1}$ (mm)	10.8	$e_{w, L-stub 2}$ (mm)	10.8
$l_{eff, L-stub 1}$ (mm)	88.0	$l_{eff, L-stub 2}$ (mm)	40.0
$M_{pl, w, Rd/L-stub 1}$ (kN.m)	1.36	$M_{pl, w, Rd/L-stub 2}$ (kN.m)	0.62
$M_{pl, f, Rd/L-stub 1}$ (kN.m)	3.78	$M_{pl, f, Rd/L-stub 2}$ (kN.m)	1.72
$F_{T,1,Rd(0)}$ (kN)	236.84	$F_{T,1,Rd(0)}$ (kN)	107.65
$F_{T1,Rd}$ (kN)	216.55	$F_{T1,Rd}$ (kN)	98.43
$F_{T,2,Rd(0)}$ (kN)	319.02	$F_{T,2,Rd(0)}$ (kN)	158.88
$F_{T2,Rd}$ (kN)	300.67	$F_{T2,Rd}$ (kN)	153.39
$F_{T,3,Rd}$ (kN)	660.96	$F_{T,3,Rd}$ (kN)	330.48
$F_{T,4,Rd}$ (kN)	363.00	$F_{T,4,Rd}$ (kN)	165.00
$F_{T,Rd, L-stub 1}$ (kN)	216.55	$F_{T,Rd, L-stub 2}$ (kN)	98.43

The final resistance obtained for the system of three L-stubs is given by:

$$F_{T,total} = 216.55 + 2 \times 98.43 = 413.42 \text{ kN} \quad (4.41)$$

Comparing the resistance obtained for the L-stub system with the resistance of the friction damper ($F_{damper_CYC12}=512kN$ and $F_{damper_CYC13}=416kN$), the weakest component should be, in fact, the L-stub system, leading to an incorrect design of the joints. However that is not in agreement with the experimental results that, in fact, obtained the weakest component as the friction damper although detecting some yielding of the L-stubs. These results can be related to the fact the real yield strength of steel is usually significantly higher than its nominal value. However, as coupon tests were not performed for the steel parts, this theory cannot be proved. In conclusion, the L-stub component must be correctly designed in order to remain on the safe side and coupon tests need absolutely to be performed in future experiments.

However, even if the resistance of the L-stub in bending is higher than the resistance of the friction damper, yielding should always be expected for this component as 2/3 of its resistance will certainly be lower than the friction damper resistance. The referred value is taken into consideration because usually that level of stresses determines the beginning of yielding for steel components. If that value is bigger than the design resistance, no loss of stiffness is considered for that component. On the contrary, if that value is lower than the design moment, some loss of stiffness should be taken into consideration.

4.3.6. Check the column web in compression

At first, the resistance of the column web in compression was analysed without considering any type of stiffeners, by performing the EC3 procedure. However, as the obtained value was lower than the design force, T_u , continuity plates were adopted and designed to fulfil resistance requirements.

$$F_{c,wc,Rd} = \frac{\omega k_{wc} b_{eff,c,wc} t_{wc} f_{y,wc}}{\gamma_{M0}} = 417.2 \text{ kN} < T_u \quad (4.42)$$

where $b_{eff,c,wc}$ is the effective width of the column web in compression. One should notice that the value of $b_{eff,c,wc}$ differs in the case of the hogging and sagging moments, as described above.

Hogging Moment

$$b_{eff,c,wc} = 2 \times (t_{w,L-stub} + t_{adhes.}) + t_{f(\text{beam or haunch})} + 5(t_{fc} + r_c) + 2t_p \quad (4.43)$$

(expression (4.43) is only applicable in the case $5(t_{fc} + r_c) \geq 2t_{adhes.} + t_{f,beam}$, which always occurs)

Sagging Moment

$$b_{eff,c,wc} = t_{w,T-stub} + 5(t_{fc} + r_c) + 2t_p \quad (4.44)$$

where $t_{w,T-stub}$ is the thickness of the T-stub web, $t_{w,L-stub}$ is the thickness of the L-stub web, t_{adhes} is the thickness of the adhesive plate (or friction plate), t_p is the thickness of the T-stub and L-stub flanges.

4.3.6.1. Design of the continuity plates

The thickness of the continuity plates, t_{cp} , was designed so that the total resistance of the column web plus the continuity plates is sufficient.

$$(b_c - t_{cw} - 2r_c)t_{cp} \cdot f_{y,cp} + F_{c,wc,Rd} \geq T_u \quad (4.45)$$

$$t_{cp} \geq \frac{T_u - F_{c,wc,Rd}}{(b_c - t_{cw} - 2r_c) \cdot f_{y,cp}} \quad (4.46)$$

For both specimens, an approximate thickness of 5 mm was required. Continuity plates with 10 mm of thickness were adopted.

Those elements should be positioned in the centre of compressions or tensions, as presented in Figure 4.12, in order to obtain a better transmission of stresses. Additionally, it is also advised that the thickness of the continuity plates is equal to the thickness of the web elements connected to the column, and that fails to be respected in this connection. Moreover, it is possible to see that, for each connection, three continuity plates were used, and that means one of them is not making any difference. That can be justified by the fact that not only single-sided joint configuration were evaluated, but also unsymmetrical double-sided joint configurations were tested.

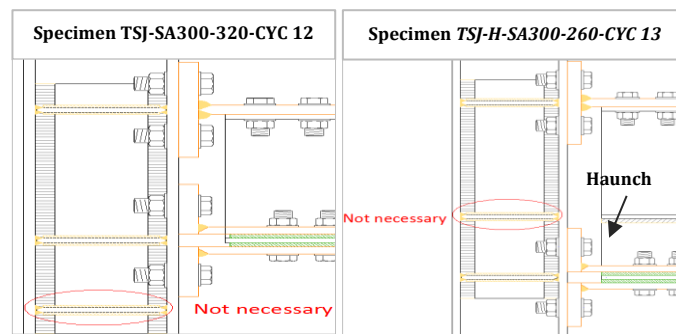


Figure 4.12: Position of the continuity plates.

4.3.6.2. Design of the continuity plates welds

The applied forces in these welds have the same direction as the tension force T_u . Therefore, the following conditions were applied:

$$\tau_{\perp} = \frac{T_u}{4 \times a_{cp} l_{cp}} \text{ and } \tau_{//} = \sigma_{\perp} = 0 \tag{4.47}$$

$$a_{cp} \geq \frac{\sqrt{3} \beta_w \gamma M_2}{4 \cdot f_u l_{cp}} \cdot T_u = 5.55 \text{ mm} \tag{4.48}$$

where $\beta_w=0.85$; $f_u=355$ MPa and l_{cp} is given by $l_{cp} = h_c - 2t_{cf} - 2r_c$ (Figure 4.13).

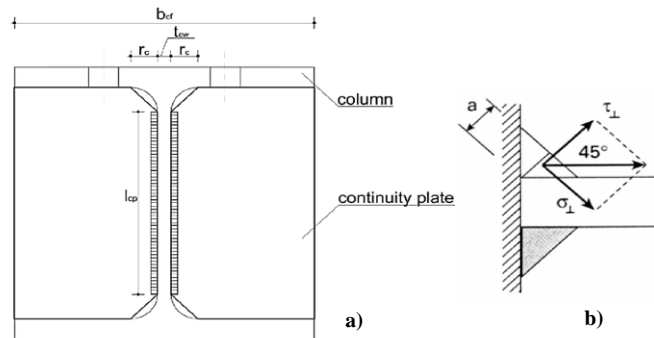


Figure 4.13: Geometry of the continuity plates welds: a) Length of the welds; b) thickness of the welds.

For both specimens, an approximate thickness of 5 mm was required. A thickness, a , equal to 7.07 mm was adopted.

4.3.7. Check of the shear panel resistance

The resistance of the shear panel was verified without additional web plates but it was proved that those elements were needed to support the overstrength required for the analysed component. Knowing the ratio between the squash load applied to the column and its yield resistance f_y , equation (4.50) was considered for the calculation of the web panel resistance.

$$\frac{\sigma}{f_{y,cw}} = 0.3 \quad (4.49)$$

$$V_{wp,Rd} = \frac{(A_{vc} \cdot f_{y,cw})}{\sqrt{3}} \sqrt{1 - \left(\frac{\sigma}{f_{y,cw}}\right)^2} \quad (4.50)$$

The additional resistance due to the existence of the continuity plates was calculated by considering equation (4.51).

$$V_{wp,add,Rd} = \frac{4M_{pl,fc,Rd}}{d_s} \quad (4.51)$$

where d_s is the distance between reinforcement plates and $M_{pl,fc,Rd}$ is the plastic bending resistance of one column flange.

$$\frac{V_{Ed}}{V_{wp,Rd} + V_{wp,add,Rd}} > 1.0 \rightarrow \text{additional web plates} \quad (4.52)$$

After concluding additional web plates were required, their contribution was introduced in $V_{wp,Rd}$ as follows:

$$V_{wp,Rd} = \frac{f_{y,cw} A_{vc} + b_s t_w c f_{y,sp}}{\sqrt{3}} \cdot \sqrt{1 - \left(\frac{\sigma}{f_{y,cw}}\right)^2} \quad (4.53)$$

Where b_s corresponds to the dimension referred in Figure 4.14.

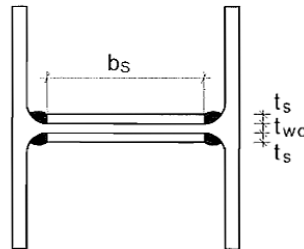


Figure 4.14: Supplementary web plates (adapted from EC3-1-8).

Relation (4.52) was calculated with the additional contribution of the web plates. For connection CYC 12, a value of 1.07 was obtained whereas for connection CYC 13, the given relation is equal to 1.12.

One must see that current rules do not allow an additional resistance bigger than $V_{add} = b_s t_{wc} f_{y,sp}$. However, current investigations about this restriction are being developed due to the fact the limit imposed is too harsh. It is possible to verify that, because of that limit, equation (4.52) is not verified. Thus, because of the too restrictive rules and due to the fact that limit is not significantly exceeded, one considers that the resistance obtained is enough.

4.3.8. Check of the column flange resistance

By adopting the procedure presented in Eurocode 3 for the resistance of the column flange in bending it was proved that this component has an overstrength factor equal to 1.58 and 1.5, in the case of the connection without haunch and with the supplementary haunch, respectively. The existence of stiffeners, although contributing significantly to enhance the resistance of the column web in compression, does not influence the resistance of the column flange in bending.

It is possible to say that no yielding should be expected for this component as its resistance is bigger than 3/2 the resistance of the weakest component, even using the nominal values of resistance for the steel elements.

4.4. Development of moment-rotation curves for the connections

The component method is a general analytical procedure for the prediction of the joint's behaviour. Its application requires the following steps: Identification of the relevant components; evaluation of the behaviour of each component; assembling of the components in order to obtain the structural characteristics of the overall joint by means of strength and stiffness. The assembling of the components is based on a distribution of the internal forces within the joint. In fact, the external loads applied to the joint are distributed, at each loading step, between the individual components according to the instantaneous stiffness and resistance of each component.

The general response of a joint can be presented in the form of an $M-\phi$ curve, where M represents the bending moment to which the joint is subjected and ϕ corresponds to the resultant relative rotation between the connected members. However, one must say that due to the nature of the loading history of the analysed connections, which are subjected to cyclic loads, the assembling of each relevant component becomes much more complex. The development of full hysteretic curves would requests computer implementation. The modified *Richard-Abbot* model is a mathematical powerful tool

for the development of full hysteretic curves, taking into account hardening and pinching parameters (Nogueiro et al., 2006).

Within this framework, only the monotonic behaviour of the joints will be developed, and results will be compared with experimental envelope curves.

In the case of bolted joints, the shape of monotonic moment-rotation curves can be characterized by four parameters: initial stiffness (k_i), design resistance (M_i), strain-hardening stiffness (k_{st}), and ultimate resistance (M_u). In the case of the innovative connections, as the dissipative component is the friction damper, no strain hardening effect is expected. Therefore, this parameter is not considered relevant.

4.4.1. Identification of the relevant components

A small explanation of the behaviour of these connections will take place. The innovative connections are characterized for having a fixed T-stub at the upper level of the beam and a friction damper at the beam lower level which allows slippage due to the existence of slotted holes. At first, no sliding occurs, neither for the friction damper neither for the metallic interface between the T-stub web and the upper beam flange. However, after reaching the sliding resistance of the upper interface and without having slotted holes, three components must be added to the resistance of the connection: the bolts in shear, the T-stub web in bearing and the beam flange in bearing. Those components will provoke a decrease of the initial stiffness. In the following procedure, the initial stiffness is calculated and after reaching the sliding resistance of the steel on steel interface, a modified value is obtained.

The relevant components analysed are presented in Table 4.2 and Figure 4.15.

Table 4.2: Relevant components for the DST connection.

Innovative Double Split Connection	
Hogging Moment	Sagging Moment
<i>Bolts in tension (bt)</i>	<i>Bolts in tension (bt)</i>
<i>T-stub flange in bending (tsb)</i>	<i>L-stub flange in bending (lsb)</i>
<i>Column Flange in Bending (cfb)</i>	<i>Column Flange in Bending (cfb)</i>
<i>Column web in tension (cwt)</i>	<i>Column web in tension (cwt)</i>
<i>T-stub web in tension (tsw-t)</i>	<i>L-stub web in tension (lsw-t)</i>
<i>Column Panel in shear (cps)</i>	<i>Column Panel in shear (cps)</i>
<i>Column web in compression (cwc)</i>	<i>Column web in compression (cwc)</i>
<i>After 1st slippage (add 3 components)</i>	
<i>Bolts in shear (bs)</i>	
<i>T-stub web in bearing (tsw-b)</i>	
<i>Beam flange in bearing (bf-b)</i>	

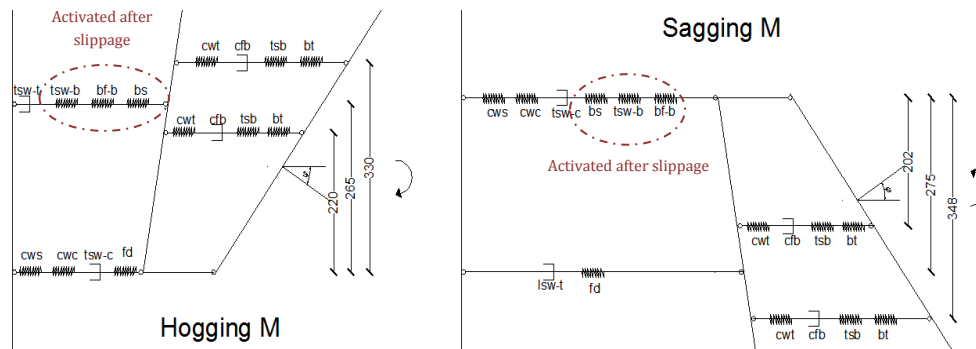


Figure 4.15: Identification of the main components – Specimen TSJ-SA300-320-CYC 12.

The main differences between the two connections are the lever arms which increase significantly in the case of connection CYC 13. In Table 4.3 is possible to observe the correspondent lever arms for both connections.

Table 4.3: Values of the lever arms for both connections (mm).

	TSJ-SA300-320-CYC 12		TSJ-H-SA300-260-CYC 13	
	Hogging	Sagging	Hogging	Sagging
1 st row	330	348	477	494
2 nd row	265	275	412	422
3 rd row	220	202	367	348

It is important to refer that four components of the connection are not aligned with the overall components belonging to the tension zone in the case of the hogging moment, more specifically, the T-stub web in tension, the bolts of the T-stub web in shear, the T-stub web in bearing and the beam flange in bearing. Therefore, an additional line was considered for these 4 components and should be assembled as in series with the other components belonging to the two bolt rows. The lever arms of the four referred components were considered to be sufficiently close to consider them aligned in the same row. Identically, for the sagging moment, two components in the tension zone were positioned in an independent line. These two components are the friction damper and the I-stub webs in tension. The later observations are depicted in Figure 4.15. Attention should be paid to the adopted order of the rows. That order will be considered in the subsequent calculations.

Additionally, in the following procedure, the hogging and sagging moments are analysed separately due to asymmetries of the joints.

Furthermore, the connections herein analysed are mainly influenced by the cyclic response of the friction dampers, which have very stable hysteretic loops. However, for the steel components, the possibility of a small engagement in the plastic field is

analysed. For this matter, 2/3 of the resistance of each component will be compared with the design resistance of the connection.

4.4.2. Initial stiffness, $K_{i,hogg}$ - hogging moment

The individual stiffness of each component was obtained and assembled to obtain the total stiffness of the connection.

The stiffness of the components belonging to the tension zone is presented in Table 4.4.

Table 4.4: Component's stiffness in the tension zone- before slippage.

Before slippage between the t-stub web and the upper beam flange	Relevant Components	Coefficients: EC3-1-8	k_i (mm)		
			1 st row	2 nd row	3 rd row
	<i>Bolts in tension (bt)</i>	k_{10}	10.85	-	10.85
	<i>T-stub in bending (tsb)</i>	k_5	13.58	-	13.58
	<i>Column Flange in Bending (cfb)</i>	k_4	32.86	-	32.86
	<i>Column web in tension (cwt)</i>	k_3	9.97	-	9.97
	<i>T-stub web in tension (tsw-t)</i>	k_9	-	44.00	-
	<i>bolts in shear (bs)</i>	k_{11}	-	∞	-
	<i>T-stub web in bearing (tsw-b)</i>	k_{12}	-	∞	-
	<i>beam flange in bearing (bf-b)</i>	k_{12}	-	∞	-
		k_{eff} (mm)	3.37	44.00	3.37

After calculating the effective stiffness assigned to each row and knowing the lever arm associated to the three identified rows, the equivalent lever arm, Z_{eq} , and the equivalent stiffness, k_{eq} can be determined. In this case, as the lever arm of the connection with the haunch is bigger, the calculated values are also different.

TSJ-SA300-320-CYC 12

$$Z_{eq,HOGG} = \frac{k_{eff,r1}h_{r1}^2 + k_{eff,r3}h_{r3}^2}{k_{eff,r1}h_{r1} + k_{eff,r3}h_{r3}} = 286.0 \text{ mm} \quad (4.54)$$

$$k_{eq,HOGG} = \frac{1}{\frac{Z_{eq}}{k_{eff,r1}h_{r1} + k_{eff,r3}h_{r3}} + \frac{h_{r,r2}}{k_{eff,r2}Z_{eq}}} = 5.71 \text{ mm} \quad (4.55)$$

TSJ-H-SA300-260-CYC 13

$$Z_{eq,HOGG} = \frac{k_{eff,r1}h_{r1}^2 + k_{eff,r3}h_{r3}^2}{k_{eff,r1}h_{r1} + k_{eff,r3}h_{r3}} = 429.2 \text{ mm} \quad (4.56)$$

$$k_{eq,HOGG} = \frac{1}{\frac{Z_{eq}}{k_{eff,r1}h_{r1} + k_{eff,r3}h_{r3}} + \frac{h_{r,r2}}{k_{eff,r2}Z_{eq}}} = 5.80 \text{ mm} \quad (4.57)$$

The stiffness of the remaining components is presented in Table 4.5 as well as the value of the initial stiffness of the connection for the hogging moment.

Table 4.5: Stiffness of the components in the shear and compressive zones and initial stiffness, $S_{j, ini}$.

Relevant Components	Coefficients: EC3-1-8	k_i (mm)	$S_{j, ini}$ (kN.m)	
			TSJ-SA300-320-CYC 12	TSJ-H-SA300-260-CYC 13
Column web in shear (cws)	k_1	∞	87153.7	198981.4
Column web in compression (cwc)	k_2	∞		
L-stub web in compression (lsw-c)	k_9	45.82		

4.4.3. Modified stiffness, $K_{mod, HOGG}$ - hogging moment

The shear resistance of the steel interface with normal sized bolts is given by EC3:

$$F_{s, Rd} = k_s \cdot n \cdot m \cdot \mu \cdot F_{p, c} \quad (4.58)$$

To continue using the adopted terminology, n represents the number of bolts ($n=8$) and m the number of friction interfaces ($m=1$). Furthermore, k_s is considered equal to the unit as the analysed bolts have normalised holes. The static friction coefficient used for steel on steel interface is equal to $\mu=0.170$, considering the classical *Bowden and Tabor theory*, already explained. The calculation of the preload force is made by assuming the following equation:

$$F_{p, c} = 0.7 \cdot f_{ub} \cdot A_s = 0.7 \times 800 \times 245 \times 10^{-3} = 137.2 \text{ kN} \quad (4.59)$$

Therefore, after achieving a resistance equal to $F_{s, Rd} = 1 \times 8 \times 0.170 \times 137.2 = 186.6 \text{ kN}$, the stiffness decreases.

The stiffness of the new activated components belonging to the tension zone is presented in Table 4.6. Its influence can be rapidly noticed in the effective stiffness of the second row. Due to the fact that row is in series with the others, one can expect a significant decrease of stiffness.

Table 4.6: Component's stiffness in the tension zone- After slippage.

Relevant Components	Coefficients: EC3-1-8	k_i (mm)		
		1 st row	2 nd row	3 rd row
bolts in shear (bs)	k_{11}	-	6.10	-
T-stub web in bearing (tsw-b)	k_{12}	-	9.21	-
beam flange in bearing (bf-b)	k_{12}	-	3.99	-
	k_{eff} (mm)	3.37	1.83	3.37

The obtained values for the equivalent lever arm and stiffness are presented as follows:

TSJ-SA300-320-CYC 12

$$Z_{eq,HOGG} = \frac{k_{eff,r1}h_{r1}^2 + k_{eff,r3}h_{r3}^2}{k_{eff,r1}h_{r1} + k_{eff,r3}h_{r3}} = 286.0 \text{ mm} \quad (4.60)$$

$$k_{eq,HOGG} = \frac{1}{\frac{Z_{eq}}{k_{eff,r1}h_{r1} + k_{eff,r3}h_{r3}} + \frac{h_{r,r2}}{k_{eff,r2}Z_{eq}}} = 1.52 \text{ mm} \quad (4.61)$$

TSJ-H-SA300-260-CYC 13

$$Z_{eq,HOGG} = \frac{k_{eff,r1}h_{r1}^2 + k_{eff,r3}h_{r3}^2}{k_{eff,r1}h_{r1} + k_{eff,r3}h_{r3}} = 429.2 \text{ mm} \quad (4.62)$$

$$k_{eq,HOGG} = \frac{1}{\frac{Z_{eq}}{k_{eff,r1}h_{r1} + k_{eff,r3}h_{r3}} + \frac{h_{r,r2}}{k_{eff,r2}Z_{eq}}} = 1.49 \text{ mm} \quad (4.63)$$

Table 4.7: Stiffness of the components in the shear and compressive zone and modified stiffness, $S_{j, mod}$.

Relevant Components	Coefficients : EC3-1-8	k_i (mm)	$S_{j, mod}$ (kN.m)	
			TSJ-SA300-320-CYC 12	TSJ-H-SA300-260-CYC 13
Column web in shear (cws)	k_1	∞		
Column web in compression (cwc)	k_2	∞	25200.0	55638.1
L-stub web in compression (lsw-c)	k_9	45.82		

Due to the fact the displacement allied to the mechanism of slip in the upper friction interface is so small, it was not taken into consideration.

$$\delta_{interface} = \frac{d_0 - d}{2} = 0.5 \text{ mm} \rightarrow \text{Neglected}$$

4.4.4. Design moment resistance, $M_{v, HOGG}$ - hogging moment

Regarding the hogging moment, all components were designed in order to have the weakest component as the friction damper. The steel component to which corresponds the weakest resistance is the T-stub in bending and still 2/3 of its resistance is still bigger than the design resistance, reason why the yielding of this component should not be considered.

As it was studied on experiments realized by Salerno University on the friction dampers, the generated force in the interface sprayed aluminium on steel varies with the normal force applied and also with the cumulated value of the energy dissipated.

At first, the static friction coefficient is calculated based on the applied preload for both specimens. For that, a relation derived by Salerno is considered (in **Latour et al., 2014**):

$$\mu = -0.0109 p + 0.6537 \{p [MPa]\} \quad (4.64)$$

Where p represents the applied pressure on the interface, obtained by assuming the normal force spreads from the bolt head through the plate thickness with a gradient equal to 45° .

TSJ-SA300-320-CYC 12

$$p = \frac{4N_b}{\pi(2t_p+d_{bh})^2} = \frac{4 \times 80}{\pi(2 \times 15 + 1.7 \times 20)^2} = 24.87 \text{ MPa} \quad (4.65)$$

$$\mu = -0.0109 \times 24.87 + 0.6537 = 0.383 \quad (4.66)$$

TSJ-H-SA300-260-CYC 13

$$p = \frac{4N_b}{\pi(2t_p+d_{bh})^2} = \frac{4 \times 65}{\pi(2 \times 15 + 1.7 \times 20)^2} = 20.21 \text{ MPa} \quad (4.67)$$

$$\mu = -0.0109 \times 24.87 + 0.6537 = 0.433 \quad (4.68)$$

Finally, a more accurate value for the friction dampers resistance is calculated in comparison with the values obtained in the design procedure and also the design moment of the connection is calculated regarding the weakest component.

TSJ-SA300-320-CYC 12

$$F = T_u = C_u = \frac{T_b \times m \times n \times \mu}{0.2 \times d} = \frac{320 \times 2 \times 8 \times 0.383}{0.2 \times 20} = 489.8 \text{ kN} \quad (4.69)$$

$$M_{j_c, Rd} = 489.8 \times 265 \times 10^{-3} = 129.8 \text{ kN.m} \quad (4.70)$$

TSJ-H-SA300-260-CYC 13

$$F = T_u = C_u = \frac{T_b \times m \times n \times \mu}{0.2 \times d} = \frac{260 \times 2 \times 8 \times 0.433}{0.2 \times 20} = 450.8 \text{ kN} \quad (4.71)$$

$$M_{j_c, Rd} = 450.8 \times 411 \times 10^{-3} = 185.3 \text{ kN.m} \quad (4.72)$$

4.4.5. Ultimate moment resistance, $M_{u, HOGG}$ – hogging moment

The ultimate resistance calculated, in this case, does not correspond to the ultimate resistance of the connection but is determined considering the load history applied. This means that the connection was not subjected to failure and there are mechanisms that were not yet achieved like the bearing of the plates and the shearing of the bolts on the lower level of the beam. These mechanisms should be considered in robustness studies.

A small variation of the friction coefficient can also be determined as its value depends on the cumulated energy dissipated. Attending to the load history applied, the biggest rotation corresponds to the ultimate cycle due to the fact AISC (2010) procedure was adopted. Therefore, using the total energy dissipated in the experiments performed in Salerno, a lower friction force should be adopted. Again a relation derived by Salerno and presented in **Latour et al., 2014** is used:

$$\frac{\mu_i}{\mu_k} = 1 - 0.000329 E_{diss,tot} \text{ with } E_{diss,tot} (kN.m) \quad (4.73)$$

TSJ-SA300-320-CYC 12

$$\Leftrightarrow \mu_i = (1 - 0.000329 \times 159.297) \times 0.382 = 0.36 \quad (4.74)$$

$$F = T_u = C_u = \frac{T_b \times m \times n \times \mu \times k_s}{0.2 \times d} = \frac{320 \times 2 \times 8 \times 0.36}{0.2 \times 20} = 464.2 \text{ kN} \quad (4.75)$$

$$M_u = 464.2 \times 265 \times 10^{-3} = 109.6 \text{ kN.m} \quad (4.76)$$

TSJ-H-SA300-260-CYC 13

$$\Leftrightarrow \mu_i = (1 - 0.000329 \times 216.45) \times 0.433 = 0.40 \quad (4.77)$$

$$F = T_u = C_u = \frac{T_b \times m \times n \times \mu}{0.2 \times d} = \frac{260 \times 2 \times 8 \times 0.40}{0.2 \times 20} = 418.8 \text{ kN} \quad (4.78)$$

$$M_u = 418.8 \times 411 \times 10^{-3} = 172.1 \text{ kN.m} \quad (4.79)$$

4.4.6. Initial stiffness, $K_{i,SAGG}$ - sagging moment

In this case, the additional components activated after slippage are located on the compressive side of the connection.

The stiffness of the components belonging to the tension zone is presented in Table 4.8.

Table 4.8: Component's stiffness in the tension zone- before slippage.

Relevant Components	Coefficients: EC3-1-8	k_i (mm)		
		1 st row	2 nd row	3 rd row
<i>Bolts in tension (bt)</i>	k_{10}	10.85	-	10.85
<i>L-stub in bending (lsb)</i>	k_5	8.55	-	7.77
<i>Column Flange in Bending (cfb)</i>	k_4	32.86	-	32.86
<i>Column web in tension (cwt)</i>	k_3	9.97	-	9.97
<i>L-stub web in tension (lsw-t)</i>	k_9	-	45.82	-
	$k_{eff}(mm)$	2.94	45.82	2.84

The equivalent lever arm and stiffness are presented below.

TSJ-SA300-320-CYC 12

$$Z_{eq,SAGG} = \frac{k_{eff,r1} h_{r1}^2 + k_{eff,r3} h_{r3}^2}{k_{eff,r1} h_{r1} + k_{eff,r3} h_{r3}} = 295.5 \text{ mm} \quad (4.80)$$

$$k_{eq,SAGG} = \frac{1}{\frac{Z_{eq}}{k_{eff,r1}h_{r1}+k_{eff,r3}h_{r3}} + \frac{h_{r,r2}}{k_{eff,r2}Z_{eq}}} = 4.87 \text{ mm} \quad (4.81)$$

TSJ-H-SA300-260-CYC 13

$$Z_{eq,HOGG} = \frac{k_{eff,r1}h_{r1}^2+k_{eff,r3}h_{r3}^2}{k_{eff,r1}h_{r1}+k_{eff,r3}h_{r3}} = 434.9 \text{ mm} \quad (4.82)$$

$$k_{eq,HOGG} = \frac{1}{\frac{Z_{eq}}{k_{eff,r1}h_{r1}+k_{eff,r3}h_{r3}} + \frac{h_{r,r2}}{k_{eff,r2}Z_{eq}}} = 5.02 \text{ mm} \quad (4.83)$$

The stiffness of the remaining components is presented in Table 4.9 as well as the value of the initial stiffness of the connection for the sagging moment.

Table 4.9: Stiffness of the components in the shear and compressive zone and initial stiffness, $S_{j, ini}$.

Relevant Components	Coefficients: EC3-1-8	k_i (mm)	$S_{j, ini}$ (kN.m)	
			TSJ-SA300-320- CYC 12	TSJ-H-SA300-260- CYC 13
Column web in shear (cws)	k_1	∞	80473.6	178981.0
Column web in compression (cwc)	k_2	∞		
T-stub web in compression (tsw-c)	k_9	44.00		
T-stub web in bearing (tsw-b)	k_{12}	∞		
beam flange in bearing (bf-b)	k_{12}	∞		
bolt in shear (bs)	k_{11}	∞		

4.4.7. Modified stiffness, $K_{mod,SAGG}$ - sagging moment

The sliding resistance already calculated for the hogging moment maintain its value of 186.6 kN.

As already explained, the stiffness of the components belonging to the tension zone is equal to the one presented for the initial stiffness as well as the obtained values of the equivalent stiffness and lever arm. However, the equivalent stiffness on the compressive side is modified due to the new activated components.

Table 4.10: Stiffness of the components in the shear and compressive zone and modified stiffness, $S_{j, mod}$.

Relevant Components	Coefficients: EC3-1-8	k_i (mm)	$S_{j, mod}$ (kN.m)	
			TSJ-SA300-320-CYC 12	TSJ-H-SA300-260-CYC 13
Column web in shear (cws)	k_1	∞	24425.8	53316.0
Column web in compression (cwc)	k_2	∞		
T-stub web in compression (tsw-c)	k_9	44.00		
T-stub web in bearing (tsw-b)	k_{12}	9.21		
Beam flange in bearing (bf-b)	k_{12}	3.99		
Bolts in shear (bs)	k_{11}	6.10		

The displacement allied to the mechanism of slip in the upper friction interface is neglected as it was also considered for the hogging moment.

4.4.8. Design moment resistance, $M_{v, SAGG}$ - sagging moment

Experimental curves prove that the design resistance obtained is equal to the friction dampers resistance. In order to achieve these results, the yield strength of steel was enhanced until the resistance of the connection is given by the resistance of the friction dampers, 489.8 kN and 450.8 kN, for connection CYC 12 and CYC 13, respectively.

For the connection without the haunch, the necessary yielding resistance must at least arise up to 326 MPa, whereas for the specimen CYC 13, f_y has to achieve 288 MPa. By observing the resistance values required for steel, it is perfectly possible to have such variability of the yield strength.

Calculations will not be repeated and therefore the design resistance of the connection has the same values as for the hogging moment, defined by the weakest component, the friction damper.

4.4.9. Ultimate moment resistance, $M_{u, SAGG}$ – sagging moment

The value adopted for the friction coefficient of each connection is the same as the one calculated for the hogging moment as well as the ultimate resistance obtained.

4.4.10. Final $M-\phi$ monotonic curve

A comparison between the analytical and experimental results is presented below (analytical curve with dashed blue line). The three points that describe the analytical curve are depicted in Table 4.11. The first point (A) was obtained considering the initial stiffness and the slip resistance regarding the upper beam flange and the T-stub web interface. The second point (B) was obtained considering the modified stiffness and the design resistance of the connection controlled by the friction dampers. The third point (C) is reached by considering the softening behaviour that influences the kinetic friction coefficient.

Table 4.11: Points used for the final monotonic curve.

HOGGING MOMENT					
TSJ-SA300-320-CYC 12			TSJ-H-SA300-260-CYC 13		
Data Points	ϕ (rad)	M (kN.m)	Data Points	ϕ (rad)	M (kN.m)
A	5.67E-04	49	A	3.85E-04	77
B	3.76E-03	130	B	2.34E-03	185
C	6.00E-02	123	C	6.00E-02	172
SAGGING MOMENT					
TSJ-SA300-320-CYC 12			TSJ-H-SA300-260-CYC 13		
Data Points	ϕ (rad)	M (kN.m)	Data Points	ϕ (rad)	M (kN.m)
A	-6.14E-04	-49	A	-4.28E-04	-77
B	-3.90E-03	-130	B	-2.47E-03	-185
C	-5.00E-02	-123	C	-6.00E-02	-172

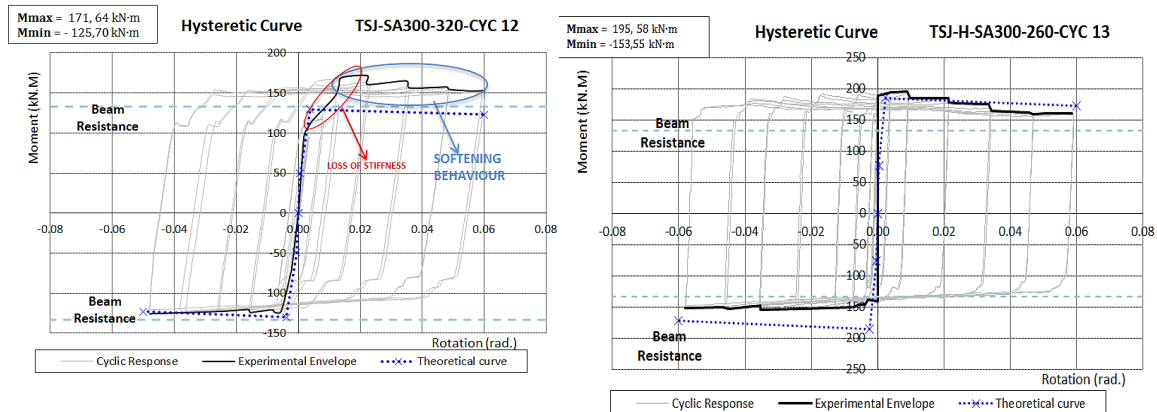


Figure 4.16: Comparison between the analytical model and the experimental envelope curve - TSJ-SA300-320-CYC 12 and TSJ-H-SA300-260-CYC 13.

Specimen TSJ-SA300-320-CYC 12

There is a good agreement with the experimental results for connection CYC 12. However, it is difficult to understand the loss of stiffness occurring for the hogging moment. Perhaps, due to the fact this type of connection is not currently used and its behaviour is not well known, there is the possibility of appearing new components that are not yet explored in the EC3-1-8.

For example, the component of the L-stub stem in bending could be activated not only for the sagging moment but also for the hogging moment because rotation of the joint is expected either way. Therefore, the yielding observed in the experimental curve could be related to this new component activated for the hogging moment, which is, in fact, in agreement with the experimental report presented by Salerno. After calculating $2/3$ of the modified resistance of the L-stub, which takes into account the random material variability of steel ($f_y = 326$ MPa), a value of approximately 90 kN.m is obtained, significantly close to the value corresponding to the loss of stiffness.

Additionally, it is also possible to observe that the sliding resistance of the friction damper is higher than expected for the hogging moment. This may be related to the fact that the friction damper does not behave identically when subjected to compressive forces or tension forces. It appears that resistance to slipping is greater when the friction interfaces are subjected to compressive forces. In fact, the direction of the force may influence the preloading of the bolts, which directly influences the sliding resistance. The ideal situation would be to measure the prestressing applied. This will be evaluated further on in the project “FREEDAM”.

However, although the slip resistance is greater for the hogging moment, the stability of the cycles decreases, which means a more significant softening behaviour is obtained.

Specimen TSJ-H-SA300-260-CYC 13

For the specimen with the additional haunch, correlations obtained by the component method were not on the safe side for the sagging moment. In this case, a resistance of approximately 150 kN.m was obtained, which is significantly different from the friction damper resistance of 185 kN.m.

However, some of the conclusions reached for connection CYC 12 are also valid for this joint. Identically, the resistance for the hogging moment is greater than the resistance for the sagging one, which reinforces the conclusion that the friction device behaves differently depending on the type of axial force. Additionally, the stability of the cycles also increases significantly for the sagging moment.

4.4.11. Final statement

The only possible way to fully understand these results is through numerical modelling of the overall beam-to-column connection in order to identify all the components involved in the behaviour of the joint, more specifically, to analyse if the bending of the L-stub web is relevant to the loss of stiffness obtained for the hogging moment. Additionally, it would also be helpful to identify the differences in the behaviour of the friction damper when subjected to tensile or compressive forces.

5. NUMERICAL SIMULATION OF THE INNOVATIVE JOINT

5.1. Introduction

In this chapter, the main goal is to develop a numerical model for the **TSJ-SA300-320-CYC-12** connection and compare the results with the experimental ones. As already explained in the previous chapter, there are some phenomena that are difficult to explain by using mechanical models, because they are not prepared to deal with load reversal required in cyclic analysis, and due to the new components involved.

5.2. Finite element model development

Aiming to decrease the running time of the numerical model, different alternatives were analysed. Some of them are presented in Figure 5.1.

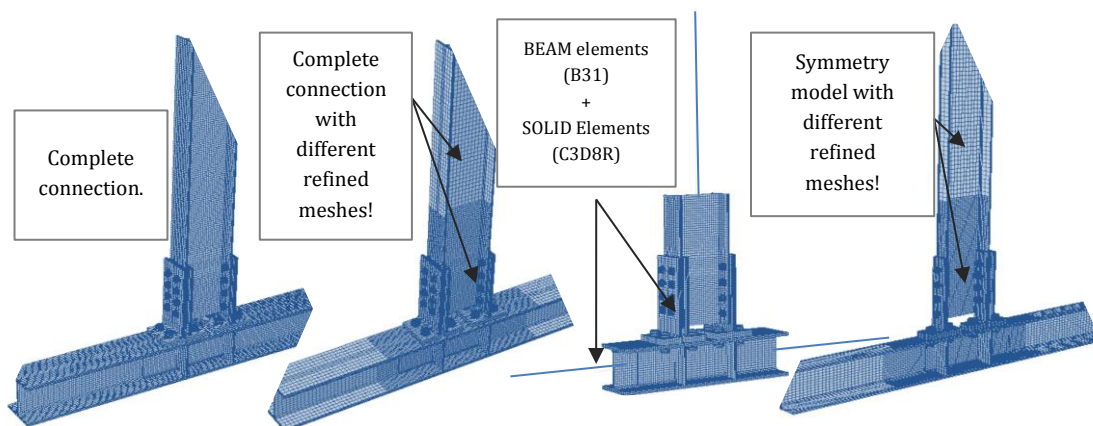


Figure 5.1: Analysed Finite Element Models.

After studying all these possibilities, it was concluded that using symmetry conditions and adopting a less refined mesh in the areas positioned at a sufficient distance from the nodal zone would save significant computational effort while giving accurate results.

5.2.1. Description of the numerical model

The innovative connection studied in the present work is characterized by having a significant number of steel elements (see Figure 5.2). Therefore, difficulties in modelling such type of connections may result from contact convergence problems.

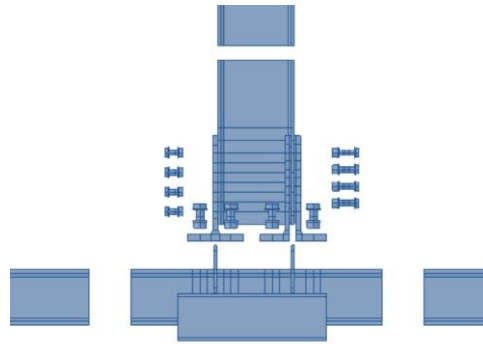


Figure 5.2: Elements in the connection zone.

In contrast, as all steel parts of this connection should behave elastically, material nonlinearity, buckling, pinching effects and low cycle fatigue are not of main concern, unlikely to what is observed for more standard bolted joints.

In the following subsections, the numerical model developed is explained in detail.

5.2.1.1. *Material properties*

In the presented connection, all metallic elements are made of steel S275. However, the friction material consists in a 8 mm plate of steel sprayed with a thin layer of aluminium (300 μm). Additionally, two types of bolts were used. In order to attach all the steel elements to the beam flanges, M20 bolts were used, while the column flange was tightened to the angles by means of M27 bolts, both made of class 8.8. Furthermore, all bolt and nut dimensions were defined according to **EN 14399-3 (2005)** and all washer dimensions according com **EN 14399-5 (2005)**.

As no coupon tests were tested for the steel elements used in the experimental specimen **TSJ-SA300-320-CYC-12**, it is not possible to develop true stress-strain curves that reproduce the mechanical behaviour of the materials. Since all elements of these connections should behave elastically, the material's plastic range characterization is not of main interest. However, as already discussed, some yielding was observed in the tested specimen, more specifically in the L-stub components, meaning that these elements were not correctly designed. In fact, as already presented in the previous chapter, the way those elements were designed should have led to an earlier rupture of the connection, and the weakest component of the connection should have been the system of L-stubs. Because this was not observed in the experimental tests, the only justification was the strength variability of steel. Therefore, in line with available data in the literature (**Luis Simões da Silva et al.,2009**), the yield strength of steel was enhanced so that the weakest component is the friction damper. The adopted yield strength for the steel elements in this joint is $f_y = 326 \text{ MPa}$.

The steel plate’s behaviour introduced in the numerical model is characterized by a quadri-linear law. The bolts are modelled based on a tri-linear law. Both curves, the quadri-linear law and the tri-linear law, are depicted below, while the resistance values adopted for this connection are presented in Table 5.1.

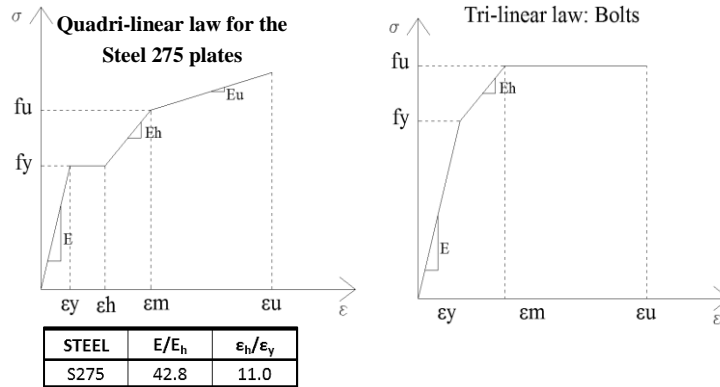


Figure 5.3: Stress-strain curves for the steel plates and the bolts.

Table 5.1: Material properties for the steel plates and bolts.

Steel S275 Plates			Steel bolts M20-8.8		
Elastic range - Abaqus			Elastic range - Abaqus		
<i>E(GPa)</i>	210		<i>E(GPa)</i>	210	
<i>ν</i>	0.3		<i>ν</i>	0.3	
Plastic range - Abaqus			Plastic range - Abaqus		
<i>σ (MPa)</i>	<i>ε (%)</i>	<i>ε</i>	<i>σ (MPa)</i>	<i>ε (%)</i>	<i>ε</i>
326	0.000	0.000	640	0.000	0.000
326	1.552	0.016	800	0.762	0.008
509.7	5.297	0.053	1000	8.695	0.087
746.9	55.845	0.558	<i>ρ (kg/m³)</i>		7850
<i>ρ (kg/m³)</i>		7850			

The friction material behaviour was simulated only at the interaction properties module, more specifically, in the tangential contact definition.

5.2.1.2. Steps used in the numerical model

Two steps (stages) are considered for the analysis of the connection. The first one is used for the application of gravity loads and for the application of the preloading forces in the bolts. In the second step, the displacement history applied at the beam end is introduced.

Gravity Loads and Preloading forces

Gravity loads were introduced automatically in the model. As for the bolt loads, they were introduced considering the “adjust length” option, available in Abaqus.

Considering the torques applied to the bolts in the experimental procedure, the calculation of the adjust lengths of each bolt is presented in Table 5.2.

Table 5.2: Calculation of the elastic adjust length of the bolts.

Preloaded bolts:M20 lower beam flange- n = 8				
T_b (N.m)	N_b (KN)	σ (MPa)	$\Delta L_{Elastic}$ (mm)	% P_{bolt}
320.0	80.0	254.65	0.068	41%
Preloaded bolts:M20 upper beam flange - n = 8				
T_b (N.m)	N_b (KN)	σ (MPa)	$\Delta L_{Elastic}$ (mm)	% P_{bolt}
548.8	137.2	436.72	0.063	70%
Preloaded bolts:M27 - n = 8				
T_b (N.m)	N_b (KN)	σ (MPa)	$\Delta L_{Elastic}$ (mm)	% P_{bolt}
800.0	148.15	258.75	0.049	40%

However, as studied before in the numerical simulation of the friction component, this “adjust length” gives origin to deformations of the connected elements. Therefore, in order to consider those deformations, the “adjust length” has to be calibrated in order to provide the correct torque introduced in the experimental procedure. To take into consideration the elastic deformation of all elements attached, three length adjustments are considered for each bolt: M20 bolt localized at the upper beam flange, M20 bolt located at the lower beam flange and M27 bolts connected to the column flange. Then, the pressure introduced in each bolt is taken from the numerical results. Furthermore, as all elements remain in the elastic range, those three points Pressure- ΔL_{bolt} give origin to approximate linear regressions, for each bolt.

The regression equations obtained for each bolt are:

- Upper beam flange - M20 bolts: $Pressure = 3266.6\Delta_{L,Bolt} - 6.7517$;
- Lower beam flange - M20 bolts: $Pressure = 2108.5\Delta_{L,Bolt} - 6.7751$;
- M27 bolts: $Pressure = 2658.8\Delta_{L,Bolt} + 1.0539$;

The final “adjust lengths” of the bolts are calculated by using the later expressions.

Table 5.3: Final adjust length of the bolts and % of error.

	M20_lower	M20_upper	M27
Target Pressure	254.65	436.72	258.75
ΔL_{bolt} (mm)	0.1240	0.1367	0.0969
Pressure	254.58	437.6	258.71
Error (%)	0.03%	0.20%	0.02%

Displacement amplitude

Firstly, only the monotonic behaviour of the joint is analysed. To do that, a transverse displacement equal to 93.6 mm is applied at the end of the beam. The main goal here was to analyse the connection's behaviour when subjected to hogging or sagging moments and point out the most important differences between both.

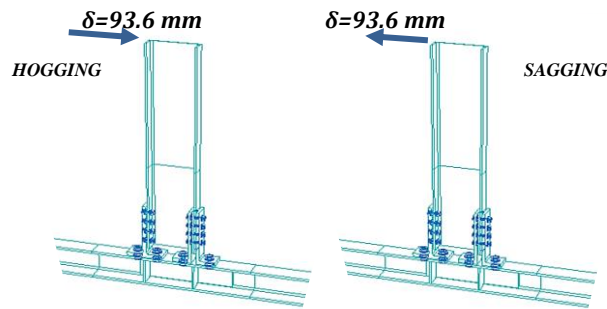


Figure 5.4: Connections subjected to monotonic loading conditions.

Subsequently, to evaluate the response of the joint when subjected to cyclic loading conditions, an amplitude function is used. The amplitude and number of cycles were defined according to AISC (2010) code for cyclic tests on beam-to-column joints. The standard loading history applied to the connection, in terms of interstory drift angle, is presented in Figure 5.5. Those values were converted into displacements at the beam end by simply multiplying the drift angles by the beam length equal to 1560 mm.

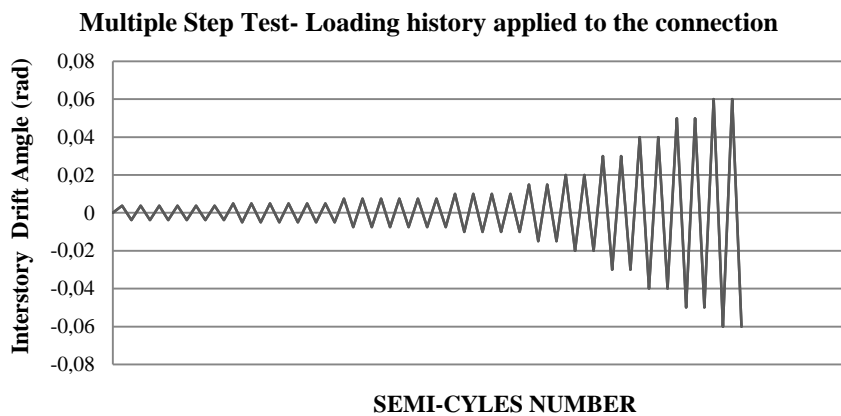


Figure 5.5: AISC loading protocol.

For each cycle, 4 amplitude points are introduced in the numerical model: $(T_i; a_i)$, $(T_{i+1}; 0)$, $(T_{i+2}; -a_i)$, $(T_{i+3}; 0)$. Therefore, by introducing 34 cycles related to the AISC loading protocol, the displacement step has a total time period equal to $T=34 \times 4=136$.

5.2.1.3. Type of finite elements

Continuum solid elements, more specifically 8 noded linear brick elements, were adopted. An approach using reduced integration elements (C3D8R) led to the necessity of using hourglass control in order to reduce the severe deformation of individual finite elements.

As already explained, the mesh was specially refined in the nodal zone and less refined for the beam and column elements located at a predefined distance from the nodal zone as reported in Figure 5.6.

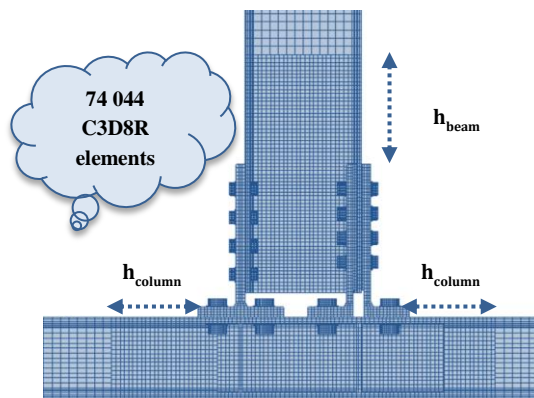


Figure 5.6: Refinement of the mesh.

A total of 74,044 finite elements are used in the numerical model, in which 65,224 elements are located at the nodal zone.

5.2.1.4. Interaction properties

Two types of interaction properties are considered in this analysis, allowing to define the influence of the sprayed aluminium coater. In fact, the normal resistance is given by the steel plate covered with aluminium. Thus, the presence of the layer of aluminium is only reported in terms of shear resistance of the asperities. These may be introduced in the numerical model by defining a friction coefficient used for all interactions where the sprayed aluminium plate participates.

In Table 5.4 there is a full description of the contact properties used for steel-steel and for sprayed aluminium-steel interactions.

Table 5.4: Interaction properties definition.

Interaction Properties		
	Normal behaviour	Tangential behaviour
Steel-steel	"Hard Contact"	Penalty: $\mu = 0.173$
Sprayed aluminium-steel	"Hard Contact"	Penalty: $\mu = 0.38$

5.2.1.5. *Boundary conditions*

Four different boundary conditions are introduced in the numerical model. One for the symmetry condition, one to fix both column edges and one to restrain the beam. As already explained in the initial chapters of this dissertation, the columns are fixed by two extremity hinges and an actuator is used to apply, under force control, an axial load equal to 30% of the column's squash load. Additionally, the displacement history is applied at the beam end by using a second actuator and lateral displacements are restrained by a horizontal frame.

The compressive load on the column is applied in the numerical model by varying the length of the column. Considering Hooke's law and knowing the value of the squash load, one can calculate the required variation of the column length:

$$\Delta_L = L_{column} \times 0.3 \times \frac{f_{y,column}}{E} = 2000 \times 0.3 \times \frac{275}{210 \times 10^3} = 0.7857 \text{ mm} \quad (5.1)$$

Then, the presented value is divided by two and applied at both column edges.

5.2.1.6. *Scripting interface*

The above numerical model was written by using the scripting interface and python language. This way, parametric studies can be later conducted by changing the geometry of all members included, beam sizes, bolts types, number of bolts. The script produced contains more than 5 000 command lines.

5.3. Results

In this chapter, moment-rotation curves, energy dissipation capacity and pressure oscillations in the bolts positioned at the lower beam flange are presented for both monotonic loading directions.

The moment is taken by measuring the force at the end of the beam and dividing it by the beam length, $L_{beam} = 1460 \text{ mm}$. The rotation of the connection is obtained by measuring both displacements, at the T-stub level and at the beam lower flange level and then applying the following relation:

$$\phi = \frac{\delta_{beam} - \delta_{T-stub}}{h} \quad (5.2)$$

where h is equal to 265.0 mm , corresponding to the lever arm.

The resistance of the friction damper is given by the connection's moment divided by the lever arm.

Moreover, with the intention of evaluating the beam end displacements due to the beam-to-column joint rotation only, according to Figure 5.7, the moment rotation curves have been corrected by simply subtracting the elastic contribution due to the beam and column flexural deformability:

$$\delta_j = \delta_{beam_end} - \frac{FL_b^3}{3EI_b} - \frac{FL_cL_b^2}{12EI_c} \left[\left(\frac{L_c}{L_c+2a} \right)^2 + \frac{6a}{L_c+2a} \right] \quad (5.3)$$

where F is the measured force at the beam end, a is the length of the rigid parts of the column supports, I_b and I_c are the inertia moments of the beam and column, respectively, and L_b and L_c the beam and column spans, correspondingly.

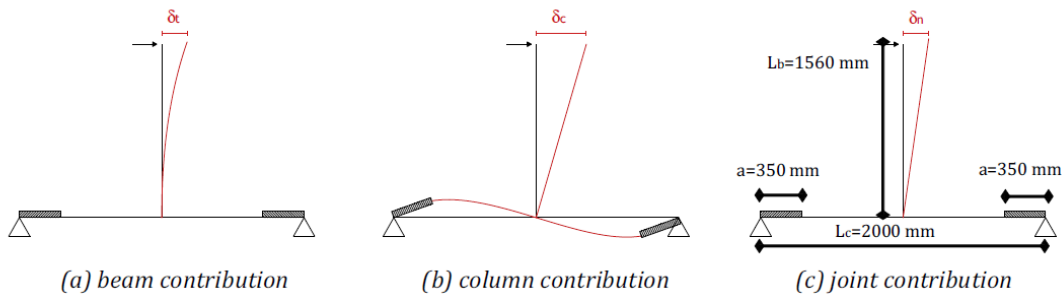


Figure 5.7: Beam end displacements considering each element contribution (Latour et al., 2015).

5.3.1. Monotonic behaviour

Figure 5.8 shows that the numerical results are close to the experimental values. For the sagging moment, the numerical values are actually superimposed with the experimental ones.

As already predicted in **Chapter 4**, the L-stub component is activated for both hogging and sagging moments. It is possible to visualize in Figure 5.8 that, also in the numerical model, some yielding was obtained for this component for the hogging moment as the stiffness of the connection starts to decrease for bending moments larger than approximately 120 kN.m. Additionally, it is also possible to observe that the energy dissipation capacity of the connection is naturally greater when subjected to hogging moments.

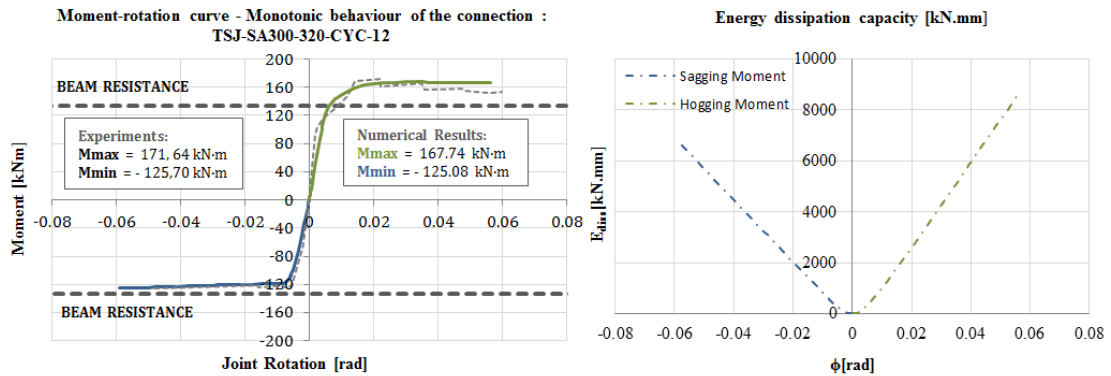


Figure 5.8: Monotonic behaviour of the connection -TSJ-SA300-320-CYC-12.

In Figure 5.9 and Figure 5.10, the stress distribution for the last displacement increment, for each loading direction, is presented. Additionally, the deformed shape of the connection is compared with the experimental deformed specimens. . In Figure 5.9 and Figure 5.10 is possible to visualize the presence of yielding in the L-stubs as the yield strength of steel, accounting with its variability ($f_y=326$ MPa), is exceeded. As expected, the registered stresses are greater for the hogging moment.

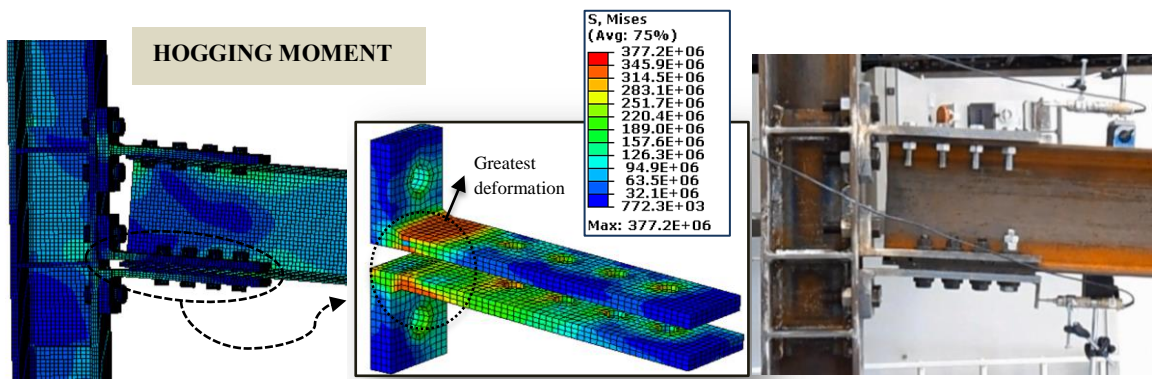


Figure 5.9: Stress distributions obtained at the end of the displacement STEP – Hogging Moment.

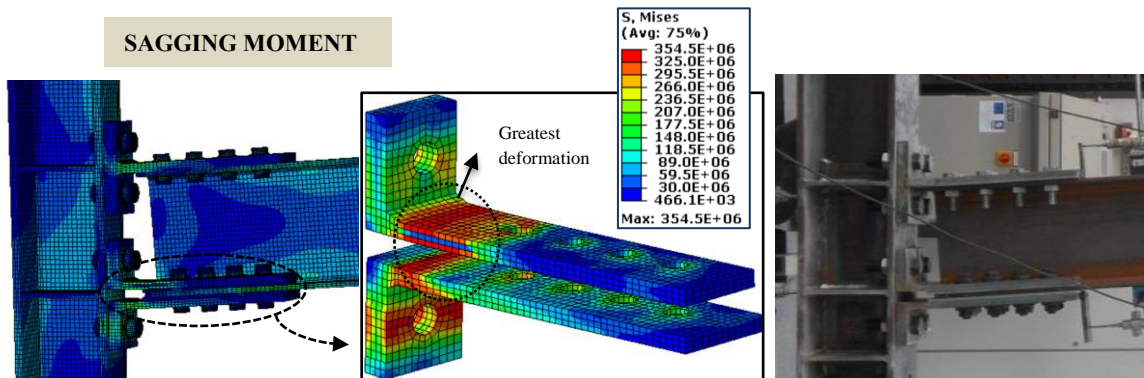


Figure 5.10: Stress distributions obtained at the end of the displacement STEP – Sagging Moment.

Moreover, in order to understand the differences between the sagging and hogging moments, pressure variations in the bolts tightening the friction damper components are analysed.

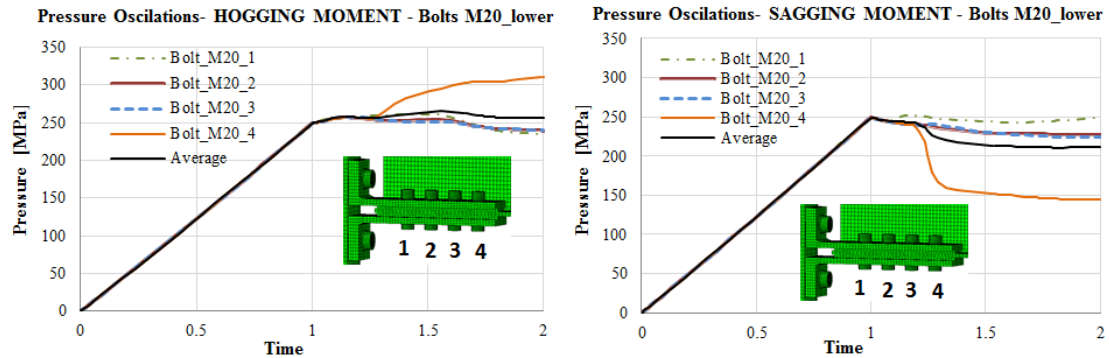


Figure 5.11: Pressure oscillations obtained with reference to the time step increments.

Figure 5.11 shows that the connection rotation influences significantly the bolts pressure, especially in the case of external bolt 4. For hogging moments, the pressure in bolt number 4 tends to increase, giving origin to a higher resistance capacity of the friction damper. On the other hand, the opposite tends to happen for the sagging moment, resulting in a lower resistance of the friction pad.

By calculating the friction damper resistance taking into consideration the bolts pressure oscillations and comparing it with the numerical results, one can obtain the overstrength of the friction device neglecting the influence of the normal force transmitted to the interfaces.

After removing that variable, a new comparison is performed for both monotonic loading directions. Still, a larger resistance was registered for the hogging moment. The overstrength obtained for the hogging moment is 1.28 whereas for the sagging moment, the overstrength obtained is equal to 1.17. In fact, a stick-slip motion in the friction device was detected in the case of the hogging moment, meaning difficulties are arising for the movement in that direction. That can be justified by the fact the beam has to move in the direction of the greatest deformation while the opposite is occurring for the sagging moment (see Figure 5.9 and Figure 5.10). The higher resistance obtained for the hogging moment is therefore justified by the flexural deformation of the L-stubs.

5.3.2. Cyclic behaviour

5.3.2.1. Moment-rotation curve

The $M-\phi$ curves are obtained for the overall connection and the elastic deformation of the beam and column elements are neglected. Then, the resistance of the friction damper is calculated and presented in terms of Force-Displacement curves ($F-\delta$). Both numerical cyclic behaviours are compared with the experimental ones (Figure 5.12).

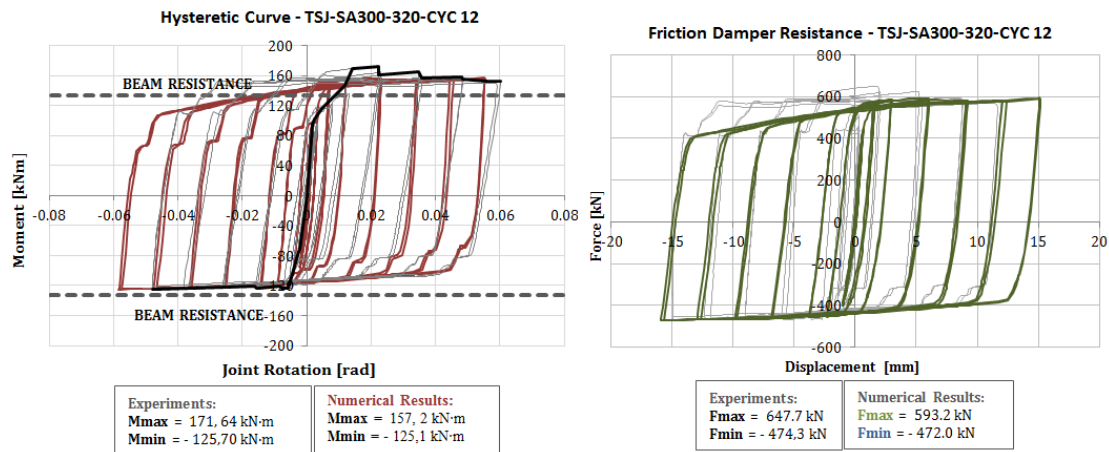


Figure 5.12: Hysteretic behaviour of the overall connection and of the weakest component.

Again, the numerical results give accurate results. However, not only the resistance values but also the stiffness obtained for the hogging moment are more distant from the experimental values.

5.3.2.2. Energy dissipation capacity

As for the energy dissipation capacity, the results obtained for the numerical model are compared with the experimental values reported for the same connection and for other two tested joints, using rubber M1 and M2 as the friction material.

Numerical results are close to the experimental ones and the connection designed to have sprayed aluminium as the friction material proves to have a larger energy dissipation capacity.

Additionally, the energy dissipated by the friction damper is compared with the total energy dissipated for the connection, showing that the joint is able to dissipate the input energy of a seismic event through the slippage of the friction device, preventing damage of the remaining steel components of the connection, as illustrated in Figure 5.13.

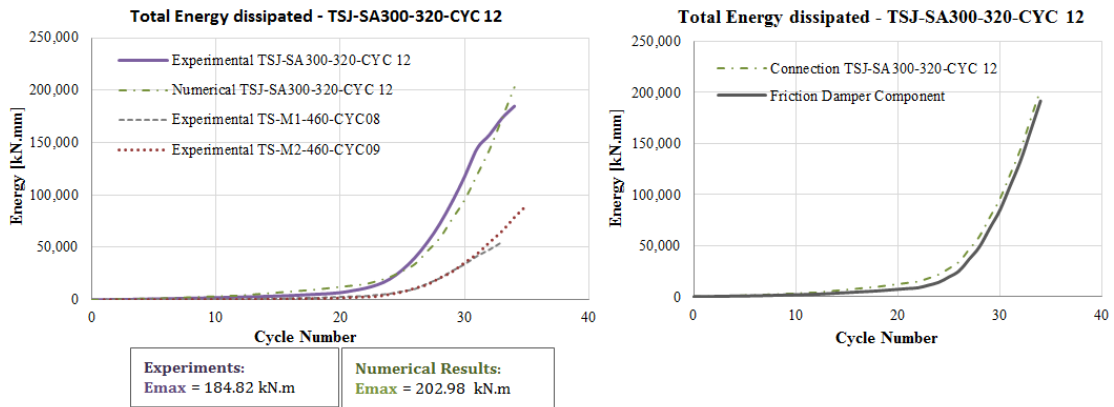


Figure 5.13: Energy dissipation capacity of the innovative connection - TSJ-SA300-320-CYC 12.

5.3.2.3. Variation of the preloading force

The same approach adopted for the monotonic behaviour is now presented. Firstly, the bolt preloading forces variations are obtained, then the resistance of the friction damper is calculated considering the normal force variations and compared with the obtained numerical resistance values. Finally, the overstrength due to the flexural deformation of the friction device elements is presented, separately for positive and negative moments. In Figure 5.14, one can observe both the pressure oscillations and the corresponding friction pad overstrength. Pressure variations are presented with reference to the step time while the overstrength is presented with respect to the semi cycle number. A total of 34 cycles are analysed. The total resistance of the friction pad is mobilized from the 45th semi-cycle onwards, reason why the values obtained for the previous semi-cycles are not presented.

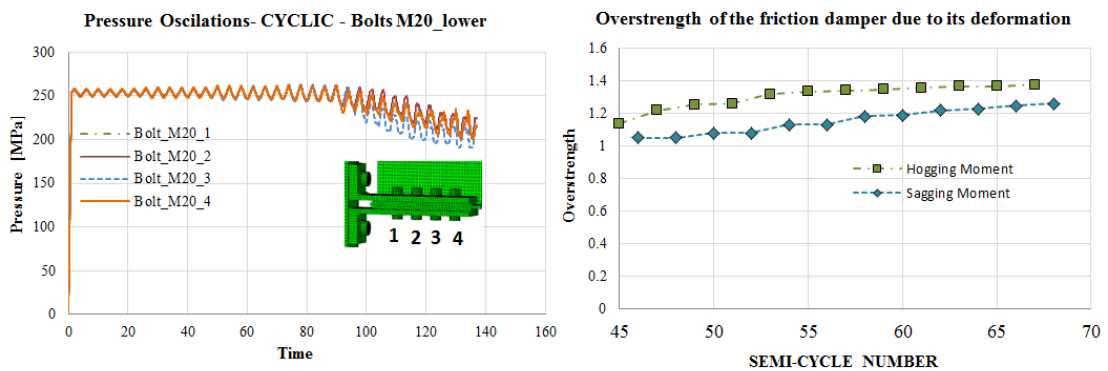


Figure 5.14: Presssure variations – cyclic analysis.

The higher peaks of the bolts pressure are obtained for the hogging moments while the lower peaks correspond to the sagging moments, which is in agreement with what was observed for monotonic loading conditions. It is possible to analyse that the

resistance of the friction damper is also bigger in the case of the hogging moment. The average relation between the overstrength for the hogging moment and the overstrength for the sagging moment being equal to 1.13.

5.3.3. Discussion of the results

It was possible to conclude that the behaviour of the friction damper is different for each loading direction due to two reasons:

- The direction of the force applied at the beam edge influences the preloading forces of the bolts. More specifically, the normal force transmitted to the friction interface tends to increase for hogging moments and to decrease for sagging moments.
- The direction of slip also influences the damper resistance as, for the hogging moment, movement from a less deformed condition to a more deformed state of the plates occurs. The deformation of the plate restrains the movement of the lower beam flange. In fact, it was observed that a stick-slip condition might occur during that movement. However, for the sagging moment, that restraint is less significant because the beam is easily pulled in the opposite direction of the most deformed conditions.

The abovementioned factors combine in the case of the hogging moment, while for the sagging moment, they have opposite effects and compensate each other, which is why the final resistance is the expected one. Moreover, as the resistance of the connection is greater for hogging moments, the L-stubs are subjected to increased bending forces, leading to a more significant yielding of these components. Thus, the L-stub component is activated for both monotonic directions.

Additionally, the connection tested using sprayed aluminium as the friction material, proved to have a wide and stable hysteretic response with a significant energy dissipation capacity.

Some yielding was observed in the L-stub webs, which is why their correct design is of key importance to the behaviour of the connection. Furthermore, no pinching was detected and even without coupon tests, the numerical results obtained were very close to the experimental ones.

6. CONCLUSIONS AND FURTHER STUDIES

6.1. Conclusions

The difficulties in measuring friction became apparent during the experimental programme and a detailed physical explanation of all the phenomena involved is extremely difficult. In fact, friction is a characteristic of the tribosystems and is not exactly a fundamental property of the material. Several variables affect the friction coefficient. These include the lubricant properties, normal force, velocity and acceleration conditions, system stiffness, contact temperature, relative humidity, presence and loss of properties, surface cleanliness and so on.

Moreover, there are no numerical tools developed to simulate friction variations at a microscopic level at present. Therefore, the work developed here at the friction component level is a possible way of introducing friction variations in complex contact phenomena using Abaqus software. A scripting interface was developed so as to “RESTART” the previous analysis with a different friction coefficient. All possible variations in the surfaces sliding against each other were therefore, reported as friction coefficient variations. However, this type of approach must always be accompanied by experimental research.

The friction law generated by the experiments can then be introduced into the numerical model. The numerical model will be validated if the friction variations introduced are obtained as an output. This approach will allow us to vary friction according to the results of the experiments. Once it is clear that friction can be manipulated, this technique may be used in more complex models in which friction oscillations have a significant importance.

The component approach was then tested for the connection. This approach was significantly helpful in order to understand the behaviour of the connection better and to focus attention on the main sources of its variability.

Furthermore, a detailed numerical model was developed for the connection equipped with a friction device using sprayed aluminium at the friction interface, capable of simulating both the monotonic and cyclic behaviour of the connection. The numerical model was validated using the experimental results available and proved capable of providing accurate results. Thus, this proves that the performance of the connection

does not depend significantly on the material's behaviour law, considering that no coupon tests were performed for these connections.

However, a remark should be made concerning the numerical model developed. By using a different friction material, not as stable as the sprayed aluminium, the variability of the behaviour of the connection could increase significantly, leading to a more difficult numerical simulation. This means that the later "RESTART" approach adopted for the friction component should be introduced in this simulation.

Finally, some general considerations can be made. The possibility of using slip resistance connections could lead to a higher efficiency of present buildings as no structural parts would suffer damage in the aftermaths of a severe earthquake. Longer slotted holes may be used in the friction devices in order to avoid the bending mechanism of general joints for high values of spectral accelerations.

It was also demonstrated that this kind of dissipative joints can provide a significantly higher rotational capacity than the minimum value equal to 35 mrad suggested by EC8-1 for frames in ductility class high (DCH).

Additionally, the flexural strength obtained for these joints is greater than the plastic resistance of the connected beam, so that, almost full-strength connections can be obtained without any damage to the beam.

6.2. Further study

An increased robustness of the joint is expected in the case of exceptional events such as explosions or impacts in general. This increment is possible because of an expected catenary action resulting, for example, in the case of the loss of a column due to blast loading or impact loading. In fact, the slippage of the friction dampers up to the stroke end, before the bolts engage in shear and the L-stub webs engage in bearing, makes it possible to obtain an increased vertical component of beam axial forces resulting from the catenary behaviour after column loss. Therefore, a significant improvement in the structural behaviour is expected. This is only possible due to the slippage of the friction material, which is able to accommodate the required displacements without any damage by simply governing the length of the slotted hole.

The robustness of these innovative connections should be studied in further research. Therefore, when subjecting the joints analysed to robustness tests, coupon tests must be made, the resistance of the bolts should be measured accurately and other components must be activated for this study, such as the:

- Shearing of the bolts tightening the friction device interfaces;
- Bearing of the friction device plates.

In this case, as there are two shearing planes, a reduction of the resistance of the bolts in shear must be contemplated through the consideration of the coefficient β_P , presented in EC3-1-8 (section 3.6), which takes into account the formation of two hinges in the shanks of the bolts instead of one.

Additionally, due to variations of the preloading force during the lifetime of the connections presented herein, it is important to develop long-term tests to evaluate the influence of time on the normal force acting on the sliding surface containing the slotted holes. Long-term tests are also important in terms of evaluating the influence of the relaxation effects that occur over time. These tests should be helpful when deciding what the best structural strategy should be adopted to preserve the tightness of the bolts.

Naturally, the influence of the adjacent preloaded bolts and of external loads should also be analysed.

With reference to the numerical modelling, both the monotonic and cyclic behaviour of the components should be analysed in order to characterize their contribution to the performance of the connection. Their energy dissipation capacity should be compared with the energy dissipation capacity of the friction damper and of the overall connection. Additionally, parametric studies should also be performed, in order to provide accurate relations between the friction damper resistance when subjected to compressive and tension loading forces.

Finally there is also the intention of developing a component based approach procedure that accounts for the cyclic loading and accurately characterizes the behaviour of all the components involved in the innovative connection. Additionally, a methodology should be developed in order to predict the seismic behaviour of moment resistance frames equipped with such type of connections.

REFERENCES

ANSI-AISC 341-10 (2010). "Seismic provisions for structural steel buildings". American Institute of Steel Construction. Chicago (Illinois).

Bowden F., Tabor D.(1967). "Friction and Lubrification". Revised Reprint. London, Methuen.

CEN (2005), EN 1993-1-8 - Eurocode 3: Design of Steel Structures - Part 1-8: Design of joints, European Committee for standardization, Brussels.

CEN (2004), EN 1998-1 - Eurocode 8:General rules, seismic actions and rules for buildings - Part 1:General rules and rules for buildings, European Committee for standardization, Brussels.

CNR-UNI 10011 (1997) Costruzioni in acciaio: Istruzioni per il calcolo, l'esecuzione, il collaudo e la manutenzione. Ente Nazionale Italiano di Unificazione, Milano.

EN 14399-3 (2005) "High-strength structural bolting assemblies for preloading – Part 3: System HR – Hexagon bolt and nut assemblies". European Standard, Commission of the European Communities, Brussels.

EN 14399-5 (2005) "High-strength structural bolting assemblies for preloading – Part 5: Plain washers". European Standard, Commission of the European Communities, Brussels.

Grecea, D.; Dinu, F.; Dubinǎ, D. (2004). "Performance criteria for MR steel frames in seismic zones". *Journal of Constructional Steel Research*, Vol. 60, pp.739–749.

Iannone, F.; Latour, M.; Piluso, V.; Rizzano, G. (2011). "Experimental Analysis of Bolted Steel Beam-to-Column Connections: Component Identification". *Journal of Earthquake engineering*, Vol. 15, pp. 214-244

Inoue, K.; Suita, K.; Takeuchi, K.; Chusilp, P.; Nakashima, M.;M.ASCE; Zhou, F. (2006). "Seismic-Resistant Weld-Free Steel Frame Buildings with Mechanical Joints and Hysteretic Dampers". *Journal of Structural Engineering*, Vol. 132, pp.864–872.

Jaspart, J.P. and Maquoi, R. (1994) Prediction of the semi-rigid and partial-strength properties of structural joints, Proceedings of the Annual Technical session, SSRC Lehigh, USA, June 29 1994, pp. 177-192.

Kloecke, F.; Trauth, D.; Shirobokov, A.; Mattfeld, P. (2015). " FE-analysis and in situ visualization of pressure, slip-rate, and temperature dependent coefficients of friction for advanced sheet metal forming: development of a novel coupled user subroutine for

shell and continuum discretization". *Advanced Manufacturing Technology (author's personal copy)*.

Koetaka, Y., Clusilp, P., Zhang, Z., Uno, N. (2005). "Mechanical property of beam-to-column moment connection with hysteretic dampers for column weak axis". *Engineering Structures*, Vol. 27, pp.109–117.

Latour, M., Piluso, Piluso, V. & Rizzano, G. (2014). "Friction joints equipped with sprayed aluminium dampers". *Proceedings of the EUROSTEEL conference, 2014*.

Latour, M.; Piluso, V.; Rizzano, G. (2014). "Experimental analysis on friction materials for supplemental damping devices". *Construction and Building Materials*, Vol. 65, pp.159–176.

Latour, M.; Piluso, V. ;Rizzano, G. (2015). "Free from damage beam-to-column joints: Testing and design of DST connections with friction pads". *Engineering Structures*, Vo. 85, pp. 219–233.

M. Couchaux, I. Ryan, M. Hjiáj Plartic Resistance of L-stubs joints subjected to tensile forces. Rio de Janeiro, 2010

Oh, S.-H., Kim, Y.-J., & Ryu, H.-S. (2009). "Seismic performance of steel structures with slit dampers". *Engineering Structures*, Vol. 31, Issue 9, pp. 1997–2008.

Piluso, V; Rizzano, G. (2008) "Experimental analysis and modelling of bolted T-stubs under cyclic loads ". *Journal of Constructional Steel Research*, Vol.64, pp.655-669.

Simões da Silva, S.; Rebelo, C; Nethercot, D.; Marques, L.; Simões, R.; Vila Real, P.M.M. (2009). "Statistical evaluation on the lateral-torsional buckling resistance of steel I-beams, Part 2: Variability of steel properties". *Journal of Constructional Steel Research*, Vol.65, pp.832-849.

Nogueiro, P.; Simões da Silva, L., Bento, R.;Simões, R. (2007). " Numerical Implementation and Calibration of a Hysteretic Model for Cyclic Response of End-Plate Beam-to-Column Steel Joints under Arbitrary Cyclic Loading".*Advanced Steel Construction*, Vol. 3, No. 1, pp. 459-484.

Ramhormozian, S., & Clifton, G. C. (2014). "The Asymmetric Friction Connection with Belleville springs in the Sliding Hinge Joint". *Proceedings of the NZSEE Conference*.

S. Kishiki, S. Yamada, K.Suzuki, E. Saeki, and A. W. (2006). "New ductile Moment-Resisting Connections Limiting Damage to Specific Elements At the Bottom Flange". *Proceedings of the 8th U.S. National Conference on Earthquake Engineering , California, Paper No. 852*.